

Annals of the ICRP

ICRP PUBLICATION XXX

Specific Absorbed Fractions for Reference Paediatric Individuals

Editor-in-Chief
C.H. CLEMENT

Associate Editor
T. YASUMUNE

Authors on behalf of ICRP
D.W. Jokisch, W.E. Bolch, B.C. Schwarz, N.E. Martinez,
K.F. Eckerman, K. Kim, K.T. Griffin, W.J. Godwin, C. Lee

PUBLISHED FOR

The International Commission on Radiological Protection

by



Please cite this issue as 'ICRP, 20xx. Specific Absorbed Fractions for
Reference Paediatric Individuals.
ICRP Publication XXX. Ann. ICRP xx(x).'

38

39

CONTENTS

40	ABSTRACT.....	3
41	MAIN POINTS.....	4
42	1. INTRODUCTION	5
43	2. ICRP SCHEMA FOR INTERNAL DOSE ASSESSMENT	7
44	2.1. Methodology for dose calculations	7
45	2.2. <i>S</i> -coefficients and the Specific Absorbed Fraction	11
46	3. ICRP REFERENCE INDIVIDUALS.....	15
47	3.1. Sources of reference mass data	15
48	3.2. Inclusion of blood and blood distribution model	24
49	3.3. Age-dependent reference masses	26
50	4. MODELS AND METHODS FOR ENERGY ABSORPTION COMPUTATION	43
51	4.1. Reference voxel phantoms	43
52	4.2. Alimentary tract	49
53	4.3. Respiratory tract.....	50
54	4.4. Skeleton.....	51
55	5. SPECIFIC ABSORBED FRACTION CALCULATION AND TABULATION.....	62
56	5.1. Scaling SAFs to reference mass.....	62
57	5.2. Low energy, limiting SAF values	64
58	5.3. Quality checks on SAF values	66
59	5.4. Plots of example SAFs.....	74
60	REFERENCES	81
61	ANNEX A. DESCRIPTION OF ELECTRONIC FILES	85
62	ACKNOWLEDGEMENTS	87
63		

64 **Specific Absorbed Fractions for Reference Paediatric Individuals**

65 ICRP PUBLICATION XXX

66 Approved by the Commission in October 20YY

67 **Abstract**—The calculation of doses to organs and tissues of interest due to internally emitting
68 radionuclides requires knowledge of the time-dependent distribution of the radionuclide, its
69 physical decay properties, and the fraction of emitted energy absorbed per mass of the target.
70 The latter property is quantified as the specific absorbed fraction (SAF). This document
71 provides photon, electron, alpha-particle, and neutron (for nuclides undergoing spontaneous
72 fission) SAF values for the suite of reference individuals.

73

74 The reference individuals are defined largely by information provided in *Publication 89*. Some
75 improvements and additional data are provided in this publication which define the reference
76 individual's source and target region masses used in the Occupational Intake of Radionuclides
77 (OIR) and Dose Coefficients for Intakes of Radionuclides by Members of the Public (EIR)
78 series of publications. The set of reference individuals includes males and females at ages of
79 0y (newborn), 1y, 5y, 10y, 15y, and 20y (adult). The reference adult masses and SAFs provided
80 in this publication are identical to those in *Publication 133* and those used in the OIR series of
81 publications.

82

83 Computation of SAF values involves simulating radiation transport in computational models
84 which represent the geometry of the reference individuals. The reference voxel phantoms of
85 *Publication 143* are used for photon and neutron transport and most of the electron transport.
86 Alpha particle transport is not necessary for large tissue regions as the short range allows for
87 an assumption of full energy absorption (absorbed fraction of unity) for self-irradiation
88 geometries. Additional computational models are needed for charged particles in small,
89 overlapping or interlaced geometries. Stylised models are described and used for electrons and
90 alpha particles in the alimentary and respiratory tract regions. For charged particles within the
91 skeleton image-based models are used to compute SAFs.

92

93 This publication is accompanied by an electronic supplement which includes files containing
94 SAFs for each radiation type in each reference individual. The supplement also includes source
95 and target region masses for each reference individual, as well as skeletal dose response
96 functions for photons incident upon the skeleton.

97

98 © 20YY ICRP. Published by SAGE.

99

100 *Keywords:* Specific absorbed fraction; absorbed fraction; internal dosimetry; reference
101 individuals; computational phantoms

102

103

MAIN POINTS

104

105

106

107

- **Specific absorbed fraction (SAF) values are provided for ICRP male and female reference individuals at 6 ages (0y, 1y, 5y, 10y, 15y, and 20y) for internally emitted photons, electrons, alpha particles, and fission-spectrum neutrons associated with radionuclides which decay by spontaneous fission.**

108

109

- **Source and target region masses for the reference individuals consistent with these SAF values are tabulated and their origins defined.**

110

111

112

- **SAF values and source and target region masses for the adults are the same as those in *Publication 133* and utilised in the Occupational Intake of Radionuclides (OIR) series of publications.**

113

114

115

116

- **Computational models used to obtain energy absorption data include the reference voxel phantoms of *Publication 143*, stylised models for charged particles in intra-respiratory and intra-alimentary tract geometries, and image-based models for charged particles emitted within the skeleton.**

117

118

119

120

121

- **The reference SAFs presented in this publication will be coupled to the nuclear decay data of *Publication 107* and the biokinetic models describing temporal distribution of radionuclide activity to calculate reference dose coefficients to members of the public in a forthcoming series of publications and dose to patients from radiopharmaceuticals.**

122

123

124

- **In addition to photons, energy-dependent SAFs for electrons and alpha particles are provided representing a significant improvement to radiation protection dosimetry compared to the non-energy dependent SAFs in *Publication 30*.**

125

1. INTRODUCTION

126 (1) *Publication 103* (ICRP 2007) describes the latest revisions to the radiation protection
127 quantities, equivalent and effective dose. Since issued, Committee 2 of the ICRP has been
128 involved in an effort to publish dose coefficients for external (ICRP 2010, 2013, 2020c) and
129 internal exposures. Specific absorbed fractions are required in the ICRP methodology for
130 computing internal dose coefficients. *Publication 133* (ICRP 2016a) contains the SAFs for the
131 reference adults utilised in computing the dose coefficients of the Occupational Intake of
132 Radionuclides (OIR) series (ICRP 2015, 2016b, 2017, 2019, 2022). This publication provides
133 specific absorbed fractions (SAFs) for members of the public including children. These SAFs
134 will be used in the computation of internal dose coefficients in the forthcoming Dose
135 Coefficients for Intakes of Radionuclides by Members of the Public (EIR) series.

136 (2) The computation of internal dose coefficients first requires definition of the individuals
137 for whom the dose coefficients are being computed. A group of 12 reference individuals are
138 defined – a male and female of the newborn, 1-year old, 5-years old, 10-years old, 15-years
139 old, and adult. The definition of the tissue masses comes largely from *Publication 89* (ICRP
140 2002). In this publication these masses are restated and expanded upon or replaced when
141 appropriate.

142 (3) The SAF is defined as the fraction of energy emitted within a source region which is
143 absorbed in a target region per mass of the target region. Target regions may be whole organs
144 or tissue layers. Source regions may be whole organs, tissue regions, surfaces, contents of
145 hollow organs, or distributed around the body in the case of a blood source. To compute the
146 fractional energy absorption, a series of reference computational phantoms and models provide
147 a representative geometry for radiation transport calculations. Reference voxel phantoms
148 (ICRP 2009, 2020b) are used for many of the source-target geometries. Additional
149 computational models provide the intricate geometry needed for charged particle transport in
150 smaller, overlapping or interlaced source and target regions within the alimentary tract,
151 respiratory tract, and skeleton. While the phantoms and models were designed with *Publication*
152 *89* (ICRP 2002) in mind, they are constructs of theoretical anatomical geometries. For a variety
153 of reasons, the masses of regions in the phantoms or models may not exactly match the
154 reference individual definitions. In such cases adjustments are made to phantom/model SAFs
155 to derive appropriate reference SAFs.

156 (4) The masses provided in Table 2.8 of *Publication 89* provide reference values for the
157 masses for each age and sex. Importantly, the mass of the organs and tissues in this table, unless
158 specifically noted, do not include the contribution from blood perfusing organs and tissues.
159 Rather, Table 2.8 generally provides the masses of the organ and tissue parenchyma. To arrive
160 at an organ or tissue mass inclusive of the perfused blood, a blood distribution model must be
161 coupled to the masses in Table 2.8. Section 3.2 of this publication describes in detail how such
162 masses are computed.

163 (5) The reference voxel phantoms in *Publications 110* and *143* were designed based on the
164 parenchyma masses in Table 2.8 of *Publication 89*. As a result, organs and tissues in the
165 reference voxel phantoms are generally smaller than desired due to the missing contribution
166 from perfused blood. Section 5.1 of this publication describes how and which SAFs were
167 adjusted from values computed in reference voxel phantoms to be consistent with target masses
168 inclusive of blood (provided in Section 3.3.) Note that the reference adult mesh-type phantoms
169 in *Publication 145* (ICRP 2020a) did properly account for perfused blood. Forthcoming mesh-
170 type phantoms for reference paediatric individuals will also include the contribution of
171 perfused blood in tissue. However, the mesh-phantoms were not available at the time Monte
172 Carlo transport simulations supporting this publication were performed and therefore the
173 reference voxel phantoms were used as described in Section 4.1.



174 (6) The SAFs for the reference adults were provided in *Publication 133*. Since they are also
175 used in the EIR series and radiopharmaceutical dosimetry, adult SAFs have been included in
176 this publication for ease of access. The adult SAFs do not differ from those used in the OIR
177 series.

178

179 2. ICRP SCHEMA FOR INTERNAL DOSE ASSESSMENT

180 (7) Doses to members of the public may result from environmental exposure to
181 radionuclides. If such a radionuclide is inhaled or ingested, the potential exists for it to be
182 transferred to the blood and incorporated into tissue thereby creating a source of radiation
183 emissions internal to the body. The resulting dose from an intake of radioactive material takes
184 place over an extended period of time, with that extent depending on the physical properties of
185 the nucleus and physiological properties of the chemical form of the material.

186 (8) The methods described in this section will be used to compute internal dose coefficients
187 for members of the public. Internal dose coefficients provide the dose per unit intake activity.
188 Depending on the interest, the coefficient could provide equivalent dose to a specific target
189 tissue or effective dose.

190 (9) The methodology is similar to that presented in the OIR series of publications (ICRP
191 2015, 2016a, 2016b, 2017, 2019) with an important difference in the handling of age. In the
192 OIR series, dose calculations were performed only for the reference adults. Since parameters
193 associated with the reference adults are constant with age, determining the dose delivered over
194 time involved a simple integration of the activity term. The energy absorption term (S -
195 coefficient) for the reference adults is time invariant.

196 (10) The EIR series, however, includes dose coefficients for intakes occurring as children.
197 Unless the radionuclide's physical or biological removal from the body is very fast, growth of
198 the child should be considered. For these individuals, both the activity term and the energy
199 absorption term are varying with time. The section below describes these terms and how their
200 time-variant nature need to be handled in computing internal dose coefficients.

201 (11) The methodology presented here can also be applied to patients in diagnostic nuclear
202 medicine. For such patients, organ absorbed dose coefficients would be the desired quantity
203 rather than equivalent dose coefficients. Finally, the caveat described in section 2.2.1 applies
204 to patient dosimetry.

205 2.1. Methodology for dose calculations

206 (12) The ICRP dosimetry system is presented below as applied to assessment of organ
207 equivalent dose and effective dose following intakes of radionuclides. The system involves
208 numerical solution of reference biokinetic models, yielding the time-dependent activity in
209 various source tissues. These solutions are then coupled with reference data on nuclear decay
210 information and specific absorbed fractions.

211 2.1.1. Computational solutions to the ICRP reference biokinetic models

212 (13) The Human Respiratory Tract Model (HRTM), the Human Alimentary Tract Model
213 (HATM), and the systemic biokinetic models describe the dynamic behaviour of radionuclide
214 movement within the body. Given the route(s) of intake, these models predict the subsequent
215 uptake to the systemic circulation, the distribution among tissues of the body, and the routes of
216 elimination from the body. The physical decay of the radionuclide and its radioactive progeny
217 are also modelled. The result is a coupled system of first-order differential equations. The
218 solution to the set of equations is the time-dependent distribution of the radionuclide and its
219 radioactive progeny in mathematical compartments associated with anatomical regions in the
220 body.

221 (14) Let $N_{i,j}(t)$ represents the number of nuclides of radionuclide i in compartment j at time
 222 t . The rate of change of the number of nuclides i of the decay chain, $i = 1, 2, \dots, n$ with $i = 1$
 223 being the parent nuclide taken into the body, is given in Eq. (2.1). Note that in addition to the
 224 number of nuclei terms, the biokinetic transfer rates may also vary with age and are therefore
 225 functions of time. The function of time notation, (t) , has been omitted from these quantities
 226 on the right-hand side of Eq. 2.1 to improve readability.

$$\frac{dN_{i,j}(t)}{dt} = \sum_{\substack{k=1 \\ k \neq j}}^M N_{i,k} \lambda_{i,k,j} - N_{i,j} \left[\sum_{\substack{k=1 \\ k \neq j}}^M \lambda_{i,j,k} + \lambda_i^P \right] + \sum_{h=1}^{i-1} N_{h,j} \lambda_h^P \beta_{h,i} \quad (2.1)$$

227 where:

- 228 M is the number of compartments describing the kinetics;
- 229 $N_{i,k}$ is the number of nuclei of chain member i in donor compartment k and varies with
- 230 time;
- 231 $\lambda_{i,j,k}$ is the fractional transfer rate of chain member i from compartment j (donor
- 232 compartment) to compartment k (receiving compartment) in the biokinetic model and may
- 233 vary with time (age);
- 234 λ_i^P is the physical decay constant of chain member i ;
- 235 $N_{h,j}$ is the number of nuclei of precursor nuclide h in compartment j and varies with time;
- 236 λ_h^P is the physical decay constant of precursor chain member h ; and
- 237 $\beta_{h,i}$ is the fraction of the decays of chain member h forming member i .

238 (15) Given the initial conditions specified for the compartments, $N_{i,j}(0)$, Eq. (2.1) defines
 239 the dynamic behaviour of the radionuclide and its progeny within the human body. The first
 240 term on the right-hand side of Eq. (2.1) represents the rate of flow of chain member i into
 241 compartment j from all donor compartments. The second term represents the rate of removal
 242 of member i from compartment j both by transfer to receiving compartments and by physical
 243 decay. The third term addresses the ingrowth of member i within compartment j due to the
 244 presence of its precursors h in the compartment. The number of nuclei of the precursor
 245 multiplied by its physical decay is the activity of the precursor, $A_{h,j}$. Note that the members of
 246 the decay chain are assumed to be of order such that the precursors of member i have indexes
 247 less than i . An ordered listing of the chain members can be obtained using the DECDATA
 248 software distributed with *Publication 107* (ICRP, 2008).

249 (16) If all terms in Eq. (2.1) are multiplied by the physical decay constant of the chain
 250 member being considered, λ_i^P , the rate of change of the activity of chain member i in
 251 compartment j is obtained as shown in Eq. (2.2).
 252

$$\frac{dA_{i,j}(t)}{dt} = \sum_{\substack{k=1 \\ k \neq j}}^M A_{i,k} \lambda_{i,k,j} - A_{i,j} \left[\sum_{\substack{k=1 \\ k \neq j}}^M \lambda_{i,j,k} + \lambda_i^P \right] + \sum_{h=1}^{i-1} A_{h,j} \beta_{h,i} \lambda_i^P \quad (2.2)$$

253 (17) The system of $n \times M$ ordinary first-order differential equations is solved using suitable
 254 numerical methods, under the assumption that $A_{i,j}(0) = 0$ for all compartments with the
 255 exception of compartments of intake, where nonzero initial conditions are only applied to the
 256 parent nuclide; i.e. $i = 1$. Information on the physical decay constants and branching fraction,
 257 $\beta_{k,i}$, are available from *Publication 107* (ICRP 2008a).

258 (18) To calculate the numerical values of the dose coefficients, it is necessary to associate
 259 the biokinetic compartments of Eq. (2.2) with anatomical source regions indexed by r_s . A

260 source region may or may not be a living tissue (for example, the stomach contents may be a
 261 source region but is not a living tissue) and may consist of more than one biokinetic
 262 compartment. The time-dependent activity in source region r_s is the sum of the time-dependent
 263 activity in each biokinetic compartment j comprising the source region:

$$A_i(r_s, t) = \sum_j^Q A_{i,j}(t) \quad (2.3)$$

264 where Q represents the total number of compartments comprising the source region being
 265 considered.

266 (19) For intakes in reference adults, dosimetric quantities are invariant with time and it is
 267 convenient to integrate the activity in Eq. (2.3) over the 50-year commitment period to obtain
 268 the total number of nuclear transformations as in the OIR series (ICRP 2015). For intakes in
 269 reference children the dosimetric quantities vary as the reference individual ages. The
 270 integration must then wait until after the time-varying activity is multiplied by a time-varying
 271 dose per nuclear transformation (S -coefficient.)

272 (20) Dividing the activity in Eq. (2.3) by the total intake activity gives the rate of nuclear
 273 transformations per activity intake, $a_i(r_s, t)$:

$$a_i(r_s, t) = \frac{A_i(r_s, t)}{A_{\text{exhaled},0} + \sum_j A_{i,j}(0)} \quad (2.4)$$

274 where the denominator includes the prompt exhaled activity $A_{\text{exhaled},0}$, (pertinent for
 275 inhalations, as only a fraction of the intake activity is deposited in the compartments of the
 276 HRTM) and the summation of parent activity ($i=1$) in all compartments at $t = 0$. Note that in
 277 *Publication 130*, the denominator was erroneously described as excluding this exhaled activity.
 278 *Publication 130*, the denominator was erroneously described as excluding this exhaled activity.
 279 This error was corrected in *Publication 133*. The denominator in Eq. (2.4) has been updated in
 280 this publication to be consistent with the description in *Publication 133*.

281 2.1.2. Computation of the ICRP reference dose coefficients for organ equivalent dose

282 (21) The equivalent dose rate coefficient in target region r_T of the Reference Adult Male,
 283 $\dot{h}^M(r_T, t)$ and the Reference Adult Female, $\dot{h}^F(r_T, t)$, are given by:

$$\dot{h}^M(r_T, t) = \sum_{i=1}^n \sum_{r_S}^m a_i(r_S, t) S_w^M(r_T \leftarrow r_S, t)_i \quad (2.5)$$

$$\dot{h}^F(r_T, t) = \sum_{i=1}^n \sum_{r_S}^m a_i(r_S, t) S_w^F(r_T \leftarrow r_S, t)_i \quad (2.6)$$

285 The S -coefficients, $S_w^M(r_T \leftarrow r_S, t)_i$ and $S_w^F(r_T \leftarrow r_S, t)_i$ give the radiation-weighted equivalent
 286 dose in target region r_T per nuclear transformation ($\text{Sv Bq}^{-1} \text{s}^{-1}$) of chain member i (of n
 287 members in the chain) in a source regions r_S (of m source regions) for the male and female
 288 reference individuals, respectively.

289 (22) The committed equivalent dose coefficients in each target region are given by
 290 integrating the time-dependent equivalent dose rate coefficients over the commitment period
 291 as shown in Eqs. (2.5) and (2.6) where t_o is the age at intake and τ is the commitment period.
 292

$$h_T^M(\tau) = \int_{t_o}^{t_o+\tau} \dot{h}^M(r_T, t) dt \quad (2.7)$$

$$h_T^F(\tau) = \int_{t_o}^{t_o+\tau} \dot{h}^F(r_T, t) dt \quad (2.8)$$

293

294 (23) Dose coefficients resulting from occupational intakes of radionuclides were published
 295 in the OIR series and based on a commitment period of 50 years in the reference adults. In the
 296 EIR series, committed dose coefficients are computed for reference individuals based on
 297 intakes at ages 3-month, 1-year, 5-year, 10-year, 15-year, and adult. For these individuals, the
 298 commitment period is 50 years for intakes as an adult and through age 70 years for intakes at
 299 all other ages. The age at intake for the adult may be 20y or 25y depending on the biokinetics
 300 of the considered radionuclide (for skeletal seeking radionuclides adult maturity is defined at
 301 age 25y.) Regardless of the age at intake for the adult, the commitment period for the adult is
 302 50y. In the OIR series of publications, all quantities contributing to the *S*-coefficient calculation
 303 are invariant with respect to time since the reference workers are adults from the time of intake
 304 throughout the entire commitment period. As a result, only the activity content in source
 305 regions required integration over time and yielded the total number of nuclear transformations
 306 taking place during the commitment period. In the EIR series, this remains true for intakes by
 307 the reference adult. For children, however, the SAF varies with respect to time as the child
 308 grows and the shape, volume, mass, and distance between tissues changes.

309 (24) A number of target tissues are represented by a single target region r_T . In cases where
 310 more than one tissue region defines the target tissue, fractional weighting of the equivalent
 311 dose must be made. The committed equivalent dose coefficients for tissue *T* in the reference
 312 adult male, $h_T^M(\tau)$, and adult female, $h_T^F(\tau)$, are thus given in Eqs. (2.9) and (2.10) as

$$h_T^M(\tau) = \sum_{r_T} f(r_T, T) h^M(r_T, \tau) \quad (2.9)$$

$$h_T^F(\tau) = \sum_{r_T} f(r_T, T) h^F(r_T, \tau) \quad (2.10)$$

313 where the target region fractional weights $f(r_T, T)$, are the proportions of the equivalent dose
 314 in tissue *T* associated with target region r_T . With the exception of the target tissues addressed
 315 in Table 2.1, the target tissues of Table 2.2 are represented by a single target region and thus
 316 for these tissues $f(r_T, T) = 1$. In Table 2.1, values of $f(r_T, T)$ for the extrathoracic (ET) and
 317 thoracic (TH or Lung) regions are taken to be equivalent to their risk apportionment factors as
 318 assigned in the revised HRTM. These are assumed to be the same for children, in the absence
 319 of information (ICRP, 1995b). For the colon, values of $f(r_T, T)$ are taken to be the fractional
 320 masses of the stem cell layers within the alimentary tract walls (see Table 7.8 of *Publication*
 321 *100* (ICRP, 2006)). Sugiyama et al. (2020) found excess relative risks among a cohort of atomic
 322 bomb survivors were not significantly different for proximal and distal colon cancer. The same
 323 study found no variation in risk by age at exposure. For the lymphatic nodes, values of $f(r_T, T)$
 324 are taken to be the fractional masses of lymphatic nodes (not lymphatic tissues) within the ET,
 325 TH, and non-respiratory regions consistent with data given previously in *Publication 66* (ICRP,
 326 1994b). These values are independent of age of the reference individual.

327

328

329

330 Table 2.1. Target region fractional weights, $f(r_T, T)$

Tissue, T	r_T	$f(r_T, T)$
ET	ET ₁	0.001
	ET ₂	0.999
TH	BB*	1/3
	bb	1/3
	AI	1/3
Colon	Right colon	0.4
	Left colon	0.4
	Rectosigmoid	0.2
Lymphatic nodes	LN _{ET}	0.08
	LN _{TH}	0.08
	Lymph (systemic)	0.84

331 ET, extrathoracic; TH, thoracic; ET₁, anterior nasal passage; ET₂, posterior nasal passage, pharynx, and
 332 larynx; BB, bronchial; bb, bronchiolar; AI, alveolar–interstitial; LN_{ET}, ET lymph nodes; LN_{TH}, TH
 333 lymph nodes.

334 *The basal and secretory cells are two target regions weighted equally.

335

336 2.1.3. Computation of the ICRP reference dose coefficients for effective dose

337 As defined in *Publication 103* (ICRP, 2007), the committed effective dose coefficient, $e(\tau)$, is
 338 then:

339

$$e(\tau) = \sum_T w_T \left[\frac{h_T^M(\tau) + h_T^F(\tau)}{2} \right] \quad (2.11)$$

340 where w_T is the tissue weighting factor for tissue T of Table 2.2 and $h_T^M(\tau)$, and $h_T^F(\tau)$, are the
 341 corresponding committed equivalent dose coefficients for these same tissues in the Reference
 342 Male and Reference Female, respectively. The tissue weighting factor for the remainder tissues
 343 is applied to the arithmetic mean of the equivalent doses to the thirteen tissues for each sex.

344

345 Table 2.2. *Publication 103* (ICRP, 2007) tissue weighting factors

Tissue	w_T	$\sum w_T$
Bone-marrow, breast, colon, lung, stomach, remainder tissues (13 for each sex*)	0.12	0.72
Gonads	0.08	0.08
Urinary bladder, oesophagus, liver, thyroid	0.04	0.16
Bone surface, brain, salivary glands, skin	0.01	0.04

346 *Remainder tissues: adrenals, ET regions of the respiratory tract, gall bladder, heart, kidneys, lymphatic
 347 nodes, muscle, oral mucosa, pancreas, prostate (male), small intestine, spleen, thymus, uterus/cervix
 348 (female).

349 2.2. S-coefficients and the Specific Absorbed Fraction

350 (25) The radiation-weighted S -coefficient is the equivalent dose to a target tissue per nuclear
 351 transformation taking place in a source region. The S -coefficient is computed as shown in Eq.
 352 (2.12) and incorporates nuclear decay data, the radiation weighting factor, and the specific
 353 absorbed fraction, $\Phi(r_T \leftarrow r_S, E_{R,i}, t)$.

354

$$S_w(r_T \leftarrow r_S, t) = \sum_R w_R \sum_i E_{R,i} Y_{R,i} \Phi(r_T \leftarrow r_S, E_{R,i}, t) \quad (2.12)$$

355

356 The energy and yield of the i th emission of radiation type R are denoted by $E_{R,i}$ and $Y_{R,i}$ and
 357 are tabulated in *Publication 107*. For the continuous energy spectrum associated with beta
 358 emissions, an integral is required rather than a summation, as shown in Eq. (2.13).
 359

$$S_{w\text{-beta}}(r_T \leftarrow r_S, t) = \int_{i=0}^{i_{\max}} w_R E_{R,i} Y_{R,i}(E_{R,i}) \Phi(r_T \leftarrow r_S, E_{R,i}, t) dE_R \quad (2.13)$$

360

361 (26) In practice it is necessary to separately compute the beta contribution given by Eq.
 362 (2.13) to the S-coefficient from the contribution due to other radiation types. The two
 363 contributions are simply summed to give the total S-coefficient for all emissions from a
 364 particular radionuclide.

365 (27) The radiation weighting factors, w_R , were provided in *Publication 103* (ICRP 2007),
 366 and are found in Table 2.3.
 367

368 Table 2.3. *Publication 103* (ICRP, 2007) radiation weighting factors

Tissue	w_R
Photons	1
Electrons and muons	1
Protons and charged pions	2
Alpha particles, fission fragments, heavy ions	20
Neutrons	$\begin{cases} 2.5 + 18.2 e^{-[\ln(E_n)]^2/6}, & E_n < 1 \text{ MeV} \\ 5.0 + 17.0 e^{-[\ln(2E_n)]^2/6}, & 1 \text{ MeV} \leq E_n \leq 50 \text{ MeV} \\ 2.5 + 3.2 e^{-[\ln(0.04E_n)]^2/6}, & E_n > 50 \text{ MeV} \end{cases}$

369

370 (28) The SAF, Φ , is defined in Eq. (2.14) as the fraction of energy, E_R , emitted from a source
 371 region, r_S , which is absorbed in a target region, r_T , per mass of the target region, m_T . The
 372 absorbed fraction term, ϕ , is a function of the source-target geometry and the energy of
 373 radiation type R .
 374

$$\Phi(r_T \leftarrow r_S, E_R) = \frac{\phi(r_T \leftarrow r_S, E_R)}{m_T} \quad (2.14)$$

375

376 (29) The absorbed fraction is calculated by radiation transport simulation in voxel phantoms
 377 or other geometrical models as described in Section 4. To calculate a SAF corresponding to the
 378 phantom or model, the absorbed fraction is divided by the target mass in that phantom or model.
 379 If the target mass represented within the phantom or model is not equal to that of the reference
 380 individual, then it may be necessary to scale the computed SAF. Section 5.1 describes the
 381 scaling process and when it is desirable. Other portions of Section 5 describe additional quality
 382 checks performed on the phantom and model SAFs.

383 (30) As described in *Publication 133* (ICRP 2016a), the internal dose calculation includes
 384 contributions from activity in the systemic region denoted as Other which consists of systemic
 tissue not explicitly invoked in a particular systemic biokinetic model. Users of SAFs will find

385 it desirable to compute a custom SAF for the Other systemic tissue based on its composition
 386 for a particular case. This SAF is computed using a source-tissue-mass-weighted average of
 387 the constituents as shown in Eq. (2.15), where m_{r_s} is the mass of a constituent source region
 388 and m_{Other} is the total mass of all the systemic tissues not explicitly invoked in the systemic
 389 biokinetic model. Later in this publication, Table 3.16 provides a list of systemic tissues eligible
 390 for inclusion in the Other source region.
 391

$$\Phi(r_T \leftarrow \text{Other}, E_{R,i}) = \frac{1}{m_{\text{Other}}} \sum_{r_s} m_{r_s} \Phi(r_T \leftarrow r_s) \quad (2.15)$$

392
 393 (31) The specific absorbed fractions provided in this publication for electrons, photons, and
 394 alpha particles are tabulated at discrete energies. It is necessary to interpolate between these
 395 energies when seeking the specific absorbed fractions at a specific energy associated with a
 396 particular radionuclide emission. More than 20 energies are tabulated to minimise the impact
 397 of different interpolation techniques. In the OIR and EIR series, a monotone interpolation using
 398 piecewise cubic Hermite spline (PCHIP) is used (Fritsch and Carlson 1980). This interpolation
 399 algorithm uses all known data points to inform the desired interpolated value(s).

400 (32) For intakes in children, the S -coefficient varies with respect to time. Interpolation is
 401 also performed to obtain S -coefficients at non-reference ages. At ages between 1 and 20 years
 402 old, the same PCHIP interpolation technique described above is applied using S -coefficients at
 403 each of the reference ages as input into the interpolation algorithm.

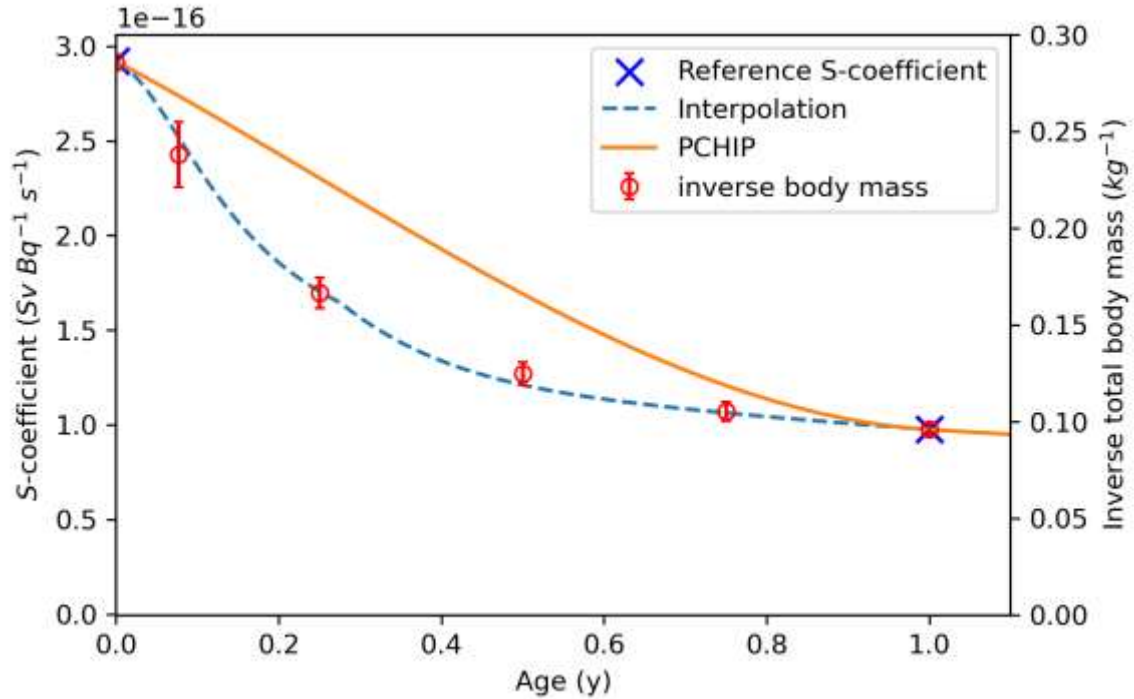
404 (33) *Publication 89* describes the complexities associated with growth rates in different
 405 tissues in the first year of life. Accordingly, during the first year of life a weighted linear
 406 interpolation is used as given in Eq. (2.16) and (2.17) to find the S -coefficient at the desired
 407 time, $S_w(t)$, where x is a fractional factor determined using Eq. (2.17).
 408

$$S_w(t) = x[S_w(1y) - S_w(0y)] + S_w(0y) \quad (2.16)$$

$$x = \begin{cases} t^{[0.3+0.7(1-t)^{10}]}, & 0 \leq t < \frac{100 d}{365 d} \\ t^{[0.16+0.84(1-t)^5]}, & \frac{100 d}{365 d} \leq t < 1y \end{cases} \quad (2.17)$$

409
 410 In Eq. (2.17), t is given as the fraction of 1 year (365 days).

411 (34) Figure 2.1 provides justification for the interpolation described in Eqs. (2.16) and
 412 (2.17). Table 4.3 in *Publication 89* provides the total body mass of European infants (Eveleth
 413 and Tanner 1990; ICRP 2002). The interpolated function is designed to provide a better fit for
 414 the variable growth patterns taking place within the first year of life.
 415



416 Fig. 2.1. S-coefficient interpolation within the first year. The X's represent S-coefficients at
 417 ages 0 and 1-year for the emissions from tritiated water from Other systemic tissue irradiating
 418 the Muscle. The dashed line is the interpolated function provided in Eq. (2.16). The circles are
 419 plotted against the right-hand y-axis and are the inverse of the total body mass provided in Eq.
 420 (4.3) of *Publication 89*. The PCHIP curve is the result if a piecewise cubic Hermite spline
 421 interpolation was applied between birth and age 1y.
 422

423 **2.2.1. Other uses of reference SAFs**

424 (35) The SAFs in this publication have been computed for the primary purpose of
 425 computing organ equivalent dose and effective dose coefficients for use in radiation protection.
 426 However, these SAFs are likely to be useful for a variety of additional internal dosimetry
 427 applications including nuclear medicine (studied by ICRP Task Group 36) and internal dose
 428 reconstruction. Users of these SAFs are advised to keep in mind that they are consistent with
 429 the reference individuals as defined in Section 3. Care should therefore be taken when applying
 430 them to non-reference individuals. Use of these SAFs should be made with an understanding
 431 that one is treating at least one component of the internal dosimetry calculation (fraction of
 432 emitted energy absorbed per unit mass) as equivalent to that in ICRP reference individuals.

433

3. ICRP REFERENCE INDIVIDUALS

434

435 (36) The reference individuals are idealised persons used for the calculation of effective
436 dose (ICRP 2007). The parameters defining the reference individuals include anatomical and
437 physiological parameters. The physiological parameters inform the biokinetic modelling of
438 activity while the anatomical parameters form the basis for of computational phantoms and
439 models used to compute SAFs. While the calculation can be thought of in terms of the product
440 of a source (or biokinetic) term and an energy absorption term, the two terms should be
441 computed in a manner consistent with one another. The characterization and definition of the
442 reference individuals serves as a guiding mechanism for ensuring the two terms involved in the
443 calculation of internal doses maintain consistency with one another. The reference SAFs
444 provided in this document are therefore reference values and consistent with the reference
445 individual definition.

446 3.1. Sources of reference mass data

447 3.1.1. Publication 89

448 (37) *Publication 89* (ICRP 2002) provides most of the reference masses of the reference
449 individuals for males and females of six ages (newborn, 1 year, 5 years, 10 years, 15 years, and
450 adult.) In addition to publishing reference masses based on research in the literature,
451 *Publication 89* included reference values previously published in *Publication 66* (ICRP 1994)
452 on the respiratory tract, *Publication 70* (ICRP 1995b) on the skeleton, *Publication 88* (ICRP
453 2001) on the embryo/foetus and *Publication 23* (ICRP 1975) on the definition of Reference
454 Man.

455 (38) Table 2.8 in *Publication 89* provides a summary table of reference masses of organs
456 and tissues by sex and age. For almost all organs and tissues listed in Table 2.8 the listed mass
457 values do not include the blood perfusing that organ or tissue (i.e., organ parenchyma mass
458 only). When performing the internal dose calculation, it is necessary to describe source masses,
459 generally, as without blood since activity presumably is taken up in tissue in proportion to the
460 parenchyma tissue mass. But since the energy absorption takes place in the entire mass of an
461 organ or tissue which contains blood, the target mass needs to include the mass of blood
462 perfusing the tissue.

463 (39) Table 2.14 in *Publication 89* provides a reference blood distribution for the adult male
464 and female but does not contain similar information for the younger reference ages. Table 2.14
465 gives the percentage of the total body blood volume which is found in each of the organs or
466 tissues listed.

467 3.1.2. Publication 66

468 (40) *Publication 66* (ICRP 1994) provides detailed information on the human respiratory
469 tract model. Table 5 in *Publication 66* was reprinted as Table 5.3 in *Publication 89* and provides
470 reference masses of epithelial target tissues in the respiratory tract, as well as masses for the
471 extrathoracic and thoracic lymph nodes.

472 (41) Table 5 of *Publication 66* did not provide masses for the newborn but newborn masses
473 were provided in Table 5.3 of *Publication 89*. During the preparation of the EIR series of
474 publications, it became clear that the reference newborn masses for the bronchi and bronchiole
475 source and target regions were not computed in *Publications 71* (ICRP 1995a) and *89* in a

476 manner consistent with the methods of *Publication 66*. In this work, new reference masses are
 477 provided for the newborn bronchi and bronchiole regions. Note that considerable uncertainty
 478 exists in the applicability of *Publication 66* methodology for the newborn. Nevertheless, it is
 479 desirable to proceed with a method consistent with that used at other reference ages.

480 (42) The newborn masses are computed here in a method consistent with the method
 481 described in *Publication 66*. Figure 2 in *Publication 66* depicts the stylised cylindrical
 482 dosimetry model for the airway regions. The mass of a tissue layer beginning at some depth d_1
 483 through a depth d_2 could be computed as given in Eq. (3.1) where D is the diameter and L
 484 is the length of the cylindrical airway and ρ is the mass density of the tissue (taken as 1.00 g cm^{-3}
 485 in *Publication 66*).

486

$$m_r = \rho L \pi \left[\left(\frac{D}{2} + d_2 \right)^2 - \left(\frac{D}{2} + d_1 \right)^2 \right] \quad (3.1)$$

487 Since the depths and thicknesses of the tissue layers are small compared to the airway diameter,
 488 the mass can be more simply approximated as the product of mass density, the surface area of
 489 the airway, S , and the thickness of the layer of interest, d .

490

$$m_r \cong \rho S d = \rho S (d_2 - d_1) \quad (3.2)$$

491

492 (43) The airway surface area is computed using the dimensional model of the
 493 tracheobronchial tree provided in *Publication 66* and repeated here in Table 3.1. The surface
 494 area of the bronchial region is given by summing the relative contributions of each branch (1
 495 through 8) in the bronchial tree as shown in Eq. (3.3) where z is the generation of the branch
 496 and D_z and L_z are the diameter and length of the branch.

497

$$S = \sum_{z=1}^8 2^z \pi D_z L_z \quad (3.3)$$

498

499 Table 3.1. Dimensions of the adult tracheobronchial tree of *Publication 66*.

Region	Generation (z)	Diameter (m)	Length (m)
Bronchial	0 Trachea	1.65×10^{-2}	9.1×10^{-2}
	1 Main bronchi	1.20×10^{-2}	3.8×10^{-2}
	2	0.85×10^{-2}	1.5×10^{-2}
	3	0.61×10^{-2}	0.83×10^{-2}
	4	0.44×10^{-2}	0.90×10^{-2}
	5	0.36×10^{-2}	0.81×10^{-2}
	6	0.29×10^{-2}	0.66×10^{-2}
	7	0.24×10^{-2}	0.60×10^{-2}
Bronchiolar	8	0.20×10^{-2}	0.53×10^{-2}
	9	0.1651×10^{-2}	0.4367×10^{-2}
	10	0.1348×10^{-2}	0.3620×10^{-2}
	11	0.1092×10^{-2}	0.3009×10^{-2}
	12	0.0882×10^{-2}	0.2500×10^{-2}
	13	0.0720×10^{-2}	0.2069×10^{-2}
	14	0.0603×10^{-2}	0.1700×10^{-2}
	15 Terminal bronchioles	0.0533×10^{-2}	0.1380×10^{-2}

500

501 (44) *Publication 66* provides information on scaling the airway dimensions to account for
 502 differences in age and sex. For the bronchi region, Table 4 of *Publication 66* provides
 503 instructions on scaling each generation 1-8 based on a study by Phalen et al. (1985). The
 504 footnote of that table provides an equation for a scaling factor, SF , dependent on body height,
 505 H , and a constant, a . The scaling factors are reproduced here in Table 3.2 based on a reference
 506 height for the newborn of 0.51 m.

$$SF = a(H - 1.76) + 1 \tag{3.4}$$

507

508 Table 3.2. Parameters for scaling bronchi dimensions for the reference newborn.

Region	Generation (z)	Constant (a)		Scaling Factors (SF)		Newborn	
		Diameter	Length	Diameter	Length	Diameter (mm)	Length (mm)
Bronchial	0	0.540	0.559	0.325	0.301	5.36	27.4
	1	0.530	0.468	0.338	0.415	4.05	15.8
	2	0.507	0.474	0.366	0.408	3.11	6.11
	3	0.489	0.502	0.389	0.373	2.37	3.09
	4	0.429	0.431	0.464	0.461	2.04	4.15
	5	0.441	0.476	0.449	0.405	1.62	3.28
	6	0.452	0.441	0.435	0.449	1.26	2.96
	7	0.405	0.359	0.494	0.551	1.19	3.31
	8	0.333	0.273	0.584	0.659	1.17	3.49

509

510 (45) Applying Eq. (3.4) with the newborn airway dimensions yields a surface area for the
 511 newborn bronchial region of $7.39 \times 10^{-3} \text{ m}^2$. Table 3.3 summarises the computation of the
 512 newborn bronchi source and target regions.

513

514 Table 3.3. Revised masses for newborn bronchi regions.

Region	Inner depth, d_1 (μm)	Outer depth, d_2 (μm)	Thickness, d (μm)	Mass (g)
Bronch-bas	35	50	15	0.111
Bronch-sec	10	40	30	0.222
Bronchi-b	0	60	60	0.443
Bronchi-q	60	70	10	0.0740

515

516 (46) A similar calculation is performed to determine the masses of the bronchiolar regions
 517 in the newborn. Equation (3.3) can be applied to scaled dimensions for generations 9 through
 518 15. *Publication 66* provides the following description for scaling the bronchiole diameter and
 519 length:

520

521 “The diameter of the bronchioles (generations 9 to 15) is obtained by interpolating
 522 between the reference diameter of the last generation of bronchi (generation 8) and the
 523 first generation of respiratory bronchioles (generation 16). The unique parabola, which
 524 has its minimum at the diameter of the 16th airway generation, provides a good fit to
 525 the bronchiolar airway diameters measured by Phalen et al. (1985) for adult subjects.
 526 This parabolic interpolation is assumed to apply to younger subjects also. In a similar
 527 manner, the lengths of the bronchioles (generations 9 to 15) are obtained by hyperbolic
 528 interpolation between the reference lengths of airways in the 8th and 16th generations.”
 529

530 (47) The parabolic interpolation for the diameters is applied as given in Eq. 3.5 while the
 531 hyperbolic interpolation for the lengths in each generation is given in Eq. 3.6.
 532

$$D_z = D_{16} + (D_8 - D_{16}) \frac{(z - 16)^2}{(8 - 16)^2} \quad (3.5)$$

533

$$L_z = L_{16} + (L_8 - L_{16}) \left(\frac{16}{z} - 1 \right) \quad (3.6)$$

534

535 In order to apply the above equations, the newborn diameters and lengths for generations 8 and
 536 16 must be determined. The values for generation 8 were previously determined (see Table
 537 3.2.) For generation 16, *Publication 66* describes scaling by the one-third power of the
 538 functional residual capacity (FRC). However, *Publication 66* only provides FRC values down
 539 to an age of 3-months old. Gaultier et al. (1979) provides an equation (Eq. 3.7) for FRC for
 540 children from birth to age 3-years.
 541

$$\begin{aligned} FRC_{\text{male}} \text{ (mL)} &= -269 + 6.9H(\text{cm}) \\ FRC_{\text{female}} \text{ (mL)} &= -204 + 5.92H(\text{cm}) \end{aligned} \quad (3.7)$$

542

543 Using the newborn reference height of 0.51 m gives a sex averaged FRC of 90 mL. Equation
 544 (3.8) applies the cube root scaling to determine the diameter and length (designated as
 545 $X_{16,\text{newborn}}$) for generation 16.
 546

$$\begin{aligned} X_{16,\text{newborn}} &= X_{16,\text{adult}} \left(\frac{FRC_{\text{newborn}}}{FRC_{\text{adult}}} \right)^{1/3} \\ D_{16,\text{newborn}} &= 1.535 \times 10^{-4} \text{m} \\ L_{16,\text{newborn}} &= 3.311 \times 10^{-4} \text{m} \end{aligned} \quad (3.8)$$

547 (48) Equations (3.5) and (3.6) can now be applied to determine the newborn airway
 548 dimensions for generations 9 through 15 given in

549 (49) Table 3.4. Equation (3.3) is then adapted to the bronchiolar generations to give a
550 newborn bronchiole surface area of $4.91 \times 10^{-2} \text{ m}^2$. The masses of the newborn bronchiole
551 source and target regions are computed via Eq. (3.2) and provided in Table 3.5.

552

553

554 Table 3.4. Bronchiolar airway dimensions for the reference newborn.

Region	Generation (z)	Diameter (mm)	Length (mm)
Bronchiolar	9	0.9298	2.789
	10	0.7239	2.227
	11	0.5496	1.768
	12	0.4070	1.385
	13	0.2961	1.060
	14	0.2169	0.7826
	15	0.1693	0.5418

555
556 Table 3.5. Revised masses for newborn bronchiolar regions with a surface area of 4.91×10^{-2}
557 m^2 .

Region	Inner depth, d_1 (μm)	Outer depth, d_2 (μm)	Thickness, d (μm)	Mass (g)
Bchiol-sec	4	12	8	0.393
Brchiole-b	0	20	20	0.982
Brchiole-q	20	25	5	0.246

558
559

560 3.1.3. Publication 100

561 (50) *Publication 100* (ICRP 2006) provides detailed information on the human alimentary
562 tract model. While *Publication 100* does not tabulate masses for the alimentary tract target
563 tissues, Section 7 of that publication provides reference geometrical information about the size
564 of the different alimentary tract regions. This information is used to compute reference masses
565 for the alimentary tract target tissues.

566 (51) For example, Table 7.4 of *Publication 100* provides reference lengths and Table 7.5 of
567 *Publication 100* provides internal diameters for the small intestine. From the accompanying
568 text, the target is assumed to be a continuous layer at 130 to 150 μm from the inner surface and
569 is independent of age and sex. Modelling the small intestine as a cylinder means the mass of
570 the target layer can be computed as:

$$m_{SI-stem} = \rho_{tissue} \left[\pi \left(\frac{d}{2} + depth_{outer} \right)^2 - \pi \left(\frac{d}{2} + depth_{inner} \right)^2 \right] l_{cylinder} \quad (3.9)$$

571 where ρ_{tissue} is the mass density of tissue, d is the internal diameter, $l_{cylinder}$ is the length of the
572 small intestine, and $depth_{outer}$ and $depth_{inner}$ are the outer and inner boundaries of the target
573 layer. For the reference 10-year-old, the mass is computed as:

$$m_{SI-stem} = 1.04 \frac{g}{cm^3} \left[\pi \left(\frac{1.6 cm}{2} + 0.0150 cm \right)^2 - \pi \left(\frac{1.6 cm}{2} + 0.0130 cm \right)^2 \right] 220 cm \quad (3.10)$$

$$m_{SI-stem} = 2.34 g \quad (3.11)$$

574 (52) Table 3.6 summarises the reference information provided in *Publication 100* and the
575 resulting masses for the target tissues modelled as cylinders (oesophagus, small intestine, and
576 colon). Table 3.7 contains the information for the stomach which is modelled as a sphere.

577 Table 3.6. Reference values used to compute target tissue masses in the cylindrical geometries of the alimentary tract.

Target region	Abbreviation	Age and sex	Length (cm)	Internal diameter (cm)	Inner depth (µm)	Outer depth (µm)	Mass (g)
Oesophagus stem cells	Oesophagus	Newborn f&m [†]	10	0.5	190	200	0.018
		1-year f&m	13	0.6	190	200	0.027
		5-year f&m	18	0.7	190	200	0.043
		10-year f&m	23	0.8	190	200	0.063
		15-year f&m	26.5*	1	190	200	0.090
		Adult female	26	1	190	200	0.088
		Adult male	28	1	190	200	0.095
Small intestine stem cells	SI-stem	Newborn f&m	80	1	130	150	0.537
		1-year f&m	120	1.2	130	150	0.963
		5-year f&m	170	1.4	130	150	1.586
		10-year f&m	220	1.6	130	150	2.340
		15-year f&m	265*	2	130	150	3.512
		Adult female	260	2	130	150	3.446
		Adult male	280	2	130	150	3.711
Right colon stem cells	RC-stem	Newborn f&m	14	3	280	300	0.280
		1-year f&m	18	4	280	300	0.477
		5-year f&m	23	4.5	280	300	0.685
		10-year f&m	28	5	280	300	0.925
		15-year f&m	30	6	280	300	1.188
		Adult female	30	6	280	300	1.188
		Adult male	34	6	280	300	1.346
Left colon stem cells	LC-stem	Newborn f&m	16	2.5	280	300	0.267
		1-year f&m	21	3	280	300	0.420
		5-year f&m	26	3.5	280	300	0.604
		10-year f&m	31	4	280	300	0.822
		15-year f&m	35	5	280	300	1.157

Target region	Abbreviation	Age and sex	Length (cm)	Internal diameter (cm)	Inner depth (µm)	Outer depth (µm)	Mass (g)
		Adult female	35	5	280	300	1.157
		Adult male	38	5	280	300	1.256
Rectosigmoid stem cells	RS-stem	Newborn f&m	15	1.5	280	300	0.153
		1-year f&m	21	2	280	300	0.282
		5-year f&m	26	2.3	280	300	0.401
		10-year f&m	31	2.5	280	300	0.518
		15-year f&m	35	3	280	300	0.699
		Adult female	35	3	280	300	0.699
		Adult male	38	3	280	300	0.759

578 *The sex-specific lengths in Pub. 100 for the 15-year-old oesophagus and small intestine are close to one another and were averaged which results
 579 in sex-independency in the 15-year-old.

580 †f&m is female and male.

581 Table 3.7. Reference values used to compute target tissue masses in the spherical geometry of the stomach.

Target region	Abbreviation	Age and sex	Volume (cm ³)	Internal diameter (cm)	Inner depth (µm)	Outer depth (µm)	Mass (g)
Stomach stem cells	St-stem	Newborn f&m	30	1.9025	60	100	0.191
		1-year f&m	40	2.094	60	100	0.231
		5-year f&m	60	2.397	60	100	0.302
		10-year f&m	80	2.6383	60	100	0.366
		15-year f&m	120	3.0201	60	100	0.479
		Adult f&m	175	3.4248	60	100	0.616

582

583 **3.2. Inclusion of blood and blood distribution model**

584 (53) The mass for most target regions requires the addition of blood to the masses listed in
 585 Table 2.8 of *Publication 89*. While Table 2.14 of *Publication 89* provides the blood distribution
 586 for the reference adults, the publication does not report explicitly a blood distribution model for
 587 younger ages. Wayson et al. (2018) provides such blood distributions.

588 (54) The values in Table 6 of Wayson et al. are rounded for publication purposes. Since they
 589 represent an intermediate step in the target mass calculation, unrounded values are used to compute
 590 the blood contribution to target masses (using a density of blood of 1.06 g cm⁻³.) Table 3.8 provides
 591 the unrounded blood distribution values used in this publication to compute reference target masses
 592 inclusive of blood.

593

594 Table 3.8. Reference values for regional blood distribution (% total blood volume).

Organ or Tissue	Newborn	1-Year	5-Year	10-Year	15-Year	
	F & M	F & M	F & M	F & M	Female	Male
Fat	2.212	4.958	4.061	4.159	6.608	3.602
Brain	5.413	5.276	4.310	2.670	1.370	1.568
Stomach & oesophagus wall	0.767	0.745	0.935	0.987	0.866	0.932
Small intestine wall	2.837	2.809	3.805	3.933	3.327	3.590
Colon wall	1.596	1.641	2.062	2.217	1.852	2.107
Right heart contents	4.50	4.50	4.50	4.50	4.50	4.50
Left heart contents	4.50	4.50	4.50	4.50	4.50	4.50
Coronary tissues	1.088	0.951	0.846	0.857	0.897	0.831
Kidneys	0.704	1.759	2.159	2.171	1.763	1.905
Liver	12.92	11.36	10.27	9.19	9.38	8.53
Lungs						
Pulmonary gas exchange blood	10.5	10.5	10.5	10.5	10.5	10.5
Pulmonary nutrient blood	2.0	2.0	2.0	2.0	2.0	2.0
Skeletal muscle	6.667	5.536	8.538	10.306	10.303	13.684
Pancreas	0.431	0.502	0.459	0.484	0.505	0.557
Skeletal tissues						
Active marrow	5.190	4.969	4.918	4.916	4.983	4.841
Trabecular bone	3.639	4.388	4.376	4.397	4.352	4.051
Cortical bone	1.294	1.584	1.607	1.612	1.490	1.387
Other skeletal tissues	0.659	0.660	0.672	0.797	0.858	0.856
Skin	3.067	2.066	1.761	1.557	2.240	2.147
Spleen	1.505	1.576	1.422	1.398	1.414	1.433
Thyroid	0.066	0.032	0.031	0.045	0.043	0.043
Lymphatic nodes	0.163	0.165	0.164	0.168	0.177	0.181
Ovaries or testes	0.0123	0.0087	0.0077	0.0071	0.0110	0.0216
Adrenal glands	0.415	0.097	0.063	0.054	0.042	0.051
Urinary bladder wall	0.028	0.022	0.020	0.019	0.018	0.019

Organ or Tissue	Newborn	1-Year	5-Year	10-Year	15-Year	
	F & M	F & M	F & M	F & M	Female	Male
All other tissues	3.826	3.397	2.013	2.558	2.002	2.162
Aorta and large arteries	6.0	6.0	6.0	6.0	6.0	6.0
Large veins	18.0	18.0	18.0	18.0	18.0	18.0

595
596
597
598
599

(55) For many target regions, the mass calculation is described in Eq. (3.12) where f_{blood} is the fraction by volume of blood in the target region, m_{wb} is the mass of blood in the body, and $m_{\text{Tparenchyma}}$ is the mass of the target region without blood.

$$m_{\text{T}} = f_{\text{blood}}m_{\text{wb}} + m_{\text{Tparenchyma}} \quad (3.12)$$

600
601
602

(56) As an example, the target mass of the spleen at age 5 years is computed as:

$$m_{\text{Spleen}} = (0.01422)(1,500g) + 50g = 71.33g \quad (3.13)$$

603
604
605
606

(57) For regions in Table 3.8 which comprise multiple targets, the blood is split by parenchyma mass fraction across those targets. For example, Table 3.8 has a single entry for the lymphatic nodes, but this blood is split across the extrathoracic, thoracic, and systemic lymph node targets by their respective mass fractions.

607
608
609

(58) In the lung regions, the 2.0% nutrient blood is split by mass fraction across the bronchi wall, the bronchiolar wall, and the alveolar interstitium. The pulmonary gas exchange blood (10.5%) is assigned in its entirety to the alveolar interstitium.

610
611
612
613
614
615

(59) There are several target regions not specified in Table 3.8. It becomes problematic to use the ‘All other tissues’ category to assign blood to these regions. First, the total list of target regions remaining does not completely comprise ‘All other tissues’. Even if reasonable attempts are made to determine how much tissue mass corresponds to ‘All other tissues’, practical problems arise such as generating sex-dependent blood mass in tissues for which sex dependency does not exist in the reference model.

616
617
618
619

(60) Instead, an approach was adopted which uses a ratio of blood to lean body mass in the whole-body and applies that to each desired target region not specified in Table 3.8. The method is mathematically summarised in Eq. (3.14).

$$m_{\text{blood in tissue}} = (m_{\text{blood}}:m_{\text{tissue}})_{\text{lean}}m_{\text{Tparenchyma}} \quad (3.14)$$

620
621
622
623

The ratio of blood to lean body mass is computed using information regarding the blood distribution and the lean tissues masses.

$$(m_{\text{blood}}:m_{\text{tissue}})_{\text{lean}} = \frac{m_{\text{blood,wb}}(1.00 - f_{\text{blood,fat}} - f_{\text{blood,aorta}} - f_{\text{blood,veins}})}{m_{\text{total body}} - m_{\text{fat}}} \quad (3.15)$$

624
625
626
627
628

In Eq. (3.15) $f_{\text{blood,fat}}$, $f_{\text{blood,aorta}}$, and $f_{\text{blood,veins}}$ are the blood volume fractions in the respective regions. The mass of the total body (Table 2.8) and the mass of fat (page 76) each come from values in *Publication 89*. For example, the blood in the 15-year female breast is computed as:

$$m_{\text{blood,breast}} = \left(\frac{3,500g(1.00 - 0.06608 - 0.060 - 0.18)}{53,000g - 14,000g} \right) 250g = 15.6g \quad (3.16)$$

629

630 **3.3. Age-dependent reference masses**

631 (61) The masses of the reference individuals are tabulated by target and source regions. The 43
 632 target regions (41 regions in each sex) consist of those tissues which contribute to effective dose
 633 along with a select set of tissues which may also be of interest for different applications. The 79
 634 source regions are regions where biokinetic modelling may assign activity.

635 **3.3.1. Target region masses**

636 (62) Table 3.9 provides the list of target regions, their corresponding abbreviations and
 637 information on the source and basis of the mass value. Tables 3.10 through 3.15 provide the
 638 reference masses for each of the reference individuals. When applicable, the contribution of blood
 639 to a target region’s mass is shown.
 640

641 Table 3.9. Target region names, abbreviations, and origin of reference masses.

Target region	Abbreviation	Origin of parenchyma mass	Origin of blood distribution
Oral mucosa	O-mucosa	Scaled from tongue	Lean body mass ratio*
Oesophagus stem cells	Oesophagus	Based on Pub. 100 [†]	NA
Stomach stem cells	St-stem	Based on Pub. 100 [†]	NA
Small intestine stem cells	SI-stem	Based on Pub. 100 [†]	NA
Right colon stem cells	RC-stem	Based on Pub. 100 [†]	NA
Left colon stem cells	LC-stem	Based on Pub. 100 [†]	NA
Rectosigmoid stem cells	RS-stem	Based on Pub. 100 [†]	NA
Anterior nose epithelium	ET1-bas	Pub. 89-Table 5.3 [‡]	NA
Extrathoracic airway epithelium	ET2-bas	Pub. 89-Table 5.3 [‡]	NA
Extrathoracic lymph nodes	LN-ET	Pub. 89-Table 5.3 [‡]	Wayson et al [§]
Bronchi basal layer	Bronchi-bas	Pub. 89-Table 5.3 [‡]	NA
Bronchi secretory layer	Bronchi-sec	Pub. 89-Table 5.3 [‡]	NA
Bronchiolar secretory layer	Bchiol-sec	Pub. 89-Table 5.3 [‡]	NA
Alveolar interstitium	AI	Pub. 89-Table 5.3 [‡]	Computed in this work ^{¶¶}

Target region	Abbreviation	Origin of parenchyma mass	Origin of blood distribution
Thoracic lymph nodes	LN-Th	Pub. 89-Table 5.3 [†]	Wayson et al [§]
Red marrow	R-marrow	Pub. 89-Table 2.8 [¶]	Wayson et al [§]
Skeletal endosteum	Endost-BS		
Brain	Brain	Pub. 89-Table 2.8 [¶]	Wayson et al [§]
Lens of the eye	Eye-lens	Pub. 23, Pub. 143 ^{**}	NA
Pituitary gland	P-gland	Pub. 89-Table 2.8 [¶]	Lean body mass ratio [*]
Tongue	Tongue	Pub. 89-Table 2.8 [¶]	Lean body mass ratio [*]
Tonsils	Tonsils	Pub. 89-Table 2.8 [¶]	Lean body mass ratio [*]
Salivary glands	S-glands	Pub. 89-Table 2.8 [¶]	Lean body mass ratio [*]
Thyroid	Thyroid	Pub. 89-Table 2.8 [¶]	Wayson et al [§]
Breast	Breast	Pub. 89-Table 2.8 [¶] and Pub. 143 ^{§§}	Lean body mass ratio [*]
Thymus	Thymus	Pub. 89-Table 2.8 [¶]	Lean body mass ratio [*]
Heart wall	Ht-wall	Pub. 89-Table 2.8 [¶]	Wayson et al [§] , Pub. 89 [¶]
Adrenals	Adrenals	Pub. 89-Table 2.8 [¶]	Wayson et al [§]
Liver	Liver	Pub. 89-Table 2.8 [¶]	Wayson et al [§]
Pancreas	Pancreas	Pub. 89-Table 2.8 [¶]	Wayson et al [§]
Kidneys	Kidneys	Pub. 89-Table 2.8 [¶]	Wayson et al [§]
Spleen	Spleen	Pub. 89-Table 2.8 [¶]	Wayson et al [§]
Gall bladder wall	GB-wall	Pub. 89-Table 2.8 [¶]	Lean body mass ratio [*]
Ureters	Ureters	Pub. 89-Table 2.8 [¶]	Lean body mass ratio [*]
Urinary bladder wall	UB-wall	Pub. 89-Table 2.8 [¶]	Wayson et al [§]
Ovaries	Ovaries	Pub. 89-Table 2.8 [¶]	Wayson et al [§]
Testes	Testes	Pub. 89-Table 2.8 [¶]	Wayson et al [§]
Prostate	Prostate	Pub. 89-Table 2.8 [¶]	Lean body mass ratio [*]
Uterus	Uterus	Pub. 89-Table 2.8 [¶]	Lean body mass ratio [*]
Systemic lymph nodes	LN-Sys	Derived from Pub. 66 and 89 ^{††}	Wayson et al [§]
Skin	Skin	Pub. 89-Table 2.8 [¶]	Wayson et al [§]
Adipose	Adipose	Modified from Pub. 89-Table 2.8 [¶]	Wayson et al [§]
Muscle	Muscle	Pub. 89-Table 2.8 [¶]	Wayson et al [§]

642 *Blood component for these tissues computed by using ratio of mass of blood in lean body mass to lean
 643 body mass (see explanation in text.)

644 †The stylised geometries described in *Publication 100* (ICRP 2006).

645 [†]Contained in Table 5.3 of *Publication 89* (ICRP 2002). Newborn values of the bronchi and bronchiole
646 regions computed in this work via the method in *Publication 66*.

647 [§]Contained in Table 6 of Wayson et al. (2018).

648 [¶]Contained in Table 2.8 of *Publication 89* (ICRP 2002)

649 ^{**}*Publication 23* describes age-dependency for the lens of the eye but does not provide reference values.
650 The phantom mass in *Publication 143* was chosen for the target mass of the lens.

651 ^{††}*Publication 89* (ICRP 2002) describes the age dependency of the total lymph node mass. This information
652 combined with the information in *Publication 66* (ICRP 1994) on the masses of the extrathoracic and
653 thoracic lymph nodes was used to calculate the systemic lymph node mass.

654 [#]The adipose mass was adjusted from the values in Table 2.8 of *Publication 89* to maintain consistency
655 with the total body mass.

656 ^{§§}*Publication 89* does not contain reference masses for the breast at ages 10 years and younger. The phantom
657 masses in *Publication 143* (ICRP 2020b) were adopted at those ages.

658 ^{¶¶}95.1% of the parenchyma lung mass in Table 2.8 from *Publication 89* was used as a starting point for the
659 parenchyma mass of the alveolar tissue. Based on the blood distribution in Wayson et al., a low-energy,
660 limiting SAF for the (AI ← Blood) geometry was computed. This limiting SAF and the alveolar tissue
661 mass inclusive of blood from Table 5 of *Publication 66* (and Table 5.3 of *Publication 89*) to arrive at the
662 mass of blood in AI and the parenchyma mass of AI. The complexity of this calculation is due to Tables
663 2.8 and 5.3 of *Publication 89* containing AI and Lung masses which are not consistent with one another for
664 several ages.

665

666

667

668 Table 3.10. Masses for target regions in the reference newborn (female / male). The target mass
669 is inclusive of blood when applicable.

Target region	Parenchyma mass (g)	Mass of blood (g)	Target mass (g)
O-mucosa	1.608	0.112	1.72
Oesophagus	0.018	NA	0.018
St-stem	0.191	NA	0.191
SI-stem	0.537	NA	0.537
RC-stem	0.280	NA	0.280
LC-stem	0.267	NA	0.267
RS-stem	0.153	NA	0.153
ET1-bas	0.0024	NA	0.0024
ET2-bas	0.053	NA	0.053
LN-ET	0.70	0.023	0.723
Bronch-bas	0.110	NA	0.110
Bronch-sec	0.220	NA	0.220
Bchiol-sec	0.393	NA	0.393
AI	23.0	29.0	52.0
LN-Th	0.70	0.023	0.723
R-marrow	50	15.1	65.1
Endost-BS	34	10.2	44.2
Brain	380	15.7	395.7
Eye-lens	0.13	NA	0.13
P-gland	0.10	0.0068	0.107
Tongue	3.5	0.239	3.74
Tonsils	0.10	0.0068	0.107
S-glands	6.0	0.410	6.41
Thyroid	1.3	0.190	1.49
Breast	0.08	0.0055	0.085
Thymus	13	0.889	13.9
Ht-wall	20	3.16	23.16
Adrenals	6.0	1.2	7.20
Liver	130	37.5	167.5
Pancreas	6.0	1.25	7.25
Kidneys	25	2.04	27.04
Spleen	9.5	4.36	13.86
GB-wall	0.5	0.0342	0.534
Ureters	0.77	0.0526	0.823
UB-wall	4.0	0.0803	4.08
Ovaries	0.30	0.0355	0.336
Testes	0.85	0.0355	0.886
Prostate	0.80	0.0547	0.855
Uterus	4.0	0.273	4.27
LN-Sys	12.9	0.425	13.3
Skin	175	8.90	183.9
Adipose	1016/1019*	6.4	1022/1025*
Muscle	800	19.33	819.3

670 *The small differences in adipose mass between the female and male result from differences in sex specific
 671 tissues (ovaries, prostate, testes, and uterus) and a desire for the total body mass to match the reference total
 672 body mass of *Publication 89* which is not sex specific at younger ages.
 673
 674

675 Table 3.11. Masses for target regions in the reference 1-year old (female / male). The target mass
 676 is inclusive of blood when applicable.

Target region	Parenchyma mass (g)	Mass of blood (g)	Target mass (g)
O-mucosa	4.679	0.231	4.910
Oesophagus	0.027	NA	0.027
St-stem	0.231	NA	0.231
SI-stem	0.963	NA	0.963
RC-stem	0.477	NA	0.477
LC-stem	0.420	NA	0.420
RS-stem	0.282	NA	0.282
ET1-bas	0.0041	NA	0.0041
ET2-bas	0.093	NA	0.093
LN-ET	2.1	0.073	2.173
Bronch-bas	0.16	NA	0.16
Bronch-sec	0.31	NA	0.31
Bchiol-sec	0.60	NA	0.60
AI	80.55	69.45	150
LN-Th	2.1	0.073	2.173
R-marrow	150	26.3	176.3
Endost-BS	70	10.9	80.9
Brain	950	28.0	978.0
Eye-lens	0.22	NA	0.22
P-gland	0.15	0.0073	0.157
Tongue	10	0.489	10.49
Tonsils	0.50	0.0244	0.524
S-glands	24	1.174	25.17
Thyroid	1.8	0.168	1.97
Breast	0.43	0.0210	0.451
Thymus	30	1.467	31.5
Ht-wall	50	5.04	55.04
Adrenals	4	0.51	4.51
Liver	330	60.2	390.2
Pancreas	20	2.66	22.66
Kidneys	70	9.32	79.32
Spleen	29	8.35	37.35
GB-wall	1.4	0.0685	1.468
Ureters	2.2	0.1076	2.308
UB-wall	9	0.1155	9.12
Ovaries	0.80	0.0463	0.846
Testes	1.5	0.0463	1.546
Prostate	1.0	0.0489	1.049

Target region	Parenchyma mass (g)	Mass of blood (g)	Target mass (g)
Uterus	1.5	0.073	1.57
LN-Sys	20.8	0.727	21.5
Skin	350	10.95	361
Adipose	4028/4027	26.28	4054/4053
Muscle	1900	29.34	1929.3

677
678
679
680

Table 3.12. Masses for target regions in the reference 5-year old (female and male). The target mass is inclusive of blood when applicable.

Target region	Parenchyma mass (g)	Mass of blood (g)	Target mass (g)
O-mucosa	8.715	0.615	9.330
Oesophagus	0.043	NA	0.043
St-stem	0.302	NA	0.302
SI-stem	1.586	NA	1.586
RC-stem	0.685	NA	0.685
LC-stem	0.604	NA	0.604
RS-stem	0.401	NA	0.401
ET1-bas	0.0083	NA	0.0083
ET2-bas	0.19	NA	0.19
LN-ET	4.1	0.206	4.306
Bronch-bas	0.23	NA	0.23
Bronch-sec	0.47	NA	0.47
Bchiol-sec	0.95	NA	0.95
AI	117	183	300
LN-Th	4.1	0.206	4.306
R-marrow	340	73.6	413.8
Endost-BS	203	30.6	233.6
Brain	1180/1310	64.7	1245/1375
Eye-lens	0.33	NA	0.33
P-gland	0.25	0.0175	0.268
Tongue	19	1.331	20.33
Tonsils	2	0.1401	2.140
S-glands	34	2.382	36.38
Thyroid	3.4	0.471	3.87
Breast	0.94	0.0659	1.006
Thymus	30	2.102	32.1
Ht-wall	85	12.70	97.70
Adrenals	5	0.95	5.95
Liver	570	154	724
Pancreas	35	6.89	41.89
Kidneys	110	32.39	142.4
Spleen	50	21.33	71.33
GB-wall	2.6	0.1822	2.782
Ureters	4.2	0.2943	4.494
UB-wall	16	0.3041	16.30

Target region	Parenchyma mass (g)	Mass of blood (g)	Target mass (g)
Ovaries	2.0	0.1150	2.115
Testes	1.7	0.1150	1.815
Prostate	1.2	0.0841	1.284
Uterus	3	0.210	3.21
LN-Sys	40.6	2.041	42.6
Skin	570	26.41	596.4
Adipose	5831/5703	60.91	5892/5764
Muscle	5600	128.1	5728

681
682
683
684

Table 3.13. Masses for target regions in the reference 10-year old (female and male). The target mass is inclusive of blood when applicable.

Target region	Female			Male		
	Parenchyma mass (g)	Mass of blood (g)	Target mass (g)	Parenchyma mass (g)	Mass of blood (g)	Target mass (g)
O-mucosa	14.7	1.0	15.7	14.7	1.0	15.7
Oesophagus	0.063	NA	0.063	0.063	NA	0.063
St-stem	0.366	NA	0.366	0.366	NA	0.366
SI-stem	2.34	NA	2.34	2.34	NA	2.34
RC-stem	0.925	NA	0.925	0.925	NA	0.925
LC-stem	0.822	NA	0.822	0.822	NA	0.822
RS-stem	0.518	NA	0.518	0.518	NA	0.518
ET1-bas	0.013	NA	0.013	0.013	NA	0.013
ET2-bas	0.28	NA	0.28	0.28	NA	0.28
LN-ET	6.8	0.353	7.153	6.8	0.353	7.153
Bronch-bas	0.31	NA	0.31	0.31	NA	0.31
Bronch-sec	0.62	NA	0.62	0.62	NA	0.62
Bchiol-sec	1.3	NA	1.3	1.3	NA	1.3
AI	196	304	500	196	304	500
LN-Th	6.8	0.353	7.153	6.8	0.353	7.153
R-marrow	630	122.9	752.9	630	122.9	752.9
Endost-BS	478	49.4	527.4	478	49.4	527.4
Brain	1220	66.8	1287	1400	66.8	1467
Eye-lens	0.35	NA	0.35	0.35	NA	0.35
P-gland	0.35	0.0242	0.374	0.35	0.0242	0.374
Tongue	32	2.210	34.21	32	2.210	34.21
Tonsils	3.0	0.2072	3.207	3.0	0.2072	3.207
S-glands	44	3.039	47.04	44	3.039	47.04
Thyroid	7.9	1.120	9.02	7.9	1.120	9.02
Breast	7.53	0.5202	8.050	7.12	0.4918	7.612
Thymus	35	2.418	37.42	40	2.763	42.76
Ht-wall	140	21.4	161.4	140	21.4	161.4
Adrenals	7	1.36	8.36	7	1.36	8.36
Liver	830	229.7	1060	830	229.7	1060
Pancreas	60	12.10	72.10	60	12.10	72.10

Target region	Female			Male		
	Parenchyma mass (g)	Mass of blood (g)	Target mass (g)	Parenchyma mass (g)	Mass of blood (g)	Target mass (g)
Kidneys	180	54.28	234.28	180	54.28	234.28
Spleen	80	34.95	114.95	80	34.95	114.95
GB-wall	4.4	0.3039	4.704	4.4	0.3039	4.704
Ureters	7	0.4835	7.484	7	0.4835	7.484
UB-wall	25	0.4866	25.49	25	0.4866	25.49
Ovaries	3.5	0.1785	3.679	NA	NA	NA
Testes	NA	NA	NA	2	0.1785	2.179
Prostate	NA	NA	NA	1.6	0.1105	1.711
Uterus	4	0.276	4.28	NA	NA	NA
LN-Sys	67.3	3.496	70.8	67.3	3.496	70.8
Skin	820	38.92	858.9	820	38.92	858.9
Adipose	9063	103.97	9167	8882	103.97	8986
Muscle	11000	257.7	11258	11000	257.7	11258

685
686
687
688

Table 3.14. Masses for target regions in the reference 15-year old (female and male). The target mass is inclusive of blood when applicable.

Target region	Female			Male		
	Parenchyma mass (g)	Mass of blood (g)	Target mass (g)	Parenchyma mass (g)	Mass of blood (g)	Target mass (g)
O-mucosa	24.49	1.51	26.00	25.6	1.90	27.5
Oesophagus	0.09	NA	0.09	0.09	NA	0.09
St-stem	0.479	NA	0.479	0.479	NA	0.479
SI-stem	3.512	NA	3.512	3.512	NA	3.512
RC-stem	1.188	NA	1.188	1.188	NA	1.188
LC-stem	1.157	NA	1.157	1.157	NA	1.157
RS-stem	0.699	NA	0.699	0.699	NA	0.699
ET1-bas	0.017	NA	0.017	0.019	NA	0.019
ET2-bas	0.38	NA	0.38	0.42	NA	0.42
LN-ET	11	0.522	11.52	12	0.731	12.73
Bronch-bas	0.38	NA	0.38	0.41	NA	0.41
Bronch-sec	0.76	NA	0.76	0.82	NA	0.82
Bchiol-sec	1.6	NA	1.6	1.8	NA	1.8
AI	311	489	800	297	563	860
LN-Th	11	0.522	11.522	12	0.731	12.73
R-marrow	1000	174.4	1174	1080	232.3	1312
Endost-BS	352	28.5	380.5	395	39.3	434.3
Brain	1300	47.9	1348	1420	75.3	1495
Eye-lens	0.4	NA	0.4	0.49	NA	0.49
P-gland	0.5	0.0311	0.531	0.5	0.037	0.537
Tongue	53	3.301	56.30	56	4.141	60.14
Tonsils	3.0	0.1868	3.187	3	0.2218	3.222

Target region	Female			Male		
	Parenchyma mass (g)	Mass of blood (g)	Target mass (g)	Parenchyma mass (g)	Mass of blood (g)	Target mass (g)
S-glands	65	4.048	69.05	68	5.028	73.03
Thyroid	12	1.497	13.50	12	2.041	14.04
Breast	250	15.57	265.6	15	1.109	16.11
Thymus	30	1.868	31.87	35	2.588	37.6
Ht-wall	220	31.4	251.4	230	39.9	269.9
Adrenals	9	1.47	10.47	10	2.43	12.43
Liver	1300	328.3	1628	1300	409.4	1709.4
Pancreas	100	17.68	117.7	110	26.73	136.7
Kidneys	240	61.71	301.7	250	91.44	341.4
Spleen	130	49.49	179.5	130	68.79	198.8
GB-wall	7.3	0.4546	7.755	7.7	0.5693	8.269
Ureters	12	0.7473	12.75	12	0.8873	12.89
UB-wall	35	0.6187	35.62	40	0.9071	40.91
Ovaries	6	0.3857	6.386	NA	NA	NA
Testes	NA	NA	NA	16	1.037	17.04
Prostate	NA	NA	NA	4.3	0.3179	4.618
Uterus	30	1.868	31.87	NA	NA	NA
LN-Sys	108.8	5.167	114.0	118.7	7.231	125.9
Skin	1700	78.39	1778	2000	103.1	2103
Adipose	17660	231.3	17890	11340	172.9	11510
Muscle	17000	360.6	17360	24000	656.8	24660

689
690
691
692

Table 3.15. Masses for target regions in the reference adult (female and male). The target mass is inclusive of blood when applicable. Values identical to those in *Publication 133* (ICRP 2016a).

Target region	Female			Male		
	Parenchyma mass (g)	Mass of blood (g)	Target mass (g)	Parenchyma mass (g)	Mass of blood (g)	Target mass (g)
O-mucosa	22.45	NA*	22.45	35.8	NA*	35.8
Oesophagus	0.088	NA	0.088	0.095	NA	0.095
St-stem	0.616	NA	0.616	0.616	NA	0.616
SI-stem	3.446	NA	3.446	3.711	NA	3.711
RC-stem	1.188	NA	1.188	1.346	NA	1.346
LC-stem	1.157	NA	1.157	1.256	NA	1.256
RS-stem	0.699	NA	0.699	0.759	NA	0.759
ET1-bas	0.017	NA	0.017	0.020	NA	0.020
ET2-bas	0.39	NA	0.39	0.45	NA	0.45
LN-ET	12	0.690	12.69	15	0.942	15.9
Bronch-bas	0.39	NA	0.39	0.43	NA	0.43
Bronch-sec	0.78	NA	0.78	0.86	NA	0.86
Bchiol-sec	1.9	NA	1.9	1.9	NA	1.9

Target region	Female			Male		
	Parenchyma mass (g)	Mass of blood (g)	Target mass (g)	Parenchyma mass (g)	Mass of blood (g)	Target mass (g)
AI	400	504	904	450	650	1100
LN-Th	12	0.690	12.7	15	0.942	15.9
R-marrow	900	164	1064	1170	224	1394
Endost-BS	407	25.3	433	544	35.6	580
Brain	1300	49.2	1349	1450	67.2	1517
Eye-lens	0.4	NA	0.4	0.4	NA	0.4
P-gland	0.6	0.0185	0.618	0.6	0.0281	0.628
Tongue	60	1.85	61.85	73	3.42	76.42
Tonsils	3	0.0923	3.092	3	0.141	3.141
S-glands	70	2.15	72.15	85	3.98	88.98
Thyroid	17	2.46	19.46	20	3.36	23.36
Breast	500	15.4	515.4	25	1.17	26.17
Thymus	20	0.615	20.62	25	1.17	26.17
Ht-wall	250	41	291	330	56	386
Adrenals	13	2.46	15.46	14	3.36	17.36
Liver	1400	410	1810	1800	560	2360
Pancreas	120	24.6	144.6	140	33.6	173.6
Kidneys	275	82.0	357	310	112	422
Spleen	130	57.4	187.4	150	78.4	228.4
GB-wall	8	0.246	8.246	10	0.469	10.47
Ureters	15	0.462	15.46	16	0.750	16.75
UB-wall	40	0.820	40.82	50	1.12	51.12
Ovaries	11	1.64	12.64	NA	NA	NA
Testes	NA	NA	NA	35	2.24	37.24
Prostate	NA	NA	NA	17	0.797	17.8
Uterus	80	2.46	82.46	NA	NA	NA
LN-Sys	119	6.82	126	148	9.32	158
Skin	2300	123	2423	3300	168	3468
Adipose	21410	348.5	21759	17230	280	17510
Muscle	17500	430.5	17931	29000	784	29784

693 *Note that in Tables A.1 and A.2 of *Publication 133* the Oral Mucosa source and target mass did not
694 differ and therefore did not leave room for the mass of blood in the oral mucosa. The SAFs accompanying
695 *Publication 133* did appropriately account for this blood component.

696 **3.3.2. Source region masses (details and origin)**

697 (63) Table 3.16 lists the source regions, their abbreviations, and the basis for the values of their
698 mass. It also provides information as to whether the source region is eligible to be part of Other
699 systemic tissue in a biokinetic model. Such tissues are assigned ‘Other’ compartment activity by
700 mass fraction if they are not explicitly invoked elsewhere in the systemic biokinetic model. Note
701 that although extrathoracic and thoracic lymph node regions are typically invoked in the HRTM
702 model, they will still be considered part of ‘Other’ if they do not appear in the systemic biokinetic

703 model. Tables 3.17 and 3.18 provide the source region masses for the age-dependent reference
 704 individuals.

705

706 Table 3.16. Source region names, abbreviations, and origin of reference masses.

Source region	Abbreviation	Eligible for 'Other'	Origin of mass
Oral cavity	O-cavity	No	No mass
Oral mucosa	O-mucosa	Yes	Scaled from tongue
Teeth surface	Teeth-S	No	No mass
Teeth volume	Teeth-V	Yes	Pub. 89-Table 2.8 [¶]
Tongue	Tongue	No	Pub. 89-Table 2.8 [¶]
Tonsils	Tonsils	Yes	Pub. 89-Table 2.8 [¶]
Slow clearance from oesophagus	Oesophag-s	No	No mass
Fast clearance from oesophagus	Oesophag-f	No	No mass
Oesophagus wall	Oesophag-w	Yes	Pub. 89-Table 2.8 [¶]
Stomach contents	St-cont	No	Pub. 89-Table 2.8 [¶]
Stomach mucosa	St-mucosa	No	Based on Pub. 100 [†]
Stomach wall	St-wall	Yes	Pub. 89-Table 2.8 [¶]
Small intestine contents	SI-cont	No	Pub. 89-Table 2.8 [¶]
Small intestine mucosa	SI-mucosa	No	Based on Pub. 100 [†]
Small intestine wall	SI-wall	Yes	Pub. 89-Table 2.8 [¶]
Small intestine villi	SI-villi	No	Based on Pub. 100 [†]
Right colon contents	RC-cont	No	Pub. 89-Table 2.8 [¶]
Right colon mucosa	RC-mucosa	No	Based on Pub. 100 [†]
Right colon wall	RC-wall	Yes	Pub. 89-Table 2.8 [¶]
Left colon contents	LC-cont	No	Pub. 89-Table 2.8 [¶]
Left colon mucosa	LC-mucosa	No	Based on Pub. 100 [†]
Left colon wall	LC-wall	Yes	Pub. 89-Table 2.8 [¶]
Rectosigmoid colon contents	RS-cont	No	Pub. 89-Table 2.8 [¶]
Rectosigmoid colon mucosa	RS-mucosa	No	Based on Pub. 100 [†]
Rectosigmoid colon wall	RS-wall	Yes	Pub. 89-Table 2.8 [¶]
Nasal vestibule skin surface	ET1-sur	No	No mass
Oropharynx mucous layer	ET2-sur	No	No mass
Oropharynx bound in epithelium	ET2-bnd	No	Based on Pub. 66

Source region	Abbreviation	Eligible for 'Other'	Origin of mass
Oropharynx sequestered in lamina propria	ET2-seq	No	Based on Pub. 66
Extrathoracic lymph nodes	LN-ET	Yes	Pub. 89-Table 5.3 [‡]
Bronchi surface transport	Bronchi	No	No mass
Bound in bronchi epithelium	Bronchi-b	No	Based on Pub. 66
Bronchi-sequestered in lamina propria	Bronchi-q	No	Based on Pub. 66
Bronchiole surface transport	Brchiole	No	No mass
Bronchiole-bound in epithelium	Brchiole-b	No	Based on Pub. 66
Bronchiole- sequestered in lamina propria	Brchiole-q	No	Based on Pub. 66
Alveolar interstitium	ALV	No	Pub. 89-Table 5.3 ^{‡,¶}
Thoracic lymph nodes	LN-Th	Yes	Pub. 89-Table 5.3 [‡]
Lungs	Lungs	No	Pub. 89-Table 2.8 [¶]
Adrenals	Adrenals	Yes	Pub. 89-Table 2.8 [¶]
Blood	Blood	No	Pub. 89-Table 2.8 [¶]
Cortical bone surface	C-bone-S	No	No mass
Cortical bone volume	C-bone-V	Yes	Pub. 89-Table 2.8 [¶]
Trabecular bone surface	T-bone-S	No	No mass
Trabecular bone volume	T-bone-V	Yes	Pub. 89-Table 2.8 [¶]
Cortical marrow	C-marrow	No	Pub. 89-Table 2.8 [¶]
Trabecular marrow	T-marrow	No	Pub. 89-Table 2.8 [¶]
Red marrow	R-marrow	Yes	Pub. 89-Table 2.8 [¶]
Yellow marrow	Y-marrow	Yes	Pub. 89-Table 2.8 [¶]
Brain	Brain	Yes	Pub. 89-Table 2.8 [¶]
Breast	Breast	Yes	Pub. 89-Table 2.8 [¶] and Pub. 143 ^{§§}
Lens of the eye	Eye-lens	Yes	Pub. 23, Pub. 143 ^{**}
Gall bladder wall	GB-wall	Yes	Pub. 89-Table 2.8 [¶]
Gall bladder contents	GB-cont	No	Pub. 89-Table 2.8 [¶]
Heart wall	Ht-wall	Yes	Pub. 89-Table 2.8 [¶]
Kidneys	Kidneys	Yes	Pub. 89-Table 2.8 [¶]
Liver	Liver	Yes	Pub. 89-Table 2.8 [¶]
Systemic lymph nodes	LN-Sys	Yes	Derived from Pub. 66 and 89 ^{††}

Source region	Abbreviation	Eligible for ‘Other’	Origin of mass
Ovaries	Ovaries	Yes	Pub. 89-Table 2.8 [¶]
Pancreas	Pancreas	Yes	Pub. 89-Table 2.8 [¶]
Pituitary gland	P-gland	Yes	Pub. 89-Table 2.8 [¶]
Prostate	Prostate	Yes	Pub. 89-Table 2.8 [¶]
Salivary glands	S-glands	Yes	Pub. 89-Table 2.8 [¶]
Skin	Skin	Yes	Pub. 89-Table 2.8 [¶]
Spleen	Spleen	Yes	Pub. 89-Table 2.8 [¶]
Testes	Testes	Yes	Pub. 89-Table 2.8 [¶]
Thymus	Thymus	Yes	Pub. 89-Table 2.8 [¶]
Thyroid	Thyroid	Yes	Pub. 89-Table 2.8 [¶]
Ureters	Ureters	Yes	Pub. 89-Table 2.8 [¶]
Urinary bladder wall	UB-wall	Yes	Pub. 89-Table 2.8 [¶]
Urinary bladder contents	UB-cont	No	Computed for this work
Uterus	Uterus	Yes	Pub. 89-Table 2.8 [¶]
Adipose	Adipose	Yes	Modified from Pub. 89-Table 2.8 [#]
Cartilage	Cartilage	Yes	Pub. 89-Table 2.8 [¶]
Muscle	Muscle	Yes	Pub. 89-Table 2.8 [¶]
Nasal vestibule wall	ET1-wall	Yes	Based on Pub. 66
Oropharynx wall	ET2-wall	Yes	Based on Pub. 66
Lung tissue (no blood)	Lung-Tis	Yes	Pub. 89-Table 2.8 [¶]
Respiratory tract airways	RT-air	No	No mass

707 †The stylised geometries described in *Publication 100* (ICRP 2006).

708 ‡Contained in Table 5.3 of *Publication 89* (ICRP 2002). Note that the ALV mass is inclusive of blood. See
 709 the target mass tables if interested in the parenchyma mass of the alveolar tissue. The lung mass with and
 710 without blood in Table 2.8 of *Publication 89* is not consistent with alveolar masses inclusive of blood
 711 provided in Table 5 of *Publication 66* and Table 5.3 of *Publication 89*.

712 §Contained in Table 6 of Wayson et al. (2018).

713 ¶Contained in Table 2.8 of *Publication 89* (ICRP 2002)

714 ***Publication 23* (ICRP 1975) describes age-dependency for the lens of the eye but does not provide
 715 reference values. The phantom mass in *Publication 143* was chosen for the target mass of the lens.

716 ††*Publication 89* (ICRP 2002) describes the age dependency of the total lymph node mass. This information
 717 combined with the information in *Publication 66* (ICRP 1994) on the masses of the extrathoracic and
 718 thoracic lymph nodes was used to calculate the systemic lymph node mass.

719 #The adipose mass was adjusted from the values in Table 2.8 of *Publication 89* to maintain consistency
 720 with the total body mass.

721 §§*Publication 89* did not provide breast masses below 15 years, the masses from *Publication 143* (ICRP
 722 2020b) have been adopted at ages 10 years and younger.

723

724

725

726
727

Table 3.17. Masses for source regions in the reference newborn, 1-year old, 5-year old, and 10-year old (female and male).

Source region	Source region mass (g) (female/male)			
	Newborn	1-y	5-y	10-y
O-cavity	NA	NA	NA	NA
O-mucosa	1.608	4.679	8.715	14.70
Teeth-S	NA	NA	NA	NA
Teeth-V	0.700	5.00	15.0	30.0
Tongue	3.50	10.0	19.0	32.0
Tonsils	0.100	0.500	2.00	3.00
Oesophag-s	NA	NA	NA	NA
Oesophag-f	NA	NA	NA	NA
Oesophag-w	2.00	5.00	10.0	18.0
St-cont	40.0	67.0	83.0	117.0
St-mucosa	1.442	1.744	2.281	2.760
St-wall	7.00	20.0	50.0	85.0
SI-cont	56.0	93.0	117.0	163.0
SI-mucosa	5.332	9.567	15.77	23.29
SI-wall	30.0	85.0	220	370
SI-villi	0.5778	1.637	4.238	7.127
RC-cont	24.0	40.0	50.0	70.0
RC-mucosa	4.158	7.110	10.21	13.80
RC-wall	7.00	20.0	49.0	85.0
LC-cont	12.0	20.0	25.0	35.0
LC-mucosa	3.968	6.237	8.996	12.25
LC-wall	7.00	20.0	49.0	85.0
RS-cont	12.0	20.0	25.0	35.0
RS-mucosa	2.249	4.178	5.938	7.687
RS-wall	3.00	10.0	22.0	40.0
ET1-sur	NA	NA	NA	NA
ET2-sur	NA	NA	NA	NA
ET2-bnd	0.2911	0.5109	1.044	1.538
ET2-seq	0.05305	0.09308	0.1902	0.2802
LN-ET	0.700	2.10	4.10	6.80
Bronchi	NA	NA	NA	NA
Bronchi-b	0.443	0.6390	0.9186	1.238
Bronchi-q	0.0740	0.1080	0.1552	0.2092
Brchiole	NA	NA	NA	NA
Brchiole-b	0.982	1.506	2.384	3.262
Brchiole-q	0.246	0.3854	0.6103	0.8351
ALV	52.0	150	300	500
LN-Th	0.700	2.10	4.10	6.80
Lungs	60.0	150	300	500
Adrenals	6.00	4.00	5.00	7.00
Blood	290	530	1500	2500
C-bone-S	NA	NA	NA	NA
C-bone-V	135	470	1010	1840
T-bone-S	NA	NA	NA	NA
T-bone-V	35.0	120	250	460

Source region	Source region mass (g) (female/male)			
	Newborn	1-y	5-y	10-y
C-marrow	2.818	6.546	30.83	99.51
T-marrow	47.18	163.5	469.2	1160
R-marrow	50.0	150	340	630
Y-marrow	0	20.0	160	630
Brain	380	950	1180/1310	1220/1400
Breast	0.0800	0.430	0.940	7.53/7.12
Eye-lens	0.130	0.220	0.330	0.350
GB-wall	0.500	1.40	2.60	4.40
GB-cont	2.80	8.00	15.0	26.0
Ht-wall	20.0	50.0	85.0	140
Kidneys	25.0	70.0	110	180
Liver	130	330	570	830
LN-Sys	12.9	20.8	40.6	67.3
Ovaries	0.300	0.800	2.00	3.50
Pancreas	6.00	20.0	35.0	60.0
P-gland	0.100	0.150	0.250	0.350
Prostate	0.800	1.00	1.20	1.60
S-glands	6.00	24.0	34.0	44.0
Skin	175	350	570	820
Spleen	9.50	29.0	50.0	80.0
Testes	0.850	1.50	1.70	2.00
Thymus	13.0	30.0	30.0	35.0/40.0
Thyroid	1.30	1.80	3.40	7.90
Ureters	0.770	2.20	4.20	7.00
UB-wall	4.00	9.00	16.0	25.0
UB-cont	15.0	25.0	65.0	75.0
Uterus	4.00	1.50	3.00	4.00
Adipose	1016/1019	4028/4027	5831/5703	9063/8882
Cartilage	130	360	600	820
Muscle	800	1900	5600	11000
ET1-wall	0.3443	0.6041	1.234	1.819
ET2-wall	0.3443	0.6041	1.234	1.819
Lung-Tis	26.79	78.26	150.1	243.8
RT-air	NA	NA	NA	NA

728
729
730

Table 3.18. Masses for source regions in the reference 15-year-old and adult (female and male).

Source region	Source region mass (g)			
	15-year female	15-year male	Adult female	Adult male
O-cavity	NA	NA	NA	NA
O-mucosa	24.49	25.60	22.45	35.83
Teeth-S	NA	NA	NA	NA
Teeth-V	35.0	45.0	40.0	50.0
Tongue	53.0	56.0	60.0	73.0
Tonsils	3.00	3.00	3.00	3.00
Oesophag-s	NA	NA	NA	NA
Oesophag-f	NA	NA	NA	NA

Source region	Source region mass (g)			
	15-year female	15-year male	Adult female	Adult male
Oesophag-w	30.0	30.0	35.0	40.0
St-cont	200	200	230	250
St-mucosa	3.612	3.612	4.639	4.639
St-wall	120	120	140	150
SI-cont	280	280	280	350
SI-mucosa	34.98	34.98	34.32	36.96
SI-wall	520	520	600	650
SI-villi	10.02	10.02	12.52	12.52
RC-cont	120	120	160	150
RC-mucosa	17.73	17.73	17.73	20.10
RC-wall	122	122	145	150
LC-cont	60.0	60.0	80.0	75.0
LC-mucosa	17.26	17.26	17.26	18.75
LC-wall	122	122	145	150
RS-cont	60.0	60.0	80.0	75.0
RS-mucosa	10.39	10.39	10.39	11.28
RS-wall	56.0	56.0	70.0	70.0
ET1-sur	NA	NA	NA	NA
ET2-sur	NA	NA	NA	NA
ET2-bnd	2.087	2.307	2.137	2.472
ET2-seq	0.3803	0.4204	0.3894	0.4504
LN-ET	11.0	12.0	12.0	15.0
Bronchi	NA	NA	NA	NA
Bronchi-b	1.518	1.638	1.552	1.727
Bronchi-q	0.2564	0.2767	0.2622	0.2918
Brchiole	NA	NA	NA	NA
Brchiole-b	4.015	4.517	4.703	4.891
Brchiole-q	1.028	1.156	1.204	1.252
ALV	800	860	900	1100
LN-Th	11.0	12.0	12.0	15.0
Lungs	750	900	950	1200
Adrenals	9.00	10.0	13.0	14.0
Blood	3500	4800	4100	5600
C-bone-S	NA	NA	NA	NA
C-bone-V	2960	3240	3200	4400
T-bone-S	NA	NA	NA	NA
T-bone-V	740	810	800	1100
C-marrow	158.5	201.5	258.0	279.0
T-marrow	2222	2359	2442	3371
R-marrow	1000	1080	900	1170
Y-marrow	1380	1480	1800	2480
Brain	1300	1420	1300	1450
Breast	250	15.0	500	25.0
Eye-lens	0.400	0.490	0.400	0.400
GB-wall	7.30	7.70	8.00	10.0
GB-cont	42.0	45.0	48.0	58.0
Ht-wall	220	230	250	330
Kidneys	240	250	275	310

Source region	Source region mass (g)			
	15-year female	15-year male	Adult female	Adult male
Liver	1300	1300	1400	1800
LN-Sys	108.8	118.7	118.7	148.4
Ovaries	6.00	NA	11.0	NA
Pancreas	100	110	120	140
P-gland	0.500	0.500	0.600	0.600
Prostate	NA	4.30	NA	17.0
S-glands	65.0	68.0	70.0	85.0
Skin	1700	2000	2300	3300
Spleen	130	130	130	150
Testes	NA	16.0	NA	35.0
Thymus	30.0	35.0	20.0	25.0
Thyroid	12.0	12.0	17.0	20.0
Ureters	12.0	12.0	15.0	16.0
UB-wall	35.0	40.0	40.0	50.0
UB-cont	85.0	85.0	200	200
Uterus	30.0	NA	80.0	NA
Adipose	17660	11340	21410	17230
Cartilage	920	1140	900	1100
Muscle	17000	24000	17500	29000
ET1-wall	2.468	2.728	2.526	2.923
ET2-wall	2.468	2.728	2.526	2.923
Lung-Tis	379.7	409.3	420.0	500.0
RT-air	NA	NA	NA	NA

731

732

733
734

4. MODELS AND METHODS FOR ENERGY ABSORPTION COMPUTATION

735
736
737
738

(64) To compute SAFs, the absorbed fraction requires the computation of the energy absorption in each target per energy emitted from each source region. This computation is performed in a computational model.

739
740
741
742
743

(65) For a large number of source-target geometries, the computational models are the reference voxel phantoms provided in *Publications 110* and *143* (ICRP 2009, 2020b). But there are many smaller regions where a finer, detailed model is required. These include the alimentary tract, the respiratory tract, and the skeleton. The following sections describe the models and the methods used to compute specific absorbed fractions in those models.

744

4.1. Reference voxel phantoms

745

4.1.1. Summary and definition

746
747
748
749
750
751

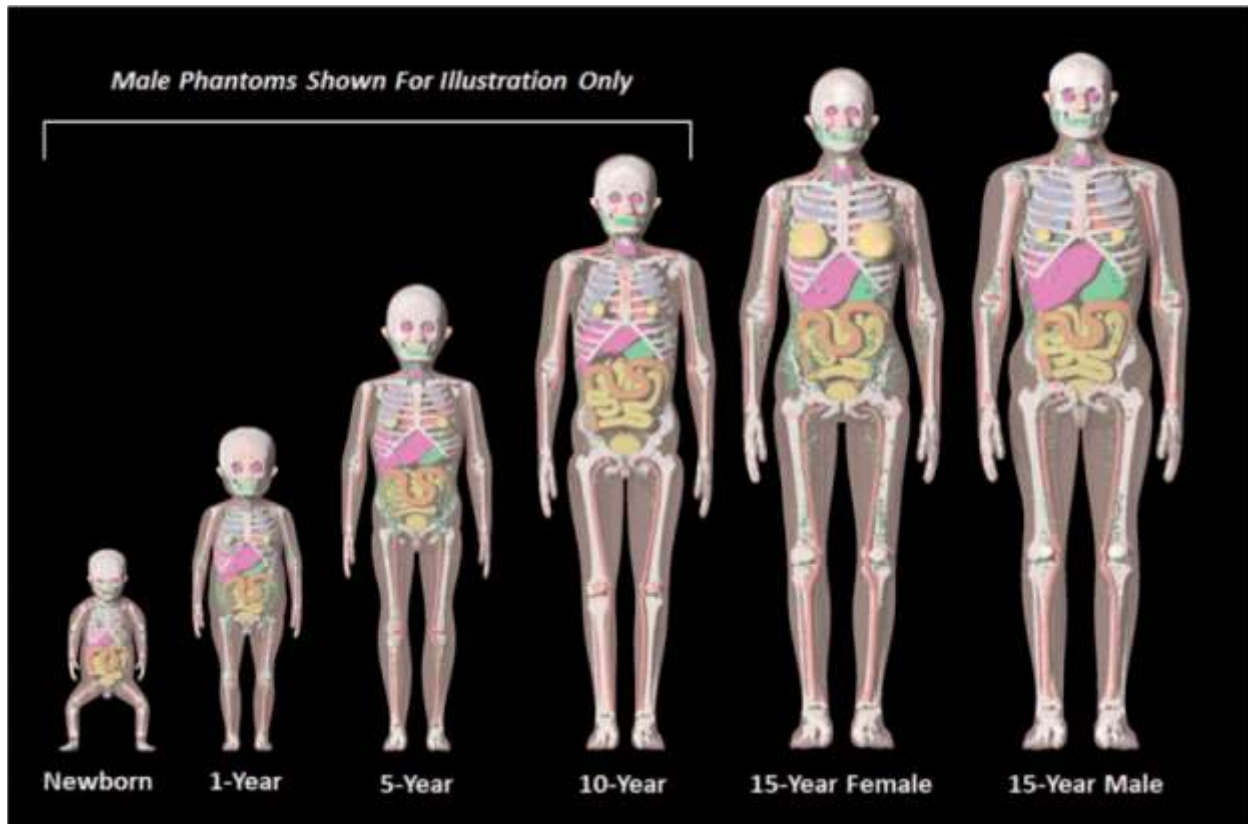
(66) The reference voxel phantoms for the adult are found in *Publication 110* and were adjusted to conform with reference parameters from individuals of similar size (Zankl and Wittmann 2001; Zankl 2005). The development of the phantoms is detailed in *Publication 110* and the use of the phantom to compute SAFs is described in detail in *Publication 133*. Since the SAFs in *Publication 133* are adopted as published for this work, the focus in this section will be on the use of the *Publication 143* phantoms to compute SAFs for the paediatric reference individuals.

752
753
754
755

(67) The paediatric reference computational phantoms were based on a series of phantoms developed at the University of Florida and the US National Cancer Institute (Lee et al. 2010). The details of the adjustments made to the phantoms are described in *Publication 143*. The voxelised phantoms are depicted in Fig. 4.1.

756
757
758
759
760
761

(68) While the masses and sizes of the *Publication 143* phantoms are unique, they were developed to have consistent descriptors as those in *Publication 110* (e.g. organs, organ ID numbers, blood contribution to elemental compositions). Body morphometry of the *Publication 143* phantoms were based on values provided in *Publication 89*. The phantoms are based on medical image data of real individuals consistent with the reference anatomical information in *Publication 89*.



762
763 Fig. 4.1. ICRP series of reference paediatric voxel computational phantoms from *Publication 143*.

764 4.1.2. Photons

765 (69) Schwarz et al. (2021b) contains the details for the computation of photon SAFs in the
766 reference paediatric phantoms of *Publication 143*. Monte Carlo photon radiation transport
767 simulations were performed using MCNPX v2.7 (Pelowitz 2011) in each paediatric reference
768 phantom. In each phantom, 60 tissues served as source and/or target regions. When a desired tissue
769 region did not exist in the reference voxel phantom, surrogate tissues were used to represent the
770 desired tissue. For example, the reference phantoms do not model the thin stem cell target regions
771 in the alimentary tract. The entire stomach wall is thus treated as a surrogate for the stomach stem
772 target.

773 (70) Monoenergetic photon emissions were simulated from source regions across a logarithmic
774 energy grid from 10 keV to 10 MeV. For non-skeletal source regions, all voxels comprising a
775 source region were uniformly sampled. For skeletal source regions, non-uniform spatial sampling
776 was applied within the various tissues of the paediatric skeleton. As with the *Publication 110* adult
777 phantoms, each of the *Publication 143* phantoms' skeletal sites may be composed of both
778 spongiosa (representing a mixture of marrow cavities and bone trabeculae) and cortical bone (the
779 bone cortex). The spongiosa represents four source regions – active marrow (red marrow), inactive
780 marrow (yellow marrow), trabecular bone surface, and trabecular bone volume. Spongiosa regions
781 exist in bones of both the axial and appendicular skeleton. The cortical bone surface and cortical
782 bone volume source regions are simulated as emissions from cortical bone voxels. A table in
783 Schwarz et al. (2021b) contains the fractional distribution of the skeletal tissue regions based on
784 previously published skeletal tissue models (Pafundi et al. 2010; Wayson 2012).

785 (71) Energy absorption in red marrow and the bone endosteum were computed for photons by
 786 coupling energy-dependent fluence-to-absorbed dose response functions (Wayson 2012) to
 787 energy-dependent photon fluences scored in the spongiosa and medullary cavities of the long
 788 bones. The response functions were derived as described in Johnson et al. (2011). The calculation
 789 of the specific absorbed fraction, Φ , to red marrow, RM, and the bone endosteum target, BS (short
 790 for bone surface), from photon emission in a source region, r_S , are given by Eqs. (4.1) and (4.2).
 791

$$\Phi(\text{R-marrow} \leftarrow r_S, E_0) = \frac{1}{E_0} \sum_x f_{\text{RM},x} \sum_i \text{DRF}(\text{RM}, E_i, x) \Phi_{\text{ph}}(\text{Sp/MC} \leftarrow r_S, E_i, x) \quad (4.1)$$

$$\Phi(\text{Endost-BS} \leftarrow r_S, E_0) = \frac{1}{E_0} \sum_x f_{\text{BS},x} \sum_i \text{DRF}(\text{BS}, E_i, x) \Phi_{\text{ph}}(\text{Sp/MC} \leftarrow r_S, E_i, x) \quad (4.2)$$

792
 793 (72) The emitted photon energy is E_0 and $\Phi_{\text{ph}}(\text{Sp/MC} \leftarrow r_S, E_i, x)$ is the scored photon fluence
 794 within the spongiosa (Sp) or medullary cavity (MC) region of bone site x at photon energy E_i . The
 795 skeletal dose response functions, $\text{DRF}(\text{RM}, E_i, x)$ and $\text{DRF}(\text{BS}, E_i, x)$, provide the absorbed
 796 dose per unit photon fluence for red marrow and bone endosteum targets, respectively, at each
 797 photon energy and within each bone site. The fractional masses of red marrow and bone endosteum
 798 within each bone site are provided by f . Tabulated values for the dose response functions and the
 799 fractional masses are provided in the electronic download which accompanies this publication and
 800 are described in Annex A.

801 (73) The inclusion of a blood source region in the latest ICRP biokinetic models necessitates
 802 computation of SAFs for emissions from a blood source distributed appropriately across the
 803 reference voxel phantoms. Source regions for a blood source should include blood in large vessels,
 804 heart contents, and blood perfusing tissue. For the latter region, weighting of all blood-containing
 805 tissue source region SAFs can be used to compute a blood SAF as detailed in Eq. (4.3),
 806

$$\Phi(r_T \leftarrow \text{Blood}, E_0) = \sum_S f_{\text{Blood},S} \Phi(r_T \leftarrow r_S, E_0) \quad (4.3)$$

807 where $f_{\text{Blood},S}$ is the fraction of the body's blood assigned in a source region and Φ is the photon
 808 SAF for a given source/target combination. The fractional blood distribution is published in
 809 Wayson et al (2018). Further details on the application of this blood distribution to the phantoms
 810 are described in Schwarz et al (2021b).

811 (74) For those crossfire geometries at lower energies when relative error in energy deposition
 812 tallies exceed 5% (photons of energies at or below 30 keV) data smoothing was performed. At the
 813 lowest energies, log-log extrapolation to theoretical zero-energy limiting values (see section 5.2)
 814 was performed. Details of the smoothing methods and when it was applied in each phantom are
 815 found in Schwarz et al (2021b)

816 4.1.3. Electrons

817 (75) Schwarz et al. (2021a) contains the details for the computation of electron SAFs in the
 818 reference paediatric phantoms. Until *Publication 133* for the adult and this publication for
 819 paediatric individuals, electron absorbed fractions were generally treated as either unity for self-

820 irradiation geometries or zero for crossfire geometries. In *Publication 133* and in this work, Monte
 821 Carlo transport of electrons in the reference phantoms allows for non-unity, non-zero absorbed
 822 fractions which vary with electron energy. Emitted electron energy is allowed to escape the source
 823 region either in the form of electron kinetic energy or via bremsstrahlung x-rays resulting from
 824 electron radiative energy losses.

825 (76) The same logarithmic energy grid used for photons is used for electron SAFs. Collisional
 826 and radiative components of the electron SAFs are computed independently with the radiative
 827 contribution utilizing previously computed photon SAFs (Wayson et al. 2012; Schwarz et al.
 828 2021a). Monte Carlo simulations of the electron transport in the phantoms were performed using
 829 MCNPX v2.7 (Pelowitz 2011). The description of sampling source regions and computing energy
 830 absorption in target regions are the same as those described in the previous section for photons.

831 (77) Schwarz et al (2021a) computed collisional electron energy absorption during the electron
 832 Monte Carlo transport. When a photon associated with bremsstrahlung x-ray production was
 833 created, its energy and source region was scored to create an energy distribution in each region.
 834 This distribution was then subsequently coupled to photon SAFs to compute the SAFs associated
 835 with radiative losses. The collisional and radiative SAFs were then summed to arrive at the total
 836 electron SAFs presented in this work. The radiative component of the electron SAF was computed
 837 as:

$$\Phi_R(r_T \leftarrow r_S, E_0) = \frac{1}{N_e E_0^e} \sum_i E_i^P \Phi^P(r_T \leftarrow r_S, E_i^P) \quad (4.4)$$

838 where $\Phi^P(r_T \leftarrow r_S, E_i^P)$ is the photon SAF for the source/target pair indexed to the x-ray photon
 839 energy E_i^P . The denominator is the product of the number of electrons simulated, N_e , and the
 840 emitted electron energy, E_0^e . This approach necessarily presumes that all bremsstrahlung x-rays are
 841 created interior to the source region, thus neglecting cases where the x-ray was generated by an
 842 electron which had previously exited the source region boundary. However, in a study by Wayson
 843 et al. (2012) using a University of Florida newborn phantom, it was shown that this two-stage
 844 approach to computing the electron SAF was statistically comparable to that using full electron
 845 transport with explicit bremsstrahlung x-ray production and transport.

846 (78) The reference phantoms were not used to derive SAFs for electrons emitted from within
 847 skeletal tissues irradiating skeletal targets. The models used for these intra-skeletal geometries are
 848 described in section 4.4.2. For electrons emitted from outside the skeleton, the collisional
 849 component of the SAF to skeletal targets $\Phi_C(\text{R-marrow} \leftarrow r_S, E_0)$ was computed as shown in Eqs.
 850 (4.5) and (4.6). The fraction of red marrow (or bone endosteum), $f_{\text{RM},x}$ in each skeletal site, x , is
 851 found in Schwarz et al (2021b). The energy deposited in the spongiosa or medullary cavity region
 852 for each skeletal site is E_x .

$$\Phi_C(\text{R-marrow} \leftarrow r_S, E_0) = \frac{1}{E_0} \sum_x f_{\text{RM},x} \left(\frac{E_x}{m_{\text{RM},x}} \right) \quad (4.5)$$

$$\Phi_C(\text{Endost-BS} \leftarrow r_S, E_0) = \frac{1}{E_0} \sum_x f_{\text{BS},x} \left(\frac{E_x}{m_{\text{BS},x}} \right) \quad (4.6)$$

853
 854 (79) Data smoothing of electron SAFs was found to be unnecessary since the collisional
 855 component of the electron SAF had very small statistical errors and the radiative component

856 utilised photon SAFs which had already been smoothed where necessary. Low energy
857 interpolation to theoretical zero-energy SAFs was performed in the same manner (log-log) as
858 described previously for photons.

859 4.1.4. Neutrons from spontaneous fission

860 (80) Griffin et al. (2022) contains the details for the computation of SAFs for fission-spectrum
861 neutrons in the reference paediatric phantoms. Neutron SAFs in this publication address 28
862 radionuclides which undergo spontaneous fission with a branching fraction greater than 1×10^{-9}
863 per nuclear transformation (ICRP 2008a). Unlike the other SAFs in this publication, neutron SAFs
864 are computed and tabulated in a manner specific to the radionuclide rather than specific to a grid
865 of monoenergetic emissions. SAFs were calculated for ^{252}Cf using MCNP6 (version 6.1) (Pelowitz
866 2013) in major source regions of the reference voxel phantoms; in other source regions, ^{252}Cf SAFs
867 were derived using a point-kernel approach. For the remaining 27 radionuclides, the SAFs for ^{252}Cf
868 were scaled using normalization factors to account for difference in soft tissue kerma and the
869 average energy of an emitted neutron.

870 (81) Table 4.1 summarises the decay data information for the selected radionuclides (ICRP
871 2008a). The spontaneous fission branching fraction ranges from 1.37×10^{-9} (^{236}Pu) to 0.997 (^{254}Cf)
872 per nuclear transformation. The average number of neutrons emitted per fission ranges from 2.01
873 (^{238}U) to 4.01 (^{256}Fm) per fission. The average emitted neutron energy per fission ranges from 3.39
874 (^{238}U) to 8.99 (^{254}Cf) MeV. Note the energy associated with fission fragments greatly exceeds that
875 of the neutrons. For example, the energy of the ^{256}Fm fission fragments is 194.56 MeV. These
876 fragments are assumed to have the same SAF as a 2.0 MeV alpha particle (local absorption).

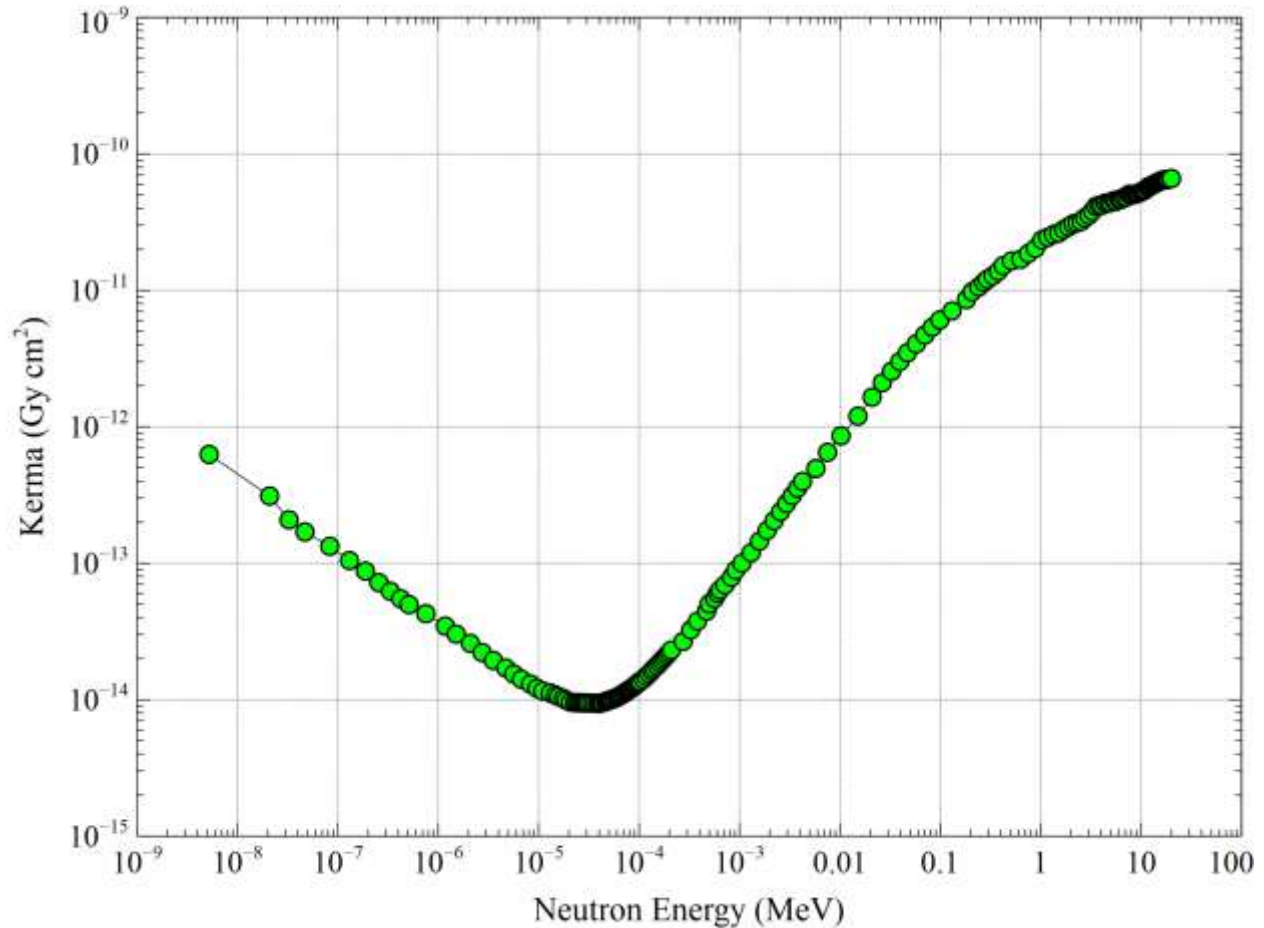
877 (82) The neutron SAFs are tabulated by radionuclide and address the energy spectrum of the
878 fission neutrons. Since the neutron radiation weighting factors in *Publication 103* (ICRP 2007) are
879 energy-dependent, radiation weighting factors for neutrons from nuclides undergoing spontaneous
880 fission are needed which are nuclide-specific and spectrum-weighted. Nuclide-specific radiation
881 weighting factors were derived assuming the neutron radiation weighting factor expressions in
882 Table 2.3 and the Watt neutron fission spectra defined in *Publication 107*. The resultant spectrum-
883 weighted neutron radiation weighting factors are provided in Table 4.1.

884 (83) The right most column of Table 4.1 lists the nuclide specific normalization factor applied
885 to ^{252}Cf SAF values, which are independent of age. This factor accounts for the difference in soft
886 tissue kerma for the spontaneous fission neutron spectrum of the nuclides relative to that of ^{252}Cf .
887 Figure 4.2 shows the dependence of the kerma coefficient as a function of neutron energy. The
888 data of Fig. 4.2 was integrated over the Watt spectra and the resultant value normalised to that for
889 ^{252}Cf . This factor also accounts for the difference in the average energy of an emitted neutron from
890 the nuclide relative to that of ^{252}Cf . The radionuclide normalization factor ranges from 0.981
891 (^{240}Cm) to 1.198 (^{238}U).

892
893

894 Table 4.1. Properties of spontaneous fission emitting radionuclides

Radionuclide	Half-life	Fission probability per nuclear transformation n	Mean neutrons emitted per fission	Mean neutron energy per fission (MeV)	Spectrum-weighted radiation weighting factor	Radionuclide normalization factor
²³⁸ U	4.468 × 10 ⁹ y	5.45 × 10 ⁻⁷	2.01	3.39	17.49	1.198
²³⁶ Pu	2.858 y	1.37 × 10 ⁻⁹	2.13	4.77	16.67	1.017
²³⁸ Pu	87.7 y	1.85 × 10 ⁻⁹	2.22	4.49	16.99	1.080
²⁴⁰ Pu	6564 y	5.75 × 10 ⁻⁸	2.16	4.18	17.12	1.108
²⁴² Pu	3.75 × 10 ⁵ y	5.54 × 10 ⁻⁶	2.15	4.22	17.07	1.099
²⁴⁴ Pu	8.00 × 10 ⁷ y	1.21 × 10 ⁻³	2.30	4.06	17.37	1.168
²⁴⁰ Cm	27 d	3.90 × 10 ⁻⁸	2.39	5.69	16.47	0.981
²⁴² Cm	162.8 d	6.37 × 10 ⁻⁸	2.52	5.28	16.88	1.058
²⁴⁴ Cm	18.1 y	1.371 × 10 ⁻⁶	2.69	5.68	16.85	1.053
²⁴⁵ Cm	8.50 × 10 ³ y	6.10 × 10 ⁻⁹	2.87	6.09	16.84	1.050
²⁴⁶ Cm	4.76 × 10 ³ y	2.63 × 10 ⁻⁴	3.18	6.57	16.92	1.066
²⁴⁸ Cm	3.84 × 10 ⁵ y	8.39 × 10 ⁻²	3.11	6.08	17.09	1.102
²⁵⁰ Cm	8300 y	7.40 × 10 ⁻¹	3.31	6.07	17.27	1.142
²⁴⁶ Cf	35.7 h	2.50 × 10 ⁻⁶	3.10	7.16	16.57	0.999
²⁴⁸ C	334 d	2.90 × 10 ⁻⁵	3.34	7.73	16.56	0.997
²⁴⁹ C	351 y	5.02 × 10 ⁻⁹	3.41	7.88	16.57	0.999
²⁵⁰ Cf	13.08 y	7.70 × 10 ⁻⁴	3.53	8.15	16.57	0.999
²⁵² C	2.645 y	3.092 × 10 ⁻²	3.765	8.68	16.57	1.000
²⁵⁴ Cf	60.5 d	9.969 × 10 ⁻¹	3.89	8.99	16.57	0.999
²⁵³ Es	20.47 d	8.90 × 10 ⁻⁸	3.93	7.87	17.02	1.087
²⁵⁴ Es	275.7 d	3.00 × 10 ⁻⁸	3.95	7.91	17.02	1.087
^{254m} E	39.3 h	4.50 × 10 ⁻⁴	3.95	7.91	17.02	1.087
²⁵⁵ Es	39.8 d	4.50 × 10 ⁻⁵	3.97	7.95	17.02	1.087
²⁵² Fm	25.39 h	2.30 × 10 ⁻⁵	3.90	7.81	17.02	1.087
²⁵⁴ F	3.240 h	5.92 × 10 ⁻⁴	3.96	7.93	17.02	1.087
²⁵⁵ Fm	20.07 h	2.30 × 10 ⁻⁷	3.73	7.47	17.02	1.087
²⁵⁶ Fm	157.6 m	9.19 × 10 ⁻¹	4.01	8.03	17.02	1.087
²⁵⁷ Fm	100.5 d	2.10 × 10 ⁻³	3.85	7.71	17.02	1.087



896
897 Fig. 4.2. Neutron kerma coefficient (Gy cm²) in soft tissue as a function of neutron energy
898 (Howerton 1986).

899 4.1.5. Alpha particles

900 (84) Unlike electron transport simulations in the reference phantoms, alpha particle transport
901 simulations are unnecessary due to the short range of the alpha particles compared to the size of
902 the source regions. For such geometries, the alpha absorbed fraction is set to unity for self-
903 irradiation geometries and zero for non-overlapping source-target geometries (crossfire
904 geometries.) The resulting alpha SAF for the self-irradiation geometries is simply the inverse of
905 the target region mass. These values are applied at all alpha particle energies (up to 12 MeV.) The
906 kinetic energy of the recoiling nucleus, typically about 2% of alpha particle energy, is assumed to
907 inherit the SAF of a 2.0 MeV alpha particle (local absorption.)

908 4.2. Alimentary tract

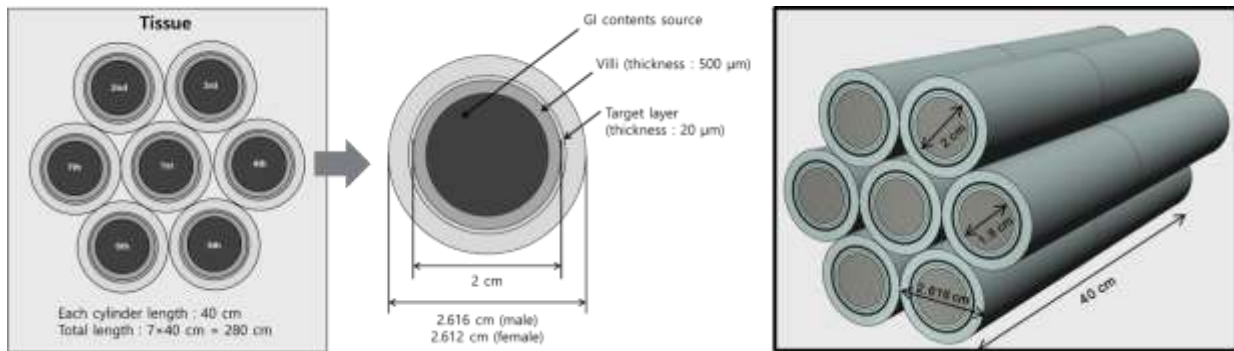
909 4.2.1. Summary and definition

910 (85) The computational models used to compute SAFs within the alimentary tract are based on
911 the geometrical definitions provided in Section 7 of *Publication 100* (ICRP 2006). For each region

912 in the alimentary tract, information is provided on the simplified geometrical shape and the sizes
 913 of these regions. Tables 3.6 and 3.7 summarise some of this information for the various target
 914 regions. Similar information is provided in *Publication 100* which define the location and size of
 915 various source regions.

916 **4.2.2. Electrons and Alphas**

917 (86) Annex F of *Publication 100* provided electron SAF values based upon Monte Carlo
 918 radiation transport simulation in the geometrical models. Similar simulations were not provided
 919 for alpha particles. For *Publication 133*, new radiation transport simulations were performed for
 920 both electron and alpha particles using the geometries from *Publication 100* with one modelling
 921 improvement made to the small intestine. Rather than modelling the small intestine as a single
 922 cylinder, the cylinders were stacked in a hexagonal array to allow for energy deposition across one
 923 segment of the small intestine to another, nearby. Figure 4.3 depicts the geometry used for the
 924 small intestine.
 925



926 Fig. 4.3. Schematic of the folded small intestine model used to allow for electron crossfire.
 927
 928

929 (87) The same approach used in *Publication 133* has been extended in this work using the age-
 930 specific geometry information provided in *Publication 100* for both electrons (up to 10 MeV) and
 931 alpha particles (up to 12 MeV).

932 **4.2.3. Photons and Neutrons**

933 (88) For photons and neutrons, surrogate tissues in the reference phantom were used to
 934 represent the small source and target regions in the alimentary tract. For example, the SAF to
 935 desired stem cell targets is considered to be the same as the SAF to the encompassing,
 936 corresponding wall region. Similarly, a photon or neutron source emanating from an alimentary
 937 mucosal region is treated as originating from the wall in the reference voxel phantom.

938 **4.3. Respiratory tract**

939 **4.3.1. Summary and definition**

940 (89) *Publication 66* (ICRP 1994) contains information on the morphometrical model used to
 941 define computational models for regions inside the respiratory tract. While the publication contains

942 some information on age and sex dependency, for dosimetric modelling the cross-sectional
943 dimensions of the airway regions (airway and wall thicknesses) have been treated as independent
944 of age and sex. Thus, the absorbed fractions computed for the adults are applied at all younger
945 ages. The SAF then changes by the mass of the target region which is dependent on age and sex.

946 4.3.2. Electrons and Alphas

947 (90) Section 5 of *Publication 133* describes the adoption of respiratory tract SAFs previously
948 provided in *Publication 66* in Annexe H. In the first part of the OIR Series, *Publication 130* (ICRP
949 2015), revisions were made to the respiratory tract model. The original HRTM included particle-
950 size-dependent slow clearance compartments which were eliminated in the revision. The revised
951 source region is taken to be uniformly distributed throughout both the gel and sol layers of
952 *Publication 66*. The weights for the relative thickness of the gel and sol are 5/11 and 6/11,
953 respectively for the bronchial region and 1/3 and 2/3, respectively for the bronchiolar region.

954 (91) *Publication 133* also describes the addition of new electron SAFs for geometries based on
955 radiation transport in the reference voxel phantoms. This was used for alveolar interstitial and
956 extrathoracic lymph node source regions. Alpha SAFs were not updated in this manner but were
957 instead adopted as they appear in *Publication 66*.

958 4.3.3. Photons and Neutrons

959 (92) For photons and neutrons, surrogate tissues in the reference phantom were used to
960 represent the small source and target regions in the respiratory tract. For example, the SAFs to
961 secretory targets in the bronchi were considered to be the same as the SAFs to the bronchi wall
962 region. Similarly, a photon or neutron source emanating from the alveolar interstitial is treated as
963 coming from the whole lung in the reference voxel phantom.

964 4.4. Skeleton

965 4.4.1. Summary and definition

966 (93) *Publication 11* (ICRP 1968) defined three cellular regions at risk for radiogenic damage
967 within the skeleton: cells among the osteogenic cells on bone surfaces, haematopoietic marrow,
968 and certain epithelial cells close to bone surfaces. The same publication defined the dose to the
969 latter category as averaged over the region "...from 5 to 10 μm from the trabecular surface."
970 *Publication 26* (ICRP 1977) includes a recommendation that the "...dose equivalent in bone
971 should apply to the endosteal cells and cells on bone surfaces, and should be calculated as an
972 average over tissue up to a distance of 10 μm from the relevant bone surfaces." *Publication 30*
973 (ICRP 1979) uses the 10 μm recommendation from *Publication 26*.

974 (94) More recently, studies have shown that the cells at risk for bone cancer induction are
975 localised up to 50 μm from trabecular and interior cortical bone surfaces (Gossner et al. 2000;
976 Gossner 2003; Bolch et al. 2007). In this work and in *Publication 133*, the bone endosteum target
977 is considered to be all marrow tissue within 50 μm of a trabecular surface or interior cortical bone
978 surface along the shafts of the long bones.

979 (95) Data suggest haematopoietic stem cells are found preferentially near trabecular bone
980 surfaces (Watchman; et al. 2007; Bourke et al. 2009). Nevertheless, in this work as in *Publication*

133, dosimetric modelling treats the cells as uniformly distributed among the marrow spaces. The models used do explicitly treat red and yellow marrow as separate, interspersed regions within the marrow spaces.

(96) *Publication 20* (ICRP 1973) describes the basis for the definition of skeletal source regions. Rowland (1966) describes rapidly-exchangeable calcium of bone as located only at bone surfaces which include cortical and trabecular endosteum, periosteum, and the surfaces of Haversian and Volkmann canals. “The calcium which lies within less than one micron from a bone surface was found to be sufficient to account for the size and location of the observed exchangeable pool” (ICRP 1973). *Publication 20* also describes the splitting of activity in the bone between cortical and trabecular regions of the skeleton as being split by the fraction of cortical/trabecular bone in the whole-body skeleton (80% / 20%). This value was later affirmed in *Publication 70* (ICRP 1995b).

(97) For the dosimetry in *Publication 30*, as well as the dosimetry here, radionuclides assumed to be on bone surfaces are modelled as uniformly spread in an infinitely thin layer over the relevant surfaces of bone. Importantly, *Publication 30* states “This assumption will result in an overestimate of the true committed dose equivalents received by bone surface cells and active bone marrow because it disregards burial of radioactive deposits by the deposition of new bone mineral.”

(98) The absorbed fraction of alpha particle energy emitted from skeletal regions was described in *Publication 30*. These values were used in subsequent ICRP dosimetry calculations. Several studies have found energy dependency in intraskeletal absorbed fractions for electrons (Spiers 1970; Eckerman et al. 1985; Bouchet et al. 1999; Eckerman and Stabin 2000; Jokisch et al. 2001; Patton et al. 2002; Shah et al. 2005; Kramer et al. 2012; Dant et al. 2013; Gao et al. 2017; Degteva et al. 2021) and alpha particles (Thorne 1976; Watchman et al. 2005; Hunt et al. 2007; Watchman and Bolch 2009). *Publication 106* (ICRP 2008b) represented the first departure from the electron absorbed fraction values of *Publication 30* and shown in Table 4.2. *Publication 106* used values for the adult from Stabin and Siegel (2003) which were based on work by Eckerman and Stabin (2000) and Bouchet et al. (2000) and was described in Stabin et al (2002). In *Publication 30*, the reference target masses for the red marrow and bone endosteum were 1.5 kg and 0.12 kg, respectively.

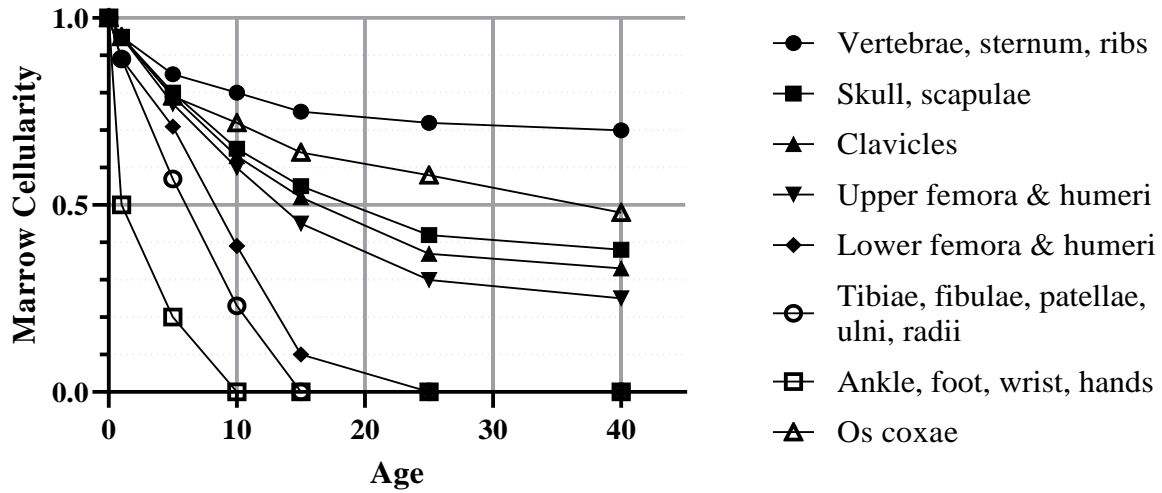
Table 4.2. Skeletal absorbed fractions in *Publication 30* (ICRP 1979) for the adult.

Radiation type	Target ← Source	Absorbed Fraction	Based on
Alpha particles	Endosteum ← Trab. bone volume	0.025	(Mays and Sears 1962; Thorne 1977)
	Endosteum ← Cortical bone-volume	0.010	(Spiers 1974)
	Red marrow ← Trab. bone volume	0.050	(Mays and Sears 1962; Thorne 1977)
	Red marrow ← Cortical bone volume	0.0	(Whitwell and Spiers 1976)
	Endosteum ← Trab. bone surface	0.25	(Mays and Sears 1962; Thorne 1977)

Radiation type	Target ← Source	Absorbed Fraction	Based on
	Endosteum ← Cortical bone surface	0.25	(Whitwell and Spiers 1976; Thorne 1977)
	Red marrow ← Trab. bone surface	0.50	Geometrical assumption
	Red marrow ← Cortical bone surface	0.0	Negligible compared to Trab. bone surface contribution
Electrons	Endosteum ← Trab. bone volume	0.025	(Spiers 1968, 1969, 1974; Whitwell and Spiers 1976)
	Endosteum ← Cortical bone-volume	0.015	
	Red marrow ← Trab. bone volume	0.35	
	Red marrow ← Cortical bone volume	0.0	
	Endosteum ← Trab. bone surface	0.25 $E < 0.2$ MeV 0.025 $E \geq 0.2$ MeV	
	Endosteum ← Cortical bone surface	0.25 $E < 0.2$ MeV 0.015 $E \geq 0.2$ MeV	
	Red marrow ← Trab. bone surface	0.50	
	Red marrow ← Cortical bone surface	0.0	

1013
1014
1015
1016
1017
1018
1019
1020

(99) Marrow cellularity is defined as the fraction of bone marrow volume that is haematopoietically active. Cellularity varies by location in the skeleton. Cellularity is also known to vary by age. In this work, reference values for marrow cellularity have been adopted from Table 41 of *Publication 70* (ICRP 1995b). The data is based largely on a review performed by Cristy (1981) of various studies of active marrow distribution. Fig. 4.4 contains a plot of these reference cellularities and how they vary by skeletal site and age.



1021
1022

Fig. 4.4. Reference marrow cellularity of *Publication 70* (ICRP 1995b) by skeletal site and age.

1023 **4.4.2. Electrons**

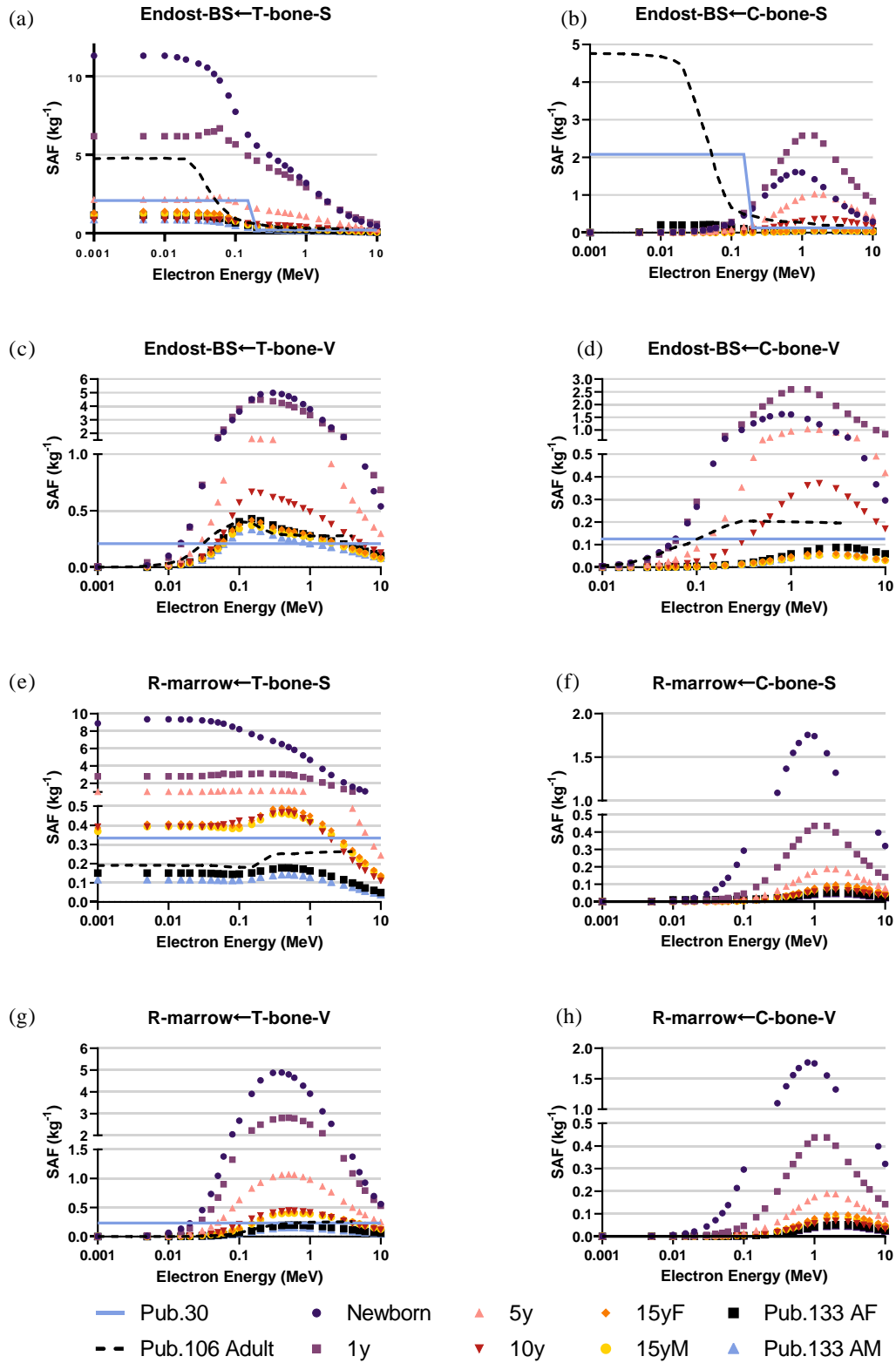
1024 (100) Since the microstructure of the skeleton cannot be modelled in the reference voxel
1025 phantoms, separate image-based voxel models of human skeletal microstructure have been used
1026 to compute absorbed fractions in the adult (Hough et al. 2011; O'Reilly et al. 2016) and paediatric
1027 individuals (Pafundi et al. 2010).

1028 (101) Intraskkeletal electron SAFs in this work are taken from those developed in Pafundi (2009)
1029 and are given as a function of reference age with no differentiation by sex. As described in Pafundi
1030 et al. (Pafundi et al. 2009; Pafundi et al. 2010), electron SAFs were computed following paired-
1031 image radiation transport simulation within CT-based images of whole bone and microCT images
1032 of spongiosa cores acquired in 5 skeletal sites within two female newborns at autopsy. The bone
1033 sites were the sternum, occipital bone, ribs, thoracic vertebrae, and lumbar vertebrae. SAF values
1034 at bone sites for which a 3D voxelised model was not available were estimated using weighting
1035 schemes originally proposed by Whitwell (1973). For the 15-year model, intraskkeletal electron
1036 SAFs were based upon paired-image radiation transport simulations within CT and microCT
1037 images of some 26 skeletal sites across both the axial and appendicular skeleton of an 18-year
1038 male cadaver. Methods applied to this model were identical to those described in both Hough et
1039 al. (2011) and O'Reilly et al. (2016) for the UF reference adult male and adult female, respectively.

1040 (102) As physical samples of trabecular spongiosa were not available to perform 3D electron
1041 transport in the skeletons of the 1-year, 5-year, and 10-year reference children, an alternative
1042 approach was taken. Macroscale electron transport was first performed within the skeletal sites of
1043 the reference phantoms at these three ages to compute sources in the cortical bone, trabecular
1044 spongiosa, and medullary cavities of the long bones. Next, microscale electron transport was
1045 performed for the 1-year and 10-year reference children using optical pathlength distributions
1046 originally reported in Beddoe et al. (1976) for a 1.7-year and 9-year child in simulated 3D
1047 geometries as described by Watchman et al. (2005). Pathlength distributions within the 5-year
1048 model were established as age-interpolated values between the 1.7-year and 9-year datasets.

1049 (103) Figure 4.5 plots the electron SAFs in this work along with those for the adult from
1050 *Publications 30, 106, and 133*. The SAF to the bone surface target is significantly smaller than
1051 values used in *Publications 30 and 133* due to the previously mentioned change in the target
1052 thickness from 10 μm to 50 μm . A significant difference in the definition of the cortical bone
1053 source is observed in Figure 4.5b. In the present work for electrons, the cortical bone surface was
1054 modelled as consisting of Haversian canals within the bone cortex and the endosteal surface of
1055 cortical bone of the long bone shafts. Since Haversian canals exist throughout the cortical bone
1056 volume, the electron SAFs for cortical bone surfaces are assumed to be identical to those of the
1057 cortical bone volume.

1058
1059

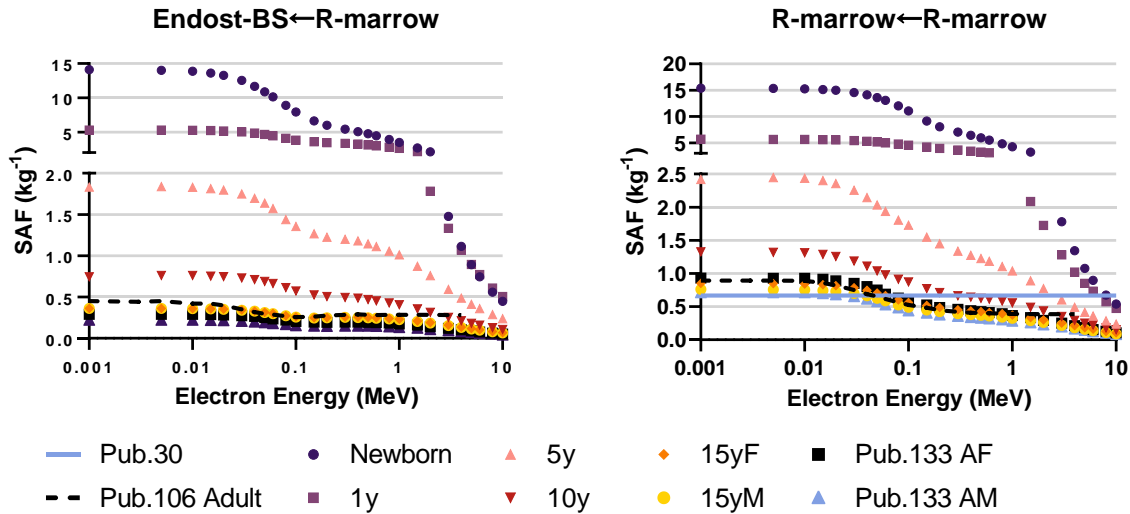


1060
1061
1062

Fig. 4.5 Intraskeletal electron SAFs for each reference individual. The plots also show adult SAF values from *Publications 30* and *106*.

1063
1064
1065
1066
1067

(104) The intraskeletal electron SAFs for emissions from the red marrow are shown in Figure 4.6. The red marrow self-irradiation geometry was treated as independent of energy in *Publication 30*. The current models now account for energy-dependent loss to surrounding yellow marrow and bone. The age-dependency accounts for the variation in marrow cellularity with age.



1068
1069
1070

Fig. 4.6. Intraskeletal electron SAFs for each reference individual for emission from the red marrow.

1071 4.4.3. Alphas

1072 (105) Intraskeletal alpha-particle SAFs for the adults were computed using both Monte Carlo
1073 and range-energy type calculations as described in *Publication 133*. Results using similar methods
1074 were not available for alpha particles in the paediatric skeleton. One approach for obtaining
1075 paediatric SAFs would be to scale the adult SAFs by the target mass. However, the significant
1076 changes in the skeletal structures and marrow cellularity with age make this problematic. Instead,
1077 an approach was adopted which uses electron SAFs for similarly ranged alpha particles. The
1078 method has the benefit of using electron SAF data which accounts for age-dependent changes in
1079 the skeleton. The weakness of the method is that the stopping power is not the same for similarly
1080 ranged alpha particles and electrons.

1081 (106) Figure 4.7 plots the energy of alpha particles and electrons versus their range in red
1082 marrow. Each set of data has been fit to obtain empirical power functions relating range and energy
1083 for each radiation type. Equations (4.7) and (4.8) give an empirical range-energy equation for each
1084 radiation in red marrow, where E is the energy in MeV of the given radiation type and R is the
1085 linear range in units of cm.

1086

$$E_{\text{alpha, RM}} = 210R^{0.6678} \quad (4.7)$$

$$E_{\text{electron, RM}} = 1.197R^{0.5757} \quad (4.8)$$

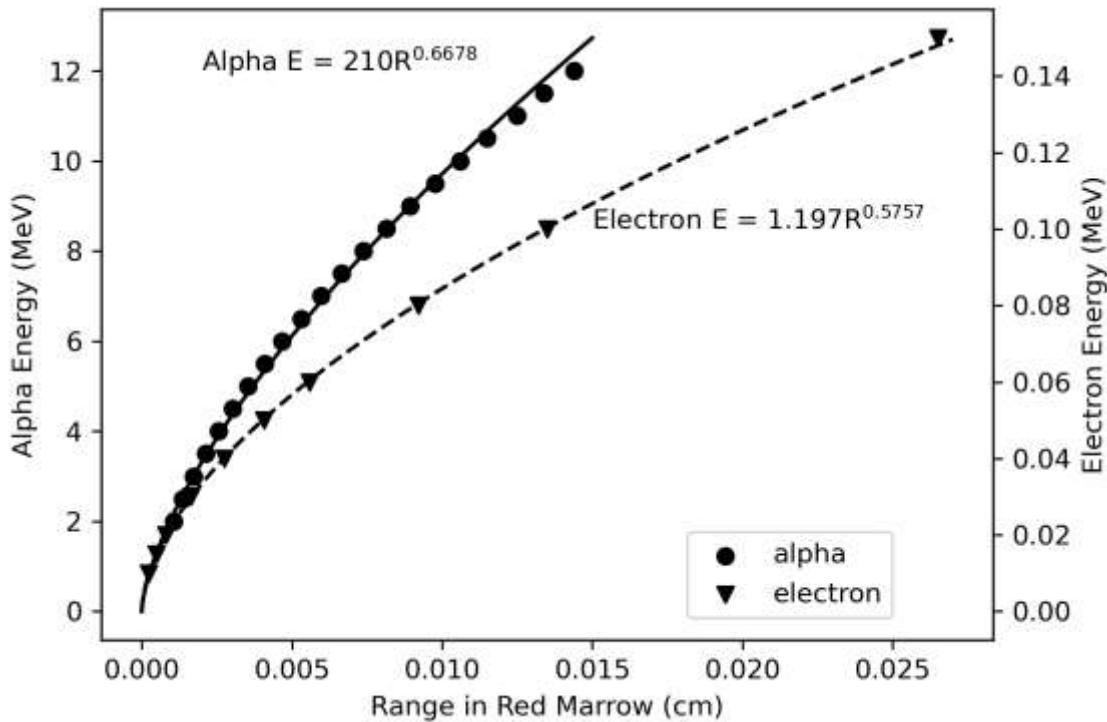
1087
1088
1089

(107) Combining Eqs. (4.7) and (4.8) and eliminating the range gives Eq. (4.9) which provides the energy of an electron with equivalent range in red marrow to that of an alpha particle of given

1090 energy. Equation (4.9) is used to obtain electron energies with equivalent ranges to each desired
 1091 alpha energy on the SAF grid. The SAF is then obtained by interpolating the skeletal electron
 1092 SAFs.

$$E_{\text{electron, RM}} = 1.197 \left(\frac{E_{\text{alpha, RM}}}{210} \right)^{0.862} \quad (4.9)$$

1093 (108) Equation (4.9) was used to obtain alpha SAFs for emissions from all marrow regions and
 1094 bone surfaces since the energy absorption is occurring on the soft tissue side of the bone-marrow
 1095 surface plane. An exception was made for the red marrow self-irradiation geometry. For this
 1096 geometry adult SAF values were scaled by target mass to the younger ages to preserve consistency
 1097 of shape of the SAF curve.



1098
 1099 Fig. 4.7 Energy versus range in red marrow for alpha particles and electrons.

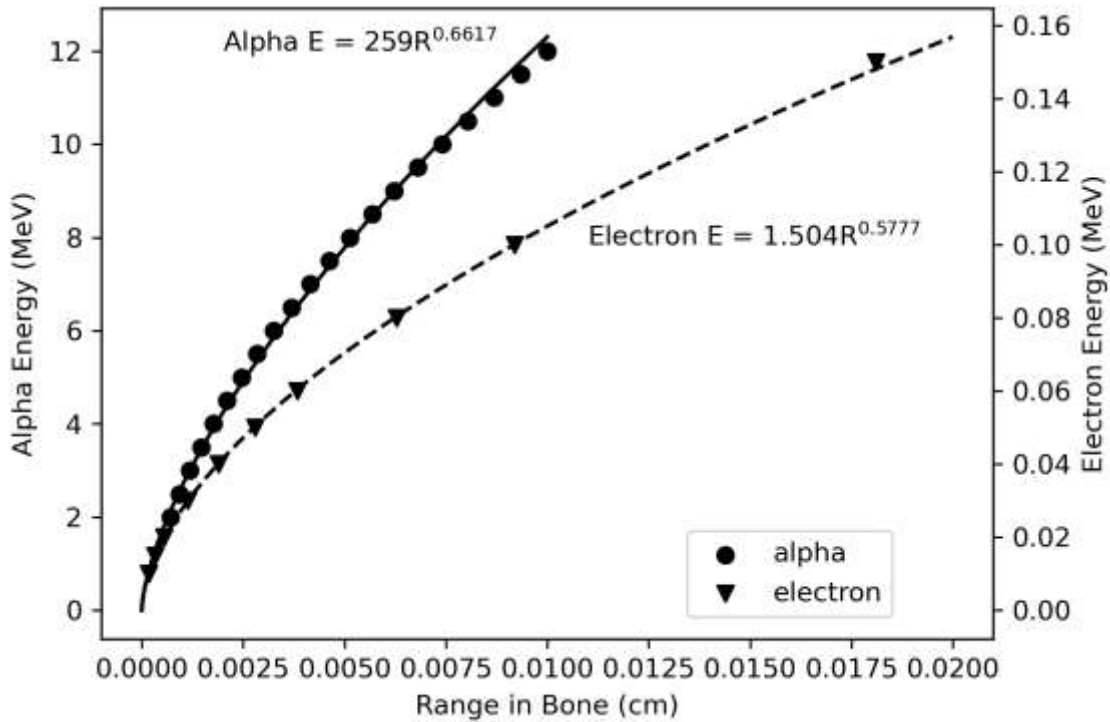
1101 (109) Figure 4.8 shows the ranges of alpha particles and electrons in bone. Equations (4.10) and
 1102 (4.11) show empirical relationships between energy and range. Combining these equations and
 1103 eliminating the range gives Eq. (4.12) which relates the alpha energy to the electron energy which
 1104 would yield the same range in bone. This equation was used to find interpolated SAFs for
 1105 emissions from the trabecular bone volume. Note that alpha particles emitted from the cortical
 1106 bone volume are considered to have absorbed fractions of zero at all alpha energies.

$$E_{\text{alpha, bone}} = 259R^{0.6617} \quad (4.10)$$

$$E_{\text{electron, bone}} = 1.504R^{0.5777} \quad (4.11)$$

$$E_{\text{electron, bone}} = 1.504 \left(\frac{E_{\text{alpha, bone}}}{259} \right)^{0.873} \quad (4.12)$$

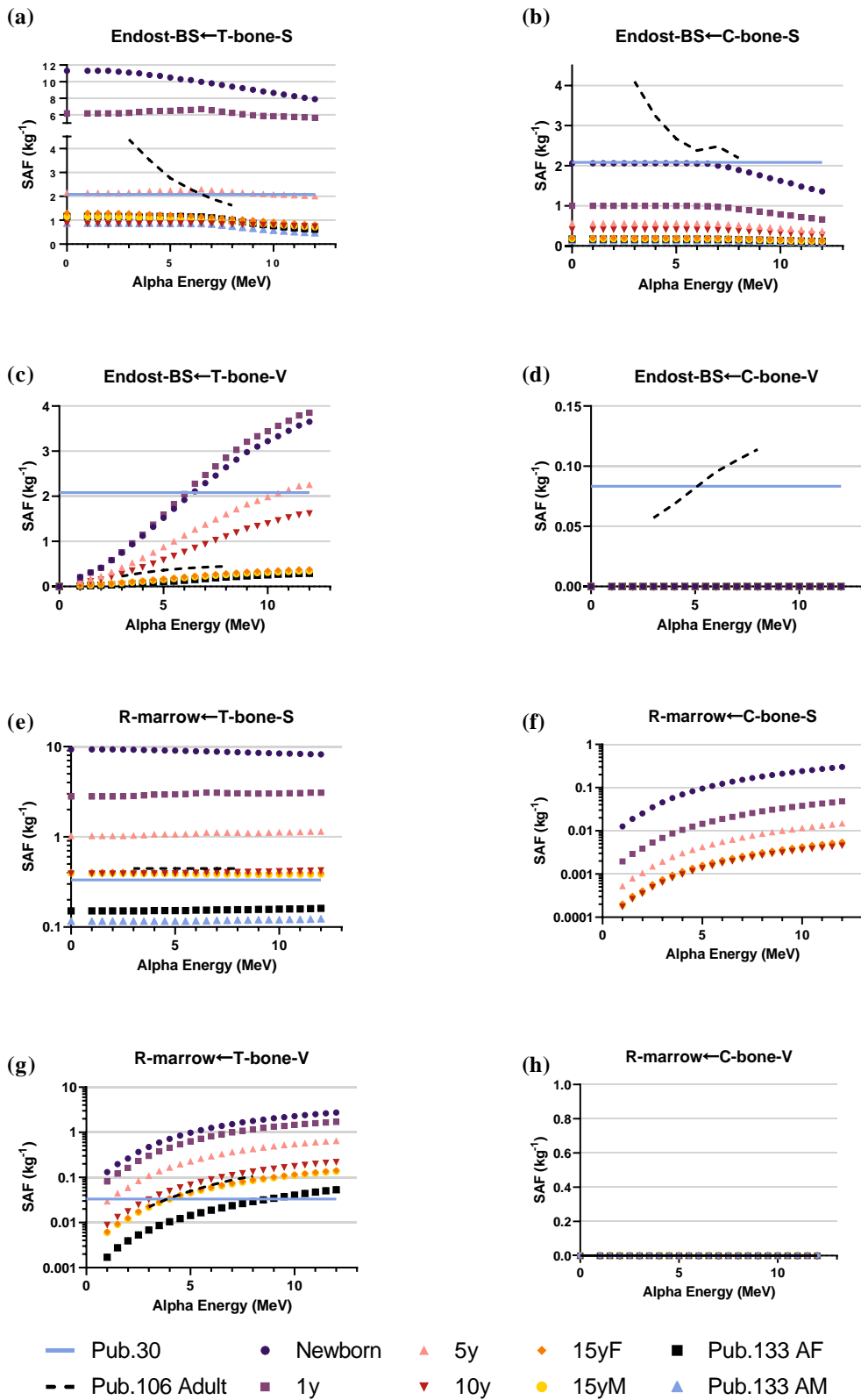
1108



1109
 1110
 1111
 1112
 1113
 1114
 1115
 1116
 1117
 1118
 1119

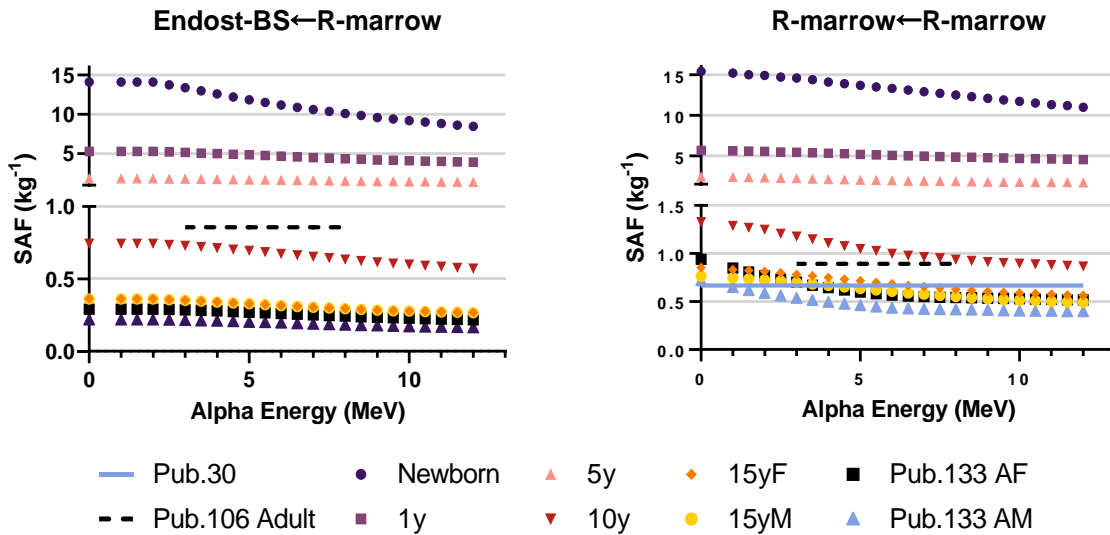
Fig. 4.8 Energy versus range in bone for alpha particles and electrons.

(110) The intraskeletal alpha-particle SAFs are shown in Fig. 4.9. As with electrons, significant differences are seen resulting from the change in the modelling definition to a 50 µm endosteum target. For alpha emissions in red marrow, energy loss to surrounding yellow marrow and bone is less significant but does still show an energy dependency. Fig. 4.10 displays values of the SAF for a red marrow source of alpha particles.



1120
1121
1122

Fig. 4.9 Intraskeletal alpha-particle SAFs from bone source regions. Note that y-axis scales are varied to improve visualization.



1123
 1124 Fig. 4.10. Skeletal SAFs for alpha-particles emitted from the red (active) marrow.
 1125

1126 **4.4.4. Photons and Neutrons**

1127 (111) SAFs to the skeletal targets for both intra-skeletal and extra-skeletal photon sources were
 1128 computed by coupling (1) Monte Carlo derived energy/bone-dependent volumetric photon
 1129 fluences scored within regions of trabecular spongiosa and long-bone medullary marrow cavities
 1130 and (2) energy/bone site-dependent fluence-to-dose response functions for red marrow and
 1131 endosteum. Adult skeletal dose-response functions (ICRP 2010, 2016a) were originally computed
 1132 in Wayson (2012) using the electron SAFs and skeletal tissue masses given in Pafundi (2009) via
 1133 the methods of Johnson et al. (2011) established for adult photon skeletal dosimetry and used as
 1134 described here in Eqs. (4.1) and (4.2). Age-dependent photon skeletal dose-response functions
 1135 were used in the computation of photon SAFs.

1136 (112) In *Publication 133*, SAFs to skeletal targets (red marrow and endosteum) for neutrons
 1137 from spontaneous fission sources were computed by coupling Monte Carlo derived neutron
 1138 fluences to neutron fluence-to-dose response functions (Bahadori et al. 2011). Similarly, neutron-
 1139 induced photon fluences, from (n, γ) reactions, were coupled to adult photon fluence-to-dose
 1140 response functions (Eckerman et al. 2008; Johnson 2011). For the reference paediatric individuals,
 1141 the age-dependent photon fluence-to-dose response functions were coupled to the neutron-induced
 1142 photon fluences from (n, γ) reactions. Fluence-to-dose response functions for neutron fluences in
 1143 paediatric individuals were not available, so those derived for the adult male were used instead.
 1144

1145
1146

5. SPECIFIC ABSORBED FRACTION CALCULATION AND TABULATION

1147

1148 (114) As described by Equation (2.14) the SAF is determined by taking the fraction of emitted
1149 energy within a source region which is absorbed in a target region and dividing by the mass of the
1150 target region. Section 4 described the computational methods and models used to arrive at the
1151 absorbed fraction for each source-target combination. Division by the target mass is then
1152 performed to provide a SAF. This section describes what adjustments, if any, are made to SAFs
1153 computed in models. It also describes methods for quality assurance in this large data set.

1154 5.1. Scaling SAFs to reference mass

1155 (115) While the computational models detailed in Section 4 were designed based on the
1156 definitions of the reference individuals of Section 3, the target mass used to compute a SAF in a
1157 given model is not always consistent with the reference target mass. In such cases, adjustment of
1158 the model-derived SAFs needs to be considered to arrive at the reference SAFs.

1159 (116) The need to consider scaling SAFs from a model or phantom to conform to another
1160 individual, whether it be a reference individual, a specific worker, a member of the public, or a
1161 medical patient is not new or unique to this effort. W.S. Snyder (1970) wrote about this need in
1162 what he described as a “preliminary” discussion which he hoped would spur further study. Snyder
1163 proposed a scaling for photon absorbed fractions in self-irradiation geometries which was
1164 proportional to the cube root of the mass of the source (and target) region. Snyder found that the
1165 proportionality worked well over the region where Compton scattering predominates. Snyder
1166 wrote:

1167
1168 “Clearly, this rule fails badly for photons of energy below 50 keV, and in these cases the
1169 AF [absorbed fraction] is greater than 0.5. Perhaps this reveals at once the limitations of
1170 this principle – namely, the organ must be small in relation to the mean free path of the
1171 photons that buildup is not an important contribution to the dose or to AF, and thus the
1172 principle does not hold for low energies. Clearly, for low photon energies such that the
1173 AF is approximately 1, the AF cannot continue to increase with the cube root of the mass
1174 as the mass of the organ is increased. Thus, the principle should be applied only for the
1175 energy region where Compton scattering predominates and then only when the AF is well
1176 below 1, say, ≤ 0.5 . But for many body organs and for a range of photon energies from,
1177 say, 0.2 to 2 MeV, the principle seems to hold fairly well...”

1178
1179 “It should be understood that no claim to a high degree of accuracy is made for these
1180 methods; indeed, quite the reverse. It is evident that only a rough approximation to the
1181 dose is given.”

1182
1183 (117) In MIRD Pamphlet 11 (Snyder et al. 1975), the MIRD Committee presented the
1184 proportionality above in terms of the SAF or absorbed dose as being equivalently proportional to
1185 the inverse of the mass to the 2/3 power. Again, the proportionality was qualified as being useful
1186 for photons “...with energies above 100 keV.”

1187
 1188 “Since dose from electrons scales with the inverse first power of the mass, if one assumes
 1189 complete absorption of energy, scaling is no longer simple; the photon dose changes with
 1190 one power of the mass and the electron dose changes with another. In fact, there seems to
 1191 be no simple scaling procedure which is approximately correct for all energies of particles
 1192 and masses of organs.”
 1193

1194 (118) Adams (1981) described using linear mass scaling for photon energies less than 30 keV
 1195 and the inverse 2/3 power scaling for energies above 30 keV. Petoussi-Henss et al. (2007) found
 1196 that photon self-dose SAFs vary with the inverse 2/3 power of mass for energies above 100 keV
 1197 “...and for organs that are not extended.” Wayson and Bolch (2018) performed Monte Carlo
 1198 radiation transport in spheres of varying sizes for photons and electrons. For photon self-dose they
 1199 found mass proportionality which varies from the inverse first power (at around 10 keV) to the
 1200 inverse 2/3 power (100 keV) and smaller when photon energy exceeds 1 MeV. For electrons, the
 1201 same study found the SAF was proportional to the inverse of the mass for all energies up to around
 1202 1 MeV.

1203 **5.1.1. Self-irradiation geometries**

1204 (119) Self-irradiation geometries are defined here as any in which the low energy SAF is non-
 1205 zero. These include source and target region being identical, but also include overlapping source
 1206 and target regions.

1207 (120) The low energy self-irradiation SAF is often the most important SAF in internal dose
 1208 coefficient calculations. A non-energy-dependent 2/3 power scaling approach would perturb the
 1209 low energy value. While an energy-dependent scaling such as described by Wayson and Bolch
 1210 may improve photon SAFs above 100 keV, in this work the simpler linear mass scaling described
 1211 in Eq. (5.1) was used for alphas, electrons, and photons.
 1212

$$\Phi_{\text{reference}}(r_T \leftarrow r_S, E) = \frac{m_{T,\text{phantom}}}{m_{T,\text{reference}}} \Phi_{\text{phantom}}(r_T \leftarrow r_S, E) \quad (5.1)$$

1213 where $m_{T,\text{phantom}}$ is the mass of the target region in the phantom or model used for the radiation
 1214 transport calculations and $m_{T,\text{reference}}$ is the mass of the target regions provided in Tables 3.10
 1215 through 3.15. This approach essentially treats the self-irradiation absorbed fraction in the phantom
 1216 as equivalent to the absorbed fraction in the reference individual.
 1217

1218 **5.1.2. Crossfire irradiation geometries**

1219 (121) Crossfire geometries are defined here as any in which the low energy SAF is zero. MIRD
 1220 Pamphlet 11 (Snyder et al. 1975), Petoussi-Henss et al. (2007), and Wayson and Bolch (2018) all
 1221 provide evidence that scaling is not required for these geometries. Therefore, crossfire geometry
 1222 SAFs computed in the phantoms and models are adopted for the reference individuals.

1223 **5.2. Low energy, limiting SAF values**

1224 (122) As the kinetic energy of any radiation approaches zero, the SAF approaches a value which
 1225 can be theoretically computed. The equations for the limiting values were provided in section 7 of
 1226 *Publication 133* (ICRP 2016a) and are summarised below. As in *Publication 133*, the SAFs
 1227 include tabulated SAFs for zero energy emissions of alphas, electrons, and photons. In addition to
 1228 their usefulness in low energy SAF interpolation, these theoretical, limiting SAF values were used
 1229 to confirm the correctness of the SAFs computed in various models.

1230 **5.2.1. Whole-body geometries**

1231 (123) If the source and target regions are non-overlapping with any distance between them, the
 1232 low energy absorbed fraction, and therefore the SAF approaches zero. If the definition of the
 1233 source and target consist of the same volume, the low energy absorbed fraction approaches unity
 1234 and the SAF is the inverse of the target mass as shown in Eq. (5.2).
 1235

$$\lim_{E \rightarrow 0} \Phi(r_T \leftarrow r_S, E) = \begin{cases} \frac{1}{m_T}, & \text{if } r_S = r_T \\ 0, & \text{if } r_S \neq r_T \end{cases} \quad (5.2)$$

1236

1237 **5.2.2. Alimentary tract geometries**

1238 (124) As described in section 4.2, the walls of the alimentary tract contain several source and
 1239 target regions which partially overlap. The low energy absorbed fraction in such regions is given
 1240 by the fraction of the source region's volume which is designated as a target region. Since the mass
 1241 density is the same throughout the regions, the volume ratio is equivalent to the mass ratio. If the
 1242 target region is completely within the source region, as is the case for the alimentary stem cell
 1243 targets for wall and mucosa source regions, the mass of the target cancels out in the SAF as shown
 1244 in Eq. (5.3). Note that the mass of the wall (or mucosa) in the denominator of Eq. (5.3) should
 1245 include the mass of blood in that region.

$$\lim_{E \rightarrow 0} \Phi(\text{HATM}_{\text{stem}} \leftarrow \text{HATM}_{\text{wall}}, E) = \frac{\frac{V_{\text{stem}}}{V_{\text{wall}}}}{\frac{m_{\text{stem}}}{m_{\text{stem}}}} = \frac{\frac{m_{\text{stem}}}{m_{\text{wall}}}}{m_{\text{stem}}} = \frac{1}{m_{\text{wall}}} \quad (5.3)$$

1246

1247 (125) All remaining source regions in the alimentary tract do not overlap with the target and
 1248 therefore give a low energy SAF of zero. These source regions include: the slow and fast clearance
 1249 regions in the oesophagus, the alimentary tract contents, and the villi in the small intestines.

1250 **5.2.3. Respiratory tract geometries**

1251 (126) In the respiratory tract the target regions are basal cells in the extrathoracic tissues (ET1
 1252 and ET2) and the bronchi of the lungs, secretory and basal cells in the bronchi, and secretory cells
 1253 in the bronchioles, and the alveolar interstitium. Source regions which do not overlap with these
 1254 targets and therefore give a low energy SAF of zero are the mucosal surfaces of the extrathoracic
 1255 regions (ET1-sur, ET2-sur), the sequestered regions of the posterior nasal passage, larynx,

1256 pharynx, and mouth (ET2-seq), the bronchi and bronchioles (bronchi-q and brchiole-q), surface
 1257 transport in the bronchi and bronchioles (bronchi, brchiole), and the airways (RT-air).

1258 (127) All other source regions (walls and bound regions) in the respiratory tract overlap with
 1259 the target regions, and therefore the same relationship described in Eq. (5.3) applies to these
 1260 geometries. The low energy SAF will approach the inverse of the mass of the source region
 1261 inclusive of any blood in the source region.

1262 5.2.4. Skeletal geometries

1263 (128) Within the skeleton, the two target regions are the red (active) marrow and the bone
 1264 endosteum. The latter is defined as a 50- μ m thick region of soft tissue adjacent to the interior bone
 1265 surface (Bolch et al. 2007). Source regions within the skeleton include bone marrow, cortical and
 1266 trabecular bone volumes and surfaces. The bone surface sources are mathematically defined as a
 1267 two-dimensional, non-volumetric interface between the bone and marrow cavity.

1268 (129) The marrow source regions are divided as either red and yellow marrow or as trabecular
 1269 and cortical marrow. The trabecular and cortical marrow consists of a mixture of red and yellow
 1270 marrow in varying proportion with age depending on the skeletal site-specific marrow cellularity.
 1271 The trabecular and cortical marrow source regions are called for in the systemic biokinetic models
 1272 of many of the actinides and lanthanides (ICRP 2017, 2019). In this work, the SAFs were computed
 1273 using models with red and yellow marrow regions. Cortical and trabecular SAFs were computed
 1274 later using skeletal site specific SAFs of the red and yellow marrow regions and information on
 1275 marrow cellularity. The need for two different source region treatments for the marrow space
 1276 results from systemic biokinetic modelling. When the cortical/trabecular treatment is not
 1277 specifically invoked by a systemic biokinetic model, the red/yellow treatment should be used as
 1278 the default marrow treatment.

1279 (130) For source material in the marrow space irradiating the bone endosteum target, the
 1280 regions overlap and similarly to Eq. (5.3), the low energy absorbed fraction can be found by the
 1281 volume ratio. The resulting SAF is shown in Eq. (5.4), where m_{Marrow} is the mass of the entire
 1282 marrow space.

$$1283 \lim_{E \rightarrow 0} \Phi(\text{Endost-BS} \leftarrow \text{Marrow}, E) = \frac{\frac{V_{\text{Endost-BS}}}{V_{\text{Marrow}}}}{\frac{m_{\text{Endost-BS}}}{m_{\text{Marrow}}}} = \frac{1}{m_{\text{Marrow}}} \quad (5.4)$$

1284 (131) For source material on the trabecular bone surface irradiating the bone surface, the low
 1285 energy absorbed fraction is one-half. The low energy SAF is given in Eq. (5.5).

$$1287 \lim_{E \rightarrow 0} \Phi(\text{Endost-BS} \leftarrow \text{T-bone-S}, E) = \frac{1/2}{\frac{m_{\text{Endost-BS}}}{2m_{\text{Endost-BS}}}} = \frac{1}{2m_{\text{Endost-BS}}} \quad (5.5)$$

1288 (132) The low energy SAF for activity on the trabecular bone surface irradiating the red marrow
 1289 is more complex. For a given skeletal site, i , with known red marrow cellularity, c_i (fraction of
 1290 marrow which is active), Eq. (5.6) can be used to find a limiting SAF. Since the cellularity varies
 1291 across different skeletal sites, the limiting value for each site must be summed using source
 1292 weighting to obtain a skeletal averaged low energy SAF.

1294

$$\lim_{E \rightarrow 0} \Phi_i(\text{R-marrow} \leftarrow \text{T-bone-S}, E) = \frac{c_i/2}{m_{\text{Endost-BS},i}} = \frac{c_i}{2m_{\text{Endost-BS},i}} \quad (5.6)$$

$$\lim_{E \rightarrow 0} \Phi_{\text{skeleton}}(\text{R-marrow} \leftarrow \text{T-bone-S}, E) = \sum_i \frac{SA_{\text{BS},i}}{SA_{\text{BS},\text{skeleton}}} \frac{c_i}{2m_{\text{Endost-BS},i}}$$

1295

1296 5.2.5. Blood source geometries

1297 (133) The blood source in the SAF represents blood distributed throughout the entire body. The
 1298 blood SAFs give the fractional energy absorption to targets resulting from nuclear transformations
 1299 taking place in large arteries and veins as well as those taking place in blood which has perfused
 1300 tissue. As given in *Publication 133*, the low energy limiting SAF for source material in the blood
 1301 irradiating a given target region is:

$$\lim_{E \rightarrow 0} \Phi(r_T \leftarrow \text{Blood}, E) = \frac{f_{r_T}}{m_T} \quad (5.2)$$

1302

1303 where f_{r_T} is the fraction of the body's blood in region r_T as described in Table 3.3.

1304 5.2.6. Low-energy extrapolation

1305 (134) As was performed in *Publication 133* (ICRP 2016a), when the low energy limiting SAF
 1306 is non-zero, log-log interpolation was performed for SAF values at energies smaller than those
 1307 reliably provided by the radiation transport calculations. For the sake of the log-log interpolation,
 1308 zero energy is treated as having a value of 10^{-3} keV and, if the low energy limiting SAF is zero it
 1309 is treated as having a value of 10^{-12} kg⁻¹.

1310 (135) Schwarz et al (2021a) describe how interpolations were performed for electrons with
 1311 kinetic energies less than 10 keV. For photons, the energy used for interpolation would vary
 1312 between 10 and 30 keV depending on the source-target geometry and the energy-dependent shape
 1313 of the SAF curve (Schwarz et al. 2021b).

1314 5.3. Quality checks on SAF values

1315 (136) The set of paediatric SAFs for ICRP reference individuals represents a large data set.
 1316 Quality checks were performed on this data at multiple stages. Use of version control repositories
 1317 allowed for tracking of edits and changes to the data set during development. The theoretical low
 1318 energy limiting SAF values described earlier in this section were computed and compared to data
 1319 sets. Visualizations of data sets were also reviewed for expected trends and relationships. For
 1320 example, since most target masses increase with increasing age, SAFs generally decrease with
 1321 increasing age. Additionally, some geometries within a system create logical relationships between
 1322 source/target combinations. The following examples provide a look at some of the quality checks.

1323 (137) Another important tool for checking the quality of SAFs is the calculation and evaluation
 1324 of the associated organ and tissue dose coefficients. Preliminary SAFs were distributed to multiple
 1325 users with codes used for computing internal dose coefficients. The resulting equivalent and
 1326 effective dose coefficients were studied to look for anomalous results. Dose coefficients can be
 1327 compared to past dose coefficients with changes needing to be explained either by something in

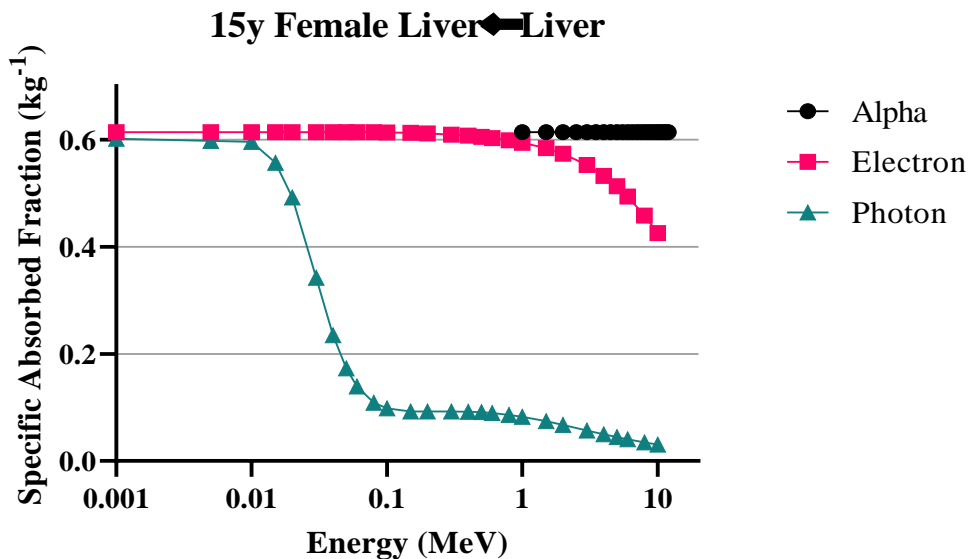
1328 the biokinetics or in the energy absorption term. One particularly valuable case is to look at
 1329 equivalent dose coefficients resulting from the ingestion of tritiated water. Water distributes fairly
 1330 uniformly throughout soft tissue. The low energy, pure beta emission associated with tritium
 1331 means uniform equivalent dose coefficients should result across all soft tissue targets.

1332 **5.3.1. Limiting value checks across radiation types**

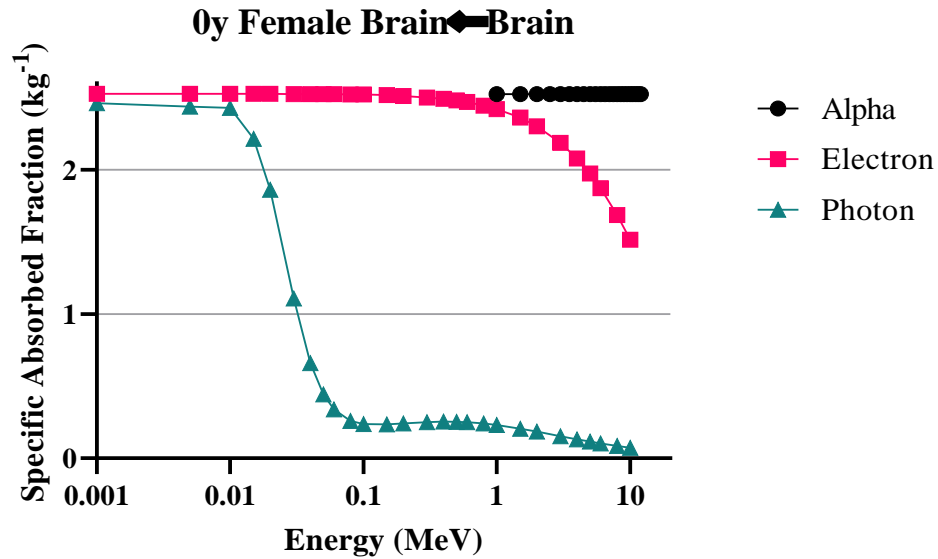
1333 (138) The theoretical low energy limiting SAF values provided in section 5.1 are a useful tool
 1334 for checking the quality of SAF data. These values were computed based on the reference masses
 1335 in section 3 and compared to SAF data. Since these values are independent of radiation type, plots
 1336 were created for a given geometry with alpha, electron, and photon SAFs on the same plot and
 1337 reviewed for SAF convergence to the limiting value at low energy.

1338 (139) Figures 5.1 through 5.3 provide three examples of such plots. Self-irradiation of the 15y
 1339 female liver is shown in Fig. 5.1. Using Eq. (5.2) with the target mass for the 15y female liver of
 1340 1.628 kg from Table 3.14 yields a theoretical low-energy SAF of 0.614 kg^{-1} . This value matches
 1341 the data in Fig. 5.1. Note that theoretical low energy limiting SAFs are generally checked
 1342 numerically within the SAF files. Calculated similarly, the theoretical low energy SAF for self-
 1343 irradiation of the newborn female brain (Fig. 5.2) is 2.527 kg^{-1} .

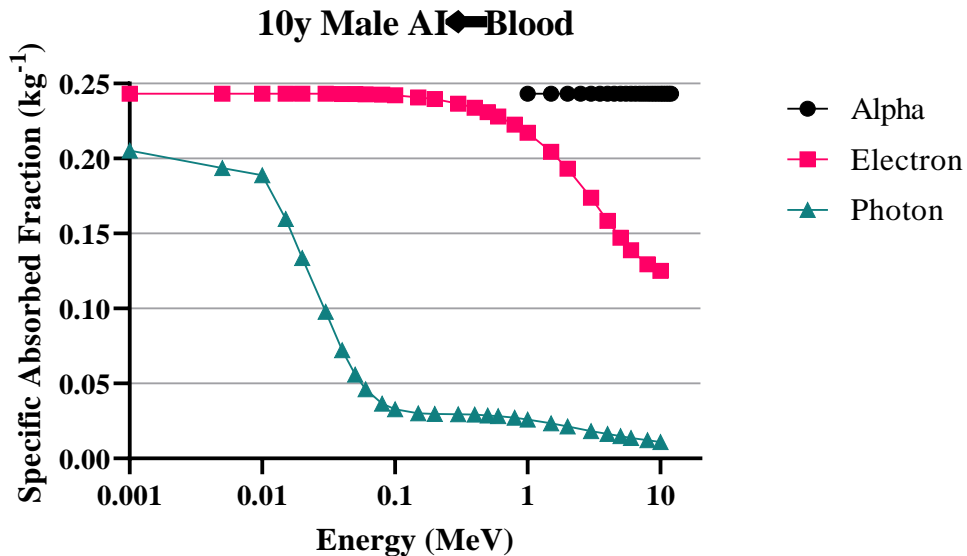
1344 (140) Equation (5.7) was used to compute the theoretical low energy limiting SAF for the blood
 1345 irradiating the alveolar target in a 10y male. As described in section 3.2, the alveolar interstitium
 1346 (AI) target receives all of the pulmonary gas exchange blood and a portion of the pulmonary
 1347 nutrient blood. Performing the mass splitting of the nutrient blood results in 12.2% of the body's
 1348 blood being assigned to the AI target. Using the AI target mass of 500 g (Table 3.13) results in a
 1349 low energy SAF of 0.243 kg^{-1} . Figure 5.3 contains this data, although because the x-axis is log-
 1350 scale the low energy limiting SAF has not yet reached convergence at 1 keV. Instead, it does so
 1351 at the zero energy point in the data files.
 1352



1353
 1354 Fig. 5.1. Liver self-irradiation SAFs in the 15-year female for alphas, electrons, and photons.
 1355



1356 Fig. 5.2. Brain self-irradiation SAFs in the newborn female for alphas, electrons, and photons.
 1357
 1358



1359 Fig. 5.3. SAFs for emissions from the blood irradiating the alveolar interstitium in the 10-year
 1360 male for alphas, electrons, and photons.
 1361
 1362

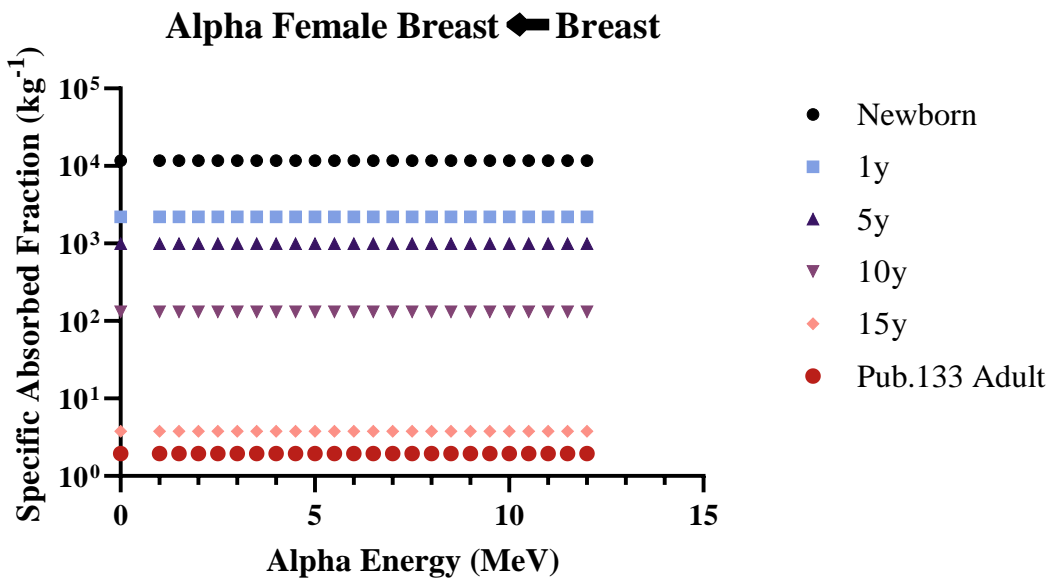
1363 **5.3.2. Age-dependency**

1364 (141) Age dependency of SAFs is inversely proportional to the mass of the target when the
 1365 absorbed fraction is at or near unity. This is particularly true for alpha particles and low energy
 1366 electrons. Figure 5.4 shows self-irradiation of the female breast for alpha particles and the expected
 1367 relationship between ages is observed. Figure 5.5 shows a partial, self-irradiation as the right colon
 1368 stem cell target comprises a portion of the right colon wall. At sufficient electron energies, the

1369 SAF drops from its low energy value and the difference between ages decreases. Figure 5.6 is
 1370 photon self-irradiation of the skin and displays the expected age dependency.

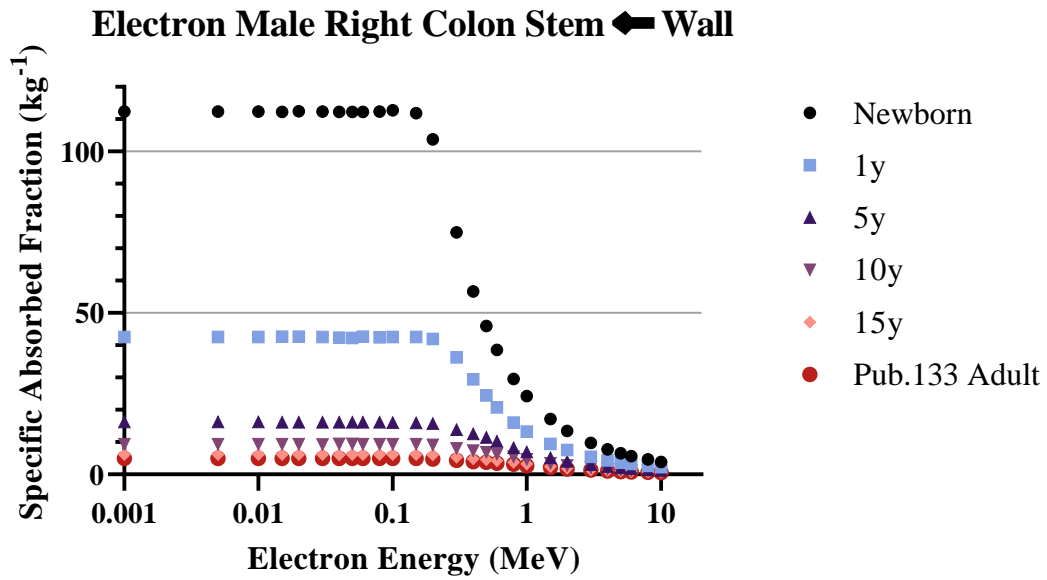
1371 (142) Figure 5.7 is an example of a result where a small inconsistency can be observed between
 1372 the data for the adult and the paediatric individuals. The adrenals are located in close proximity to
 1373 the kidneys. Around 200 keV the electron SAF for the adult begins to increase away from zero
 1374 while the SAF for younger individuals remains near zero. In the voxel phantom for the adult, the
 1375 adrenals are located closer to the kidneys than in the paediatric voxel phantoms, in fact some
 1376 adrenal voxels are located adjacent to kidney voxels in the adult reference voxel phantoms. The
 1377 SAF for the adult also peaks at a lower energy than it does for every other phantom except for the
 1378 newborn which is consistent with the adrenals being slightly further away in the paediatric
 1379 phantoms than they are in the adult phantom. This does not necessarily speak to a problem with
 1380 any of the plotted SAFs, particularly when one considers the small differences in the SAFs and the
 1381 consistency of the shape amongst the individuals. It simply reflects a modelling difference which
 1382 may reflect anatomical reality or biological variability.

1383 (143) Figure 5.8 shows SAFs for photons emitted from the cortical bone volume irradiating the
 1384 thyroid. Consistency of shape is again observed, and the expected age dependency is observed.
 1385



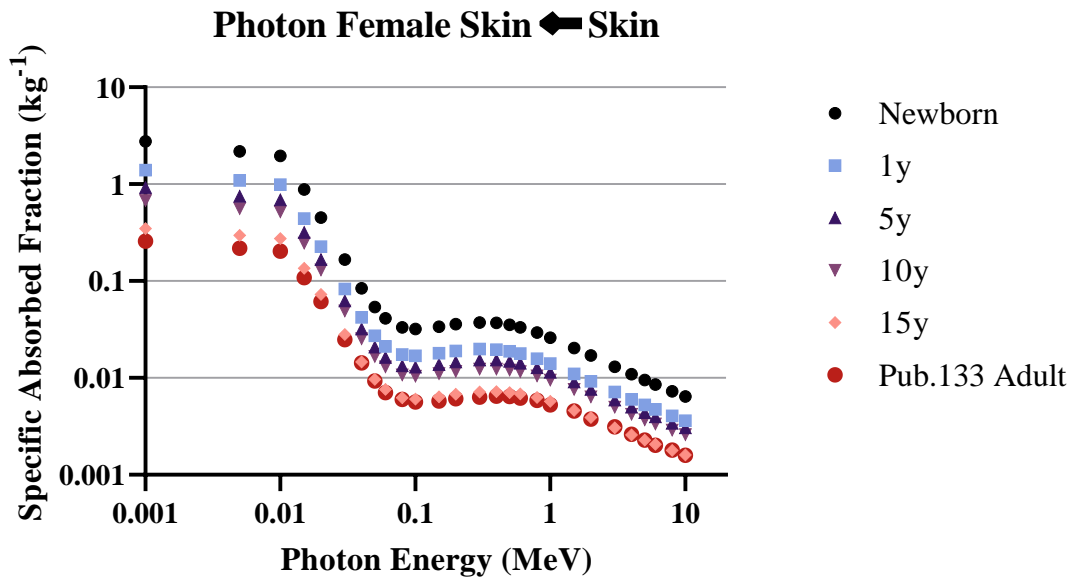
1386
 1387 Fig. 5.4. Breast self-irradiation SAFs for alpha particles in each reference female.
 1388

1389
 1390



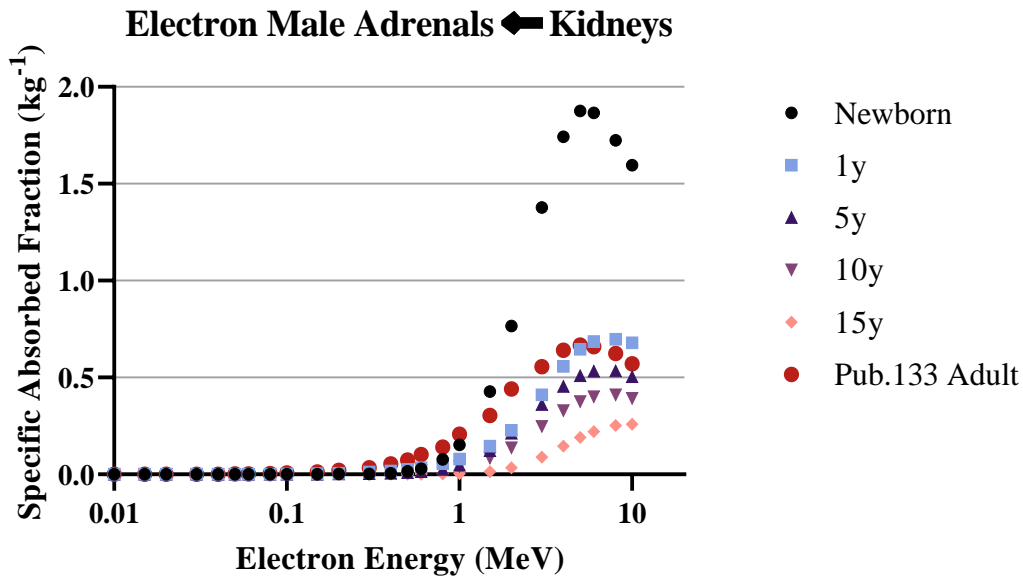
1391
1392
1393
1394

Fig. 5.5. Electron self-irradiation SAFs for the right colon stem cell target irradiated from the right colon wall in each reference male.

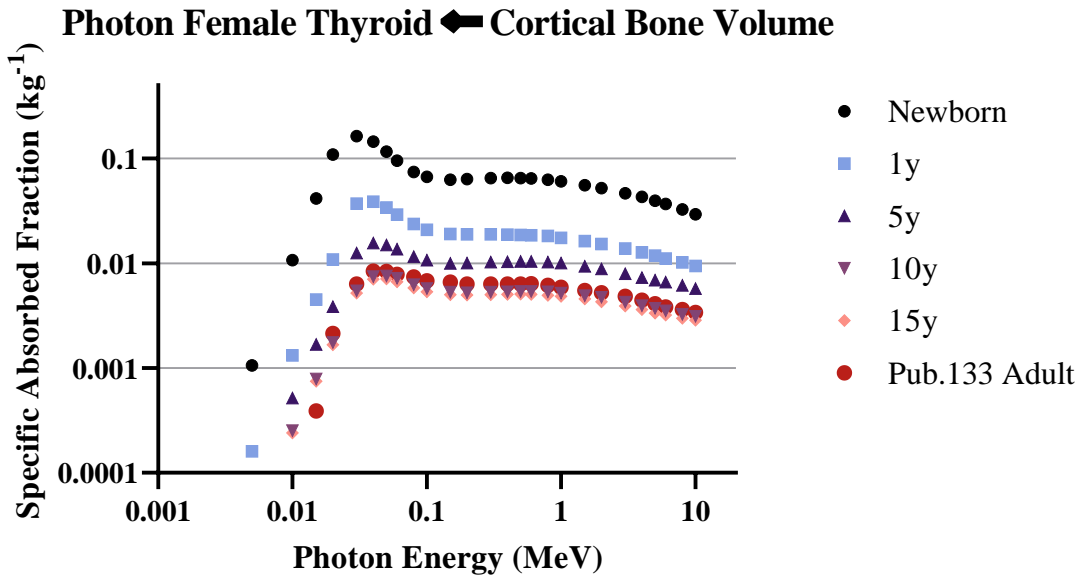


1395
1396
1397
1398
1399

Fig. 5.6. Skin self-irradiation SAFs for photons in each reference female.



1400
 1401 Fig. 5.7. SAFs for electrons emitted from the kidneys irradiating the adrenals in each reference
 1402 male.
 1403



1404
 1405 Fig. 5.8. SAFs for photons emitted from the cortical bone volume irradiating the thyroid in each
 1406 reference female.
 1407

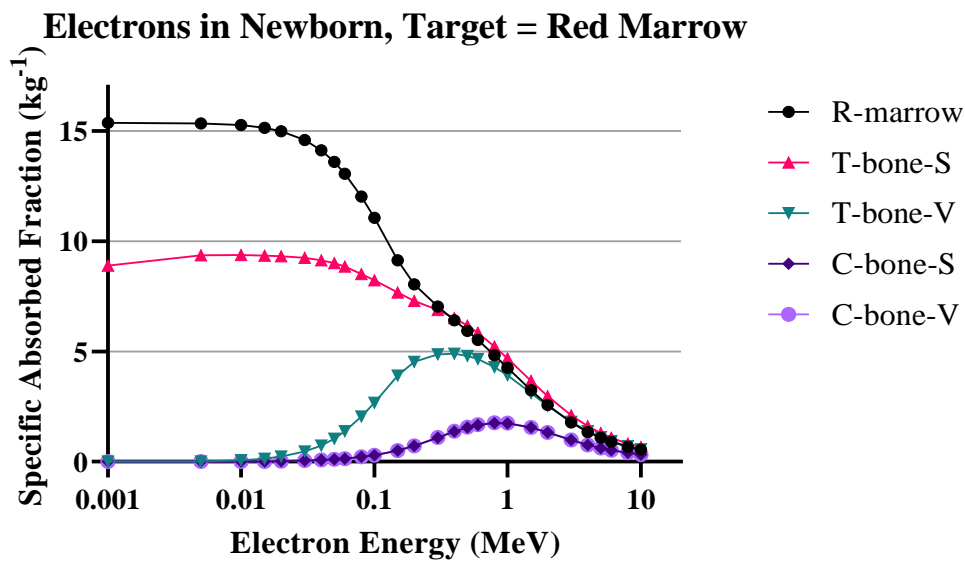
1408 **5.3.3. Geometries with relationships**

1409 (144) Figure 5.9 shows SAFs to the newborn red marrow target for electrons emitted from a
 1410 variety of skeletal source regions. At the lowest energy SAFs approach the limiting self-irradiation
 1411 values for sources in the red marrow and on the trabecular bone surface. As electron energy

1412 increases the trabecular bone volume source is the first of the bone sources to depart from zero due
 1413 to the smaller size of trabecular bone and being surrounded by marrow. Cortical bone is generally
 1414 thicker and has marrow located on only the interior side of the source region. Finally, as electron
 1415 energy continues to increase the expected convergence of the SAFs is observed. At high energies
 1416 (long ranges) the medium of origin of the electron becomes irrelevant.

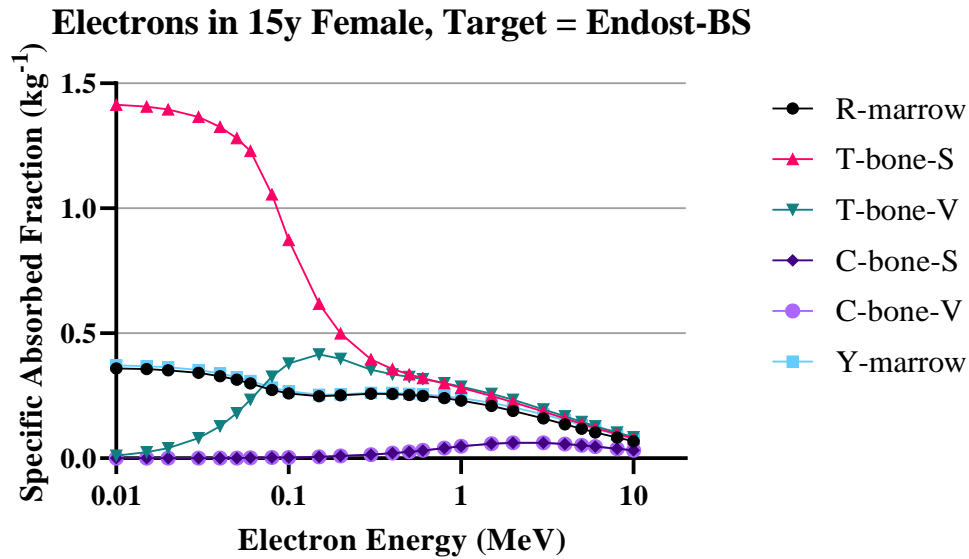
1417 (145) Figure 5.10 displays SAFs in the 15y female bone endosteum target for electrons emitted
 1418 from varying skeletal source regions. Since the trabecular bone surface is adjacent to the bone
 1419 endosteum emissions from that surface produce the highest SAF at low energies. The marrow
 1420 source regions give non-zero low energy SAFs since the bone endosteum target consists of marrow
 1421 space adjacent to the surface. Similar trends as those described in the previous paragraph are
 1422 observed for intermediate and high energy electrons.

1423
 1424



1425
 1426
 1427
 1428
 1429
 1430

Fig. 5.9. Newborn SAFs for electrons emitted from various skeletal source regions irradiating the red marrow.

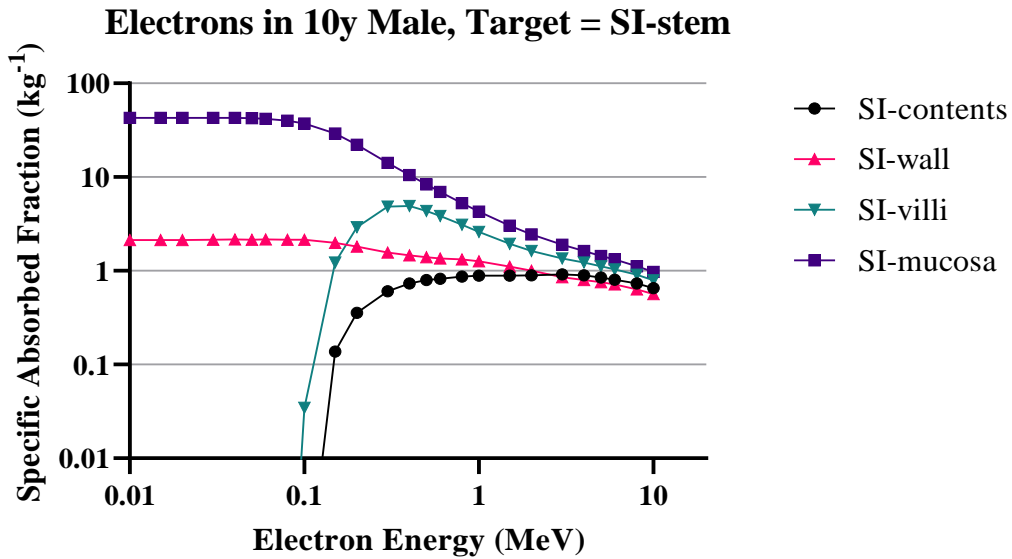


1431
 1432 Fig. 5.10. 15-year female SAFs for electrons emitted from various skeletal source regions
 1433 irradiating the bone endosteum.
 1434

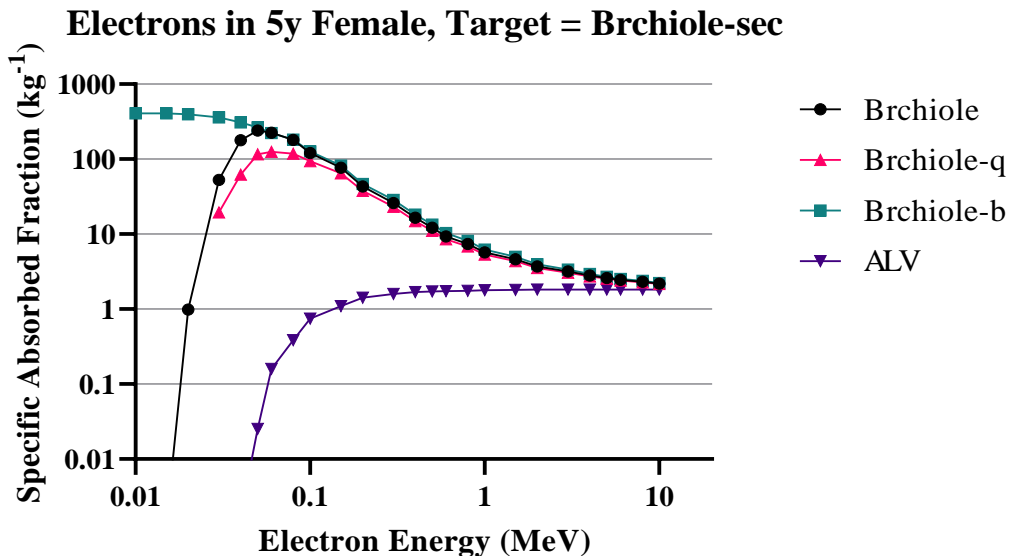
1435 (146) Figure 5.11 is a plot of SAFs for electrons emitted from various small intestine source
 1436 regions irradiating the 10y male small intestine stem cell target. The stem cell target layer is
 1437 contained within the mucosa and the mucosa is enveloped by the wall. The expected non-zero SAF
 1438 is observed for both geometries with the mucosa source producing a larger SAF owing to its
 1439 smaller size compared to the wall. Since the villi are closer in proximity to the stem cell target than
 1440 the contents, the SAF increases away from zero at a lower electron energy for emissions from the
 1441 villi. Finally, as with the skeletal geometries at high energies the SAFs converge as the location of
 1442 the emission becomes less important.

1443 (147) Figure 5.12 is a plot of SAFs for electrons emitted from lung source regions irradiating
 1444 the bronchiole secretory cell target. Source material bound in the bronchiolar epithelium (Brchiole-
 1445 b) overlaps with the target region and therefore has a non-zero low energy SAF. The surface
 1446 transport region (Brchiole) is the next closest source region to the target followed closely by
 1447 material sequestered in the lamina propria (Brchiole-q) so the SAF for electrons emitted from those
 1448 two regions rise away from zero at similar energies. The alveolar source region is further away,
 1449 but in still close proximity to the bronchiole target tissue. Similar to the other geometries discussed
 1450 in this section, at high energies the SAFs converge.

1451
 1452



1453
 1454 Fig. 5.11. 10-year male SAFs for electrons emitted from various small intestine source regions
 1455 irradiating the small intestine stem cell target.
 1456
 1457

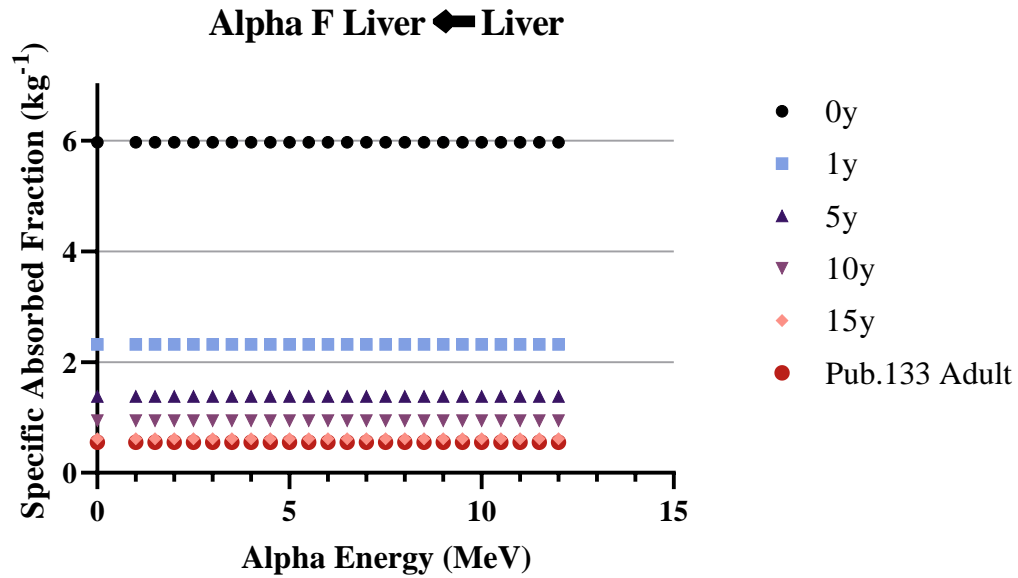


1458
 1459 Fig. 5.12. 5-year female SAFs for electrons emitted from various lung source regions irradiating
 1460 the bronchiolar secretory cell target.
 1461

1462 **5.4. Plots of example SAFs**

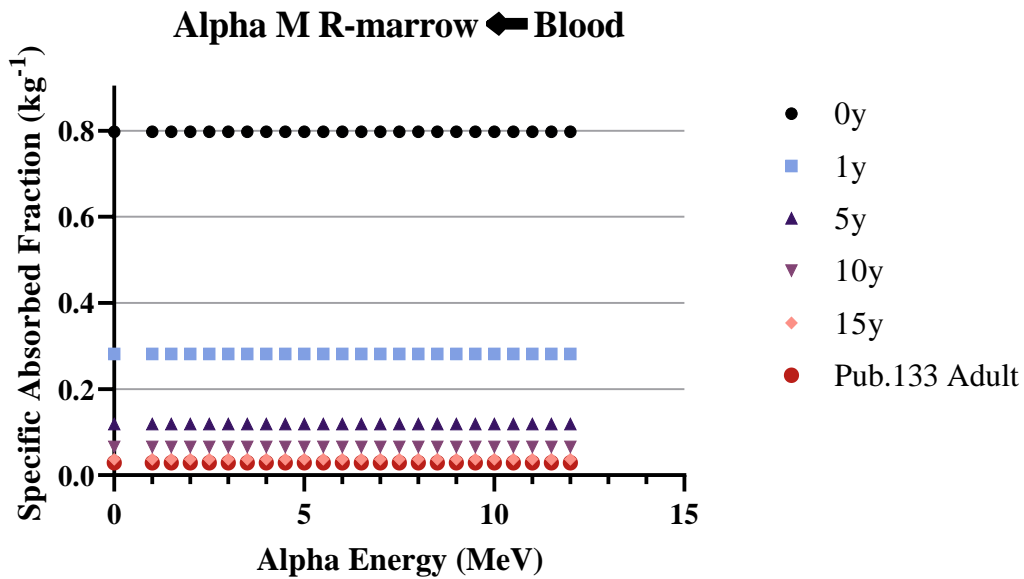
1463 (148) The plots in this section contain additional examples of SAFs plotted for all reference
 1464 ages. Figures 5.13 through 5.16 are examples of alpha particle SAFs, all of which result from

1465 absorbed fractions of unity which are independent of alpha energy. Differences, therefore, are
 1466 solely the result of differences in target masses.
 1467



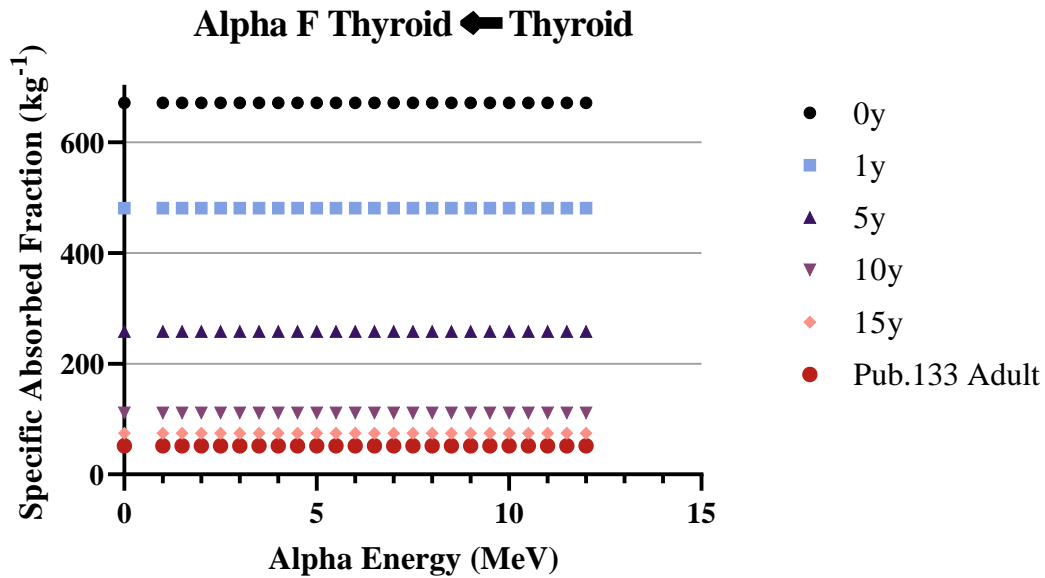
1468 Fig. 5.13. Liver self-irradiation alpha particle SAFs in the reference females.
 1469
 1470

1471

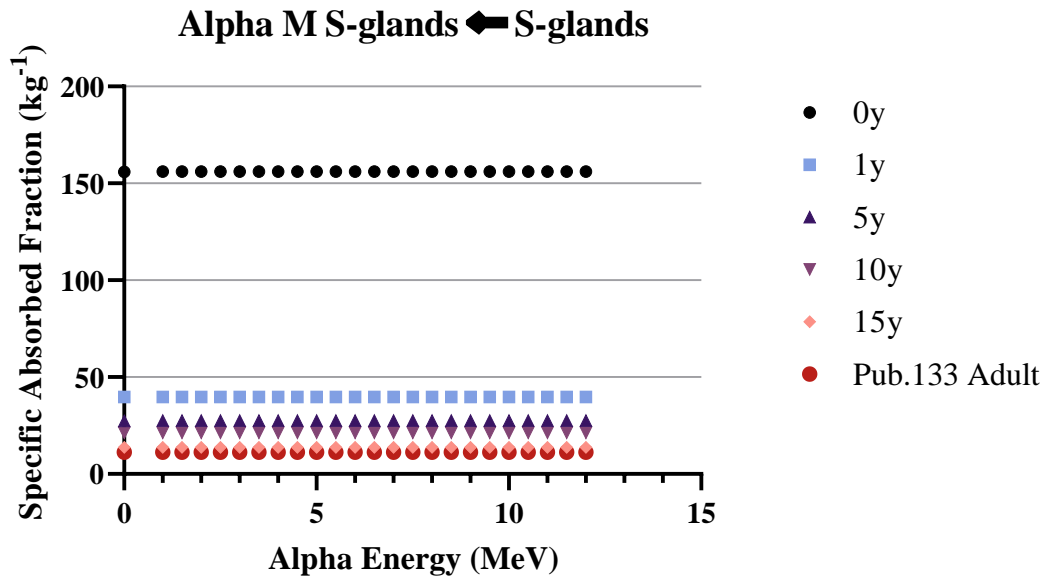


1472 Fig. 5.14. Alpha particle SAFs to the red marrow for emissions from the blood in the reference
 1473 males.
 1474

1475
 1476
 1477



1478
1479 Fig. 5.15. Alpha particle SAFs for thyroid self-irradiation in the reference females.
1480

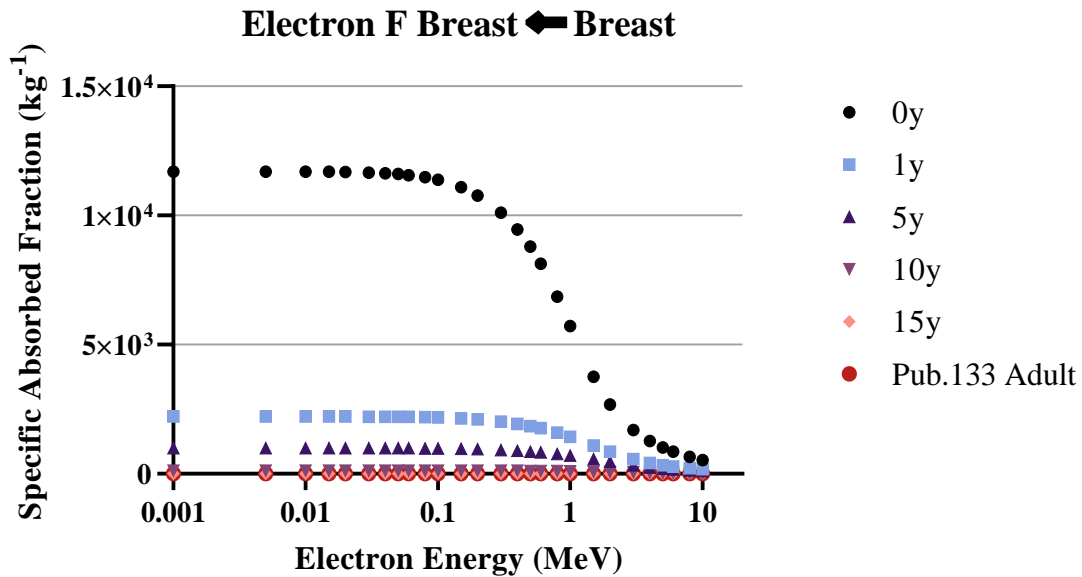


1481
1482 Fig. 5.16. Alpha particle SAFs for salivary glands self-irradiation in the reference males.
1483

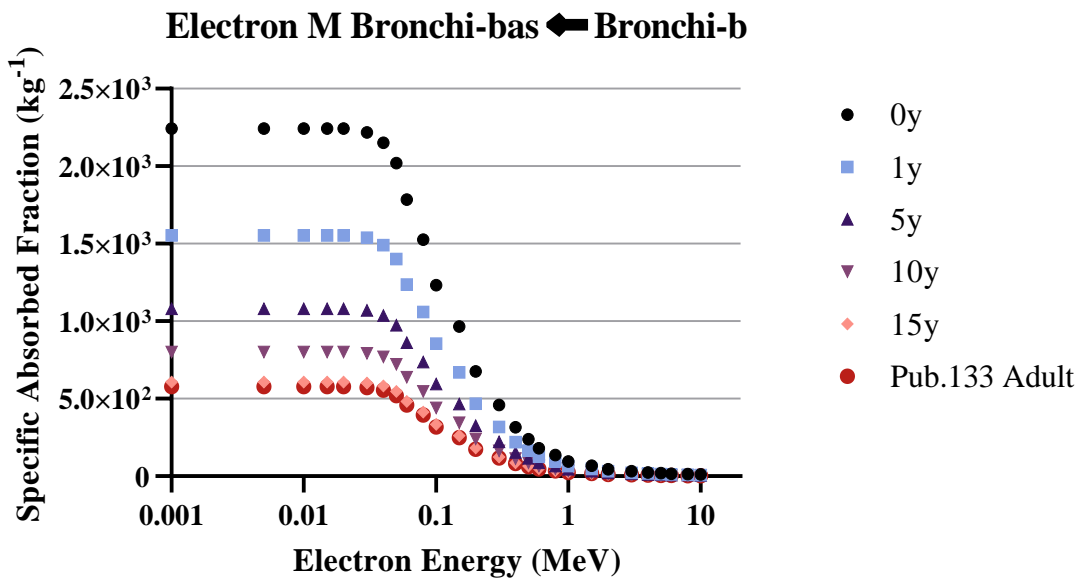
1484 (149) Figures 5.17 through 5.20 are examples of electron SAFs. Figure 5.17 shows electron
1485 SAFs for self-irradiation of the female breast. Figure 5.18 has electron SAFs in the male for
1486 irradiation of the bronchi basal target from source bound in the bronchi epithelium. Figure 5.19
1487 shows the irradiation of the stomach stem cell target by electrons originating in the stomach
1488 contents.

1489 (150) Figure 5.20 contains SAFs for electrons emitted from the blood irradiating the AI target.
1490 The expected age dependency based on varying target mass is observed. At the highest electron
1491 energies, a surprising peak is seen in the newborn SAFs. Further exploration of the source SAFs

1492 reveals this is coming from the collisional component of the electron SAF and not the radiative
 1493 component. The target in this case is the lung located somewhat centrally in the trunk of the body.
 1494 The source is blood both within the lung (driving the SAF at low and moderate energies) but also
 1495 blood in tissues neighbouring the lung. It is thought that the peak results from electrons from these
 1496 neighbouring tissues (e.g. heart) being able to reach the lung target. This effect is observed in the
 1497 newborn and not the older phantoms due to the smaller size and proximity of all organs in the
 1498 newborn.
 1499

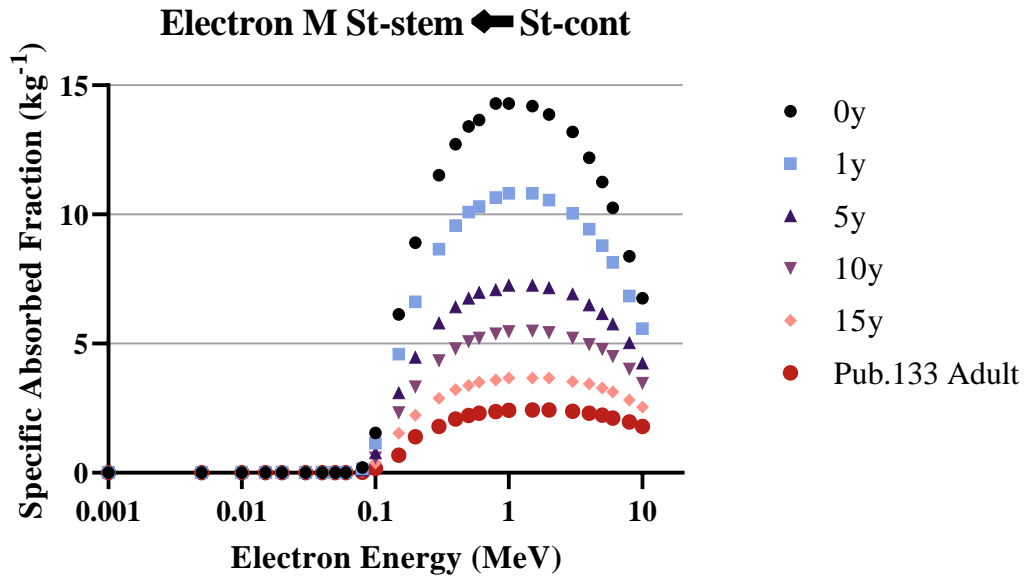


1500 Fig. 5.17. Electron SAFs for breast self-irradiation in the reference females.
 1501
 1502
 1503

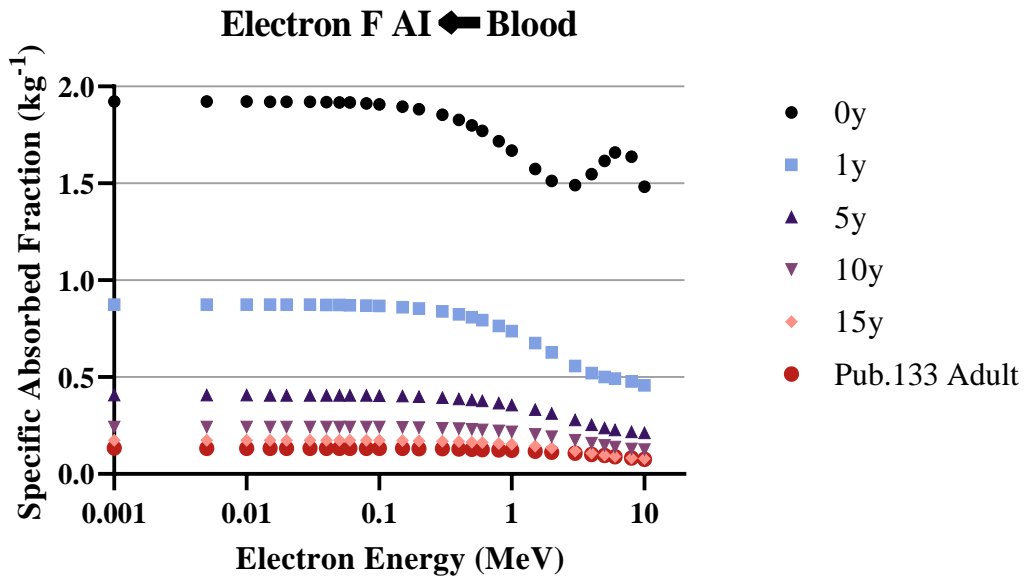


1504

1505 Fig. 5.18. Electron SAFs for emissions from the bound bronchi epithelium irradiating the bronchi
 1506 basal layer in the reference males.
 1507



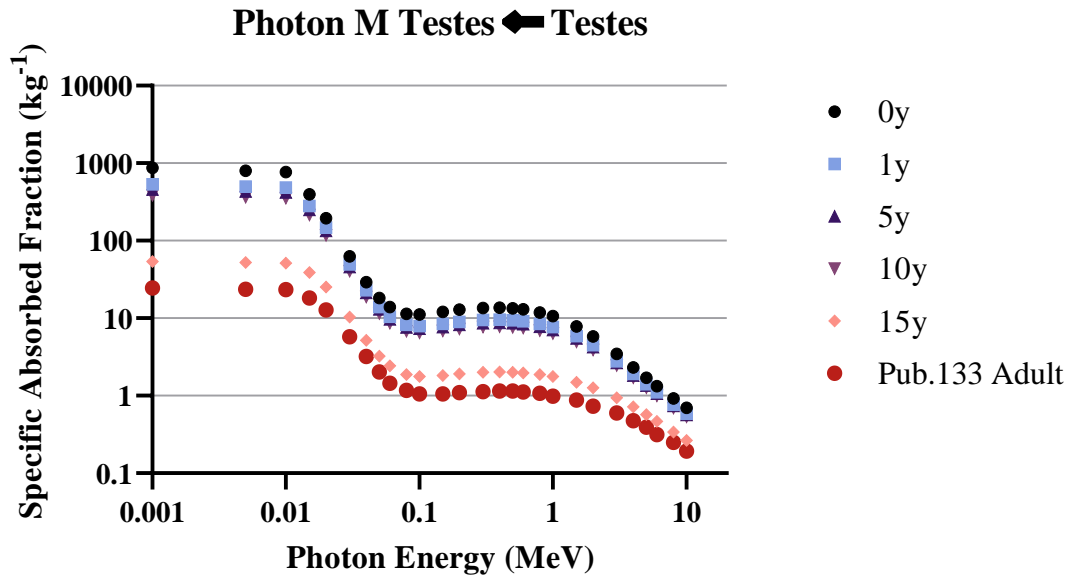
1508 Fig. 5.19. Electron SAFs for emissions from the stomach contents irradiating the stomach stem
 1509 cell layer in the reference males.
 1510
 1511
 1512



1513 Fig. 5.20. Electron SAFs for emissions from the blood irradiating the alveolar interstitial target in
 1514 the reference females.
 1515
 1516
 1517
 1518

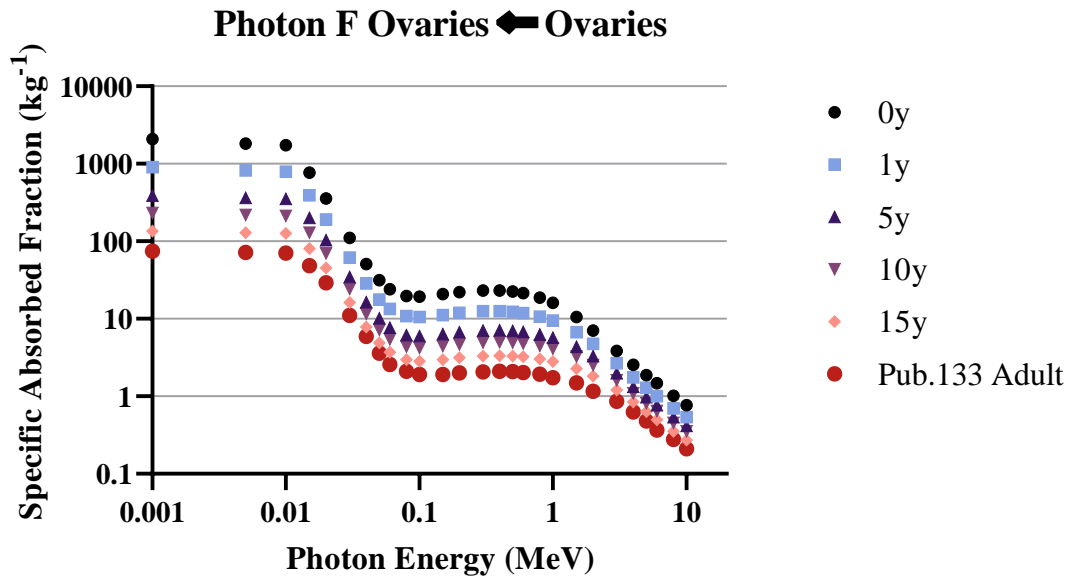
1519
1520
1521
1522
1523
1524

(151) Figures 5.21 through 5.24 are examples of photon SAFs. In all cases the expected age dependency is observed.



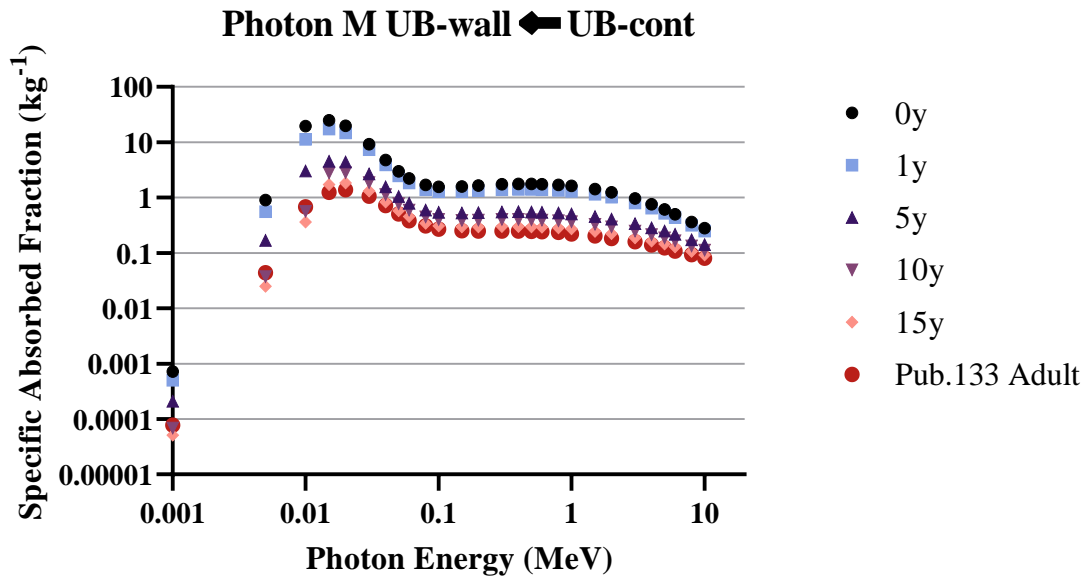
1525
1526
1527

Fig. 5.21. Photon SAFs for testes self-irradiation in the reference males.



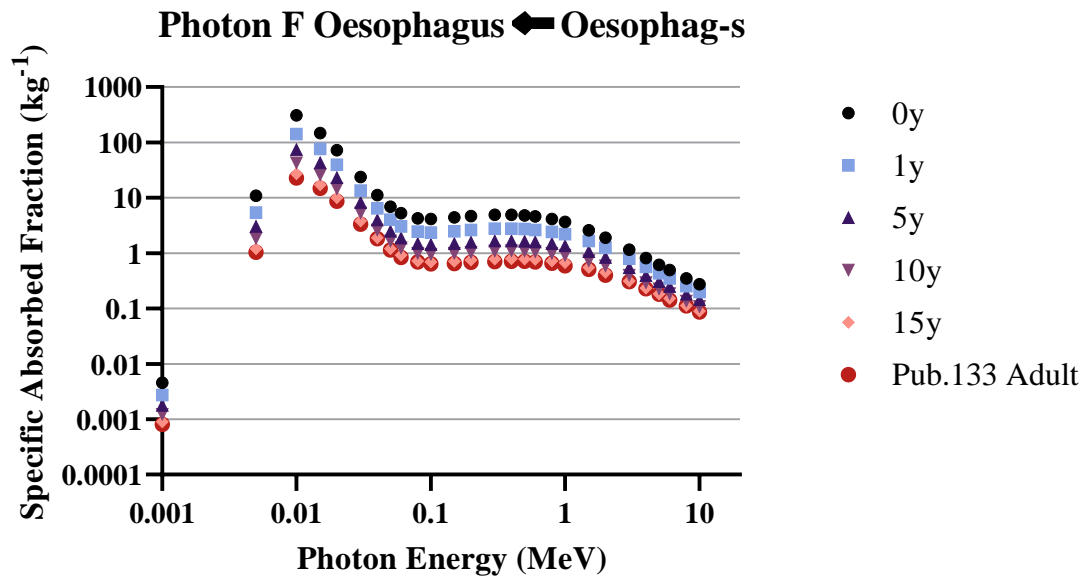
1528
1529
1530
1531
1532

Fig. 5.22. Photon SAFs for ovaries self-irradiation in the reference females.



1533
1534
1535
1536
1537

Fig. 5.23. Photon SAFs for emissions from the urinary bladder contents irradiating the urinary bladder wall in the reference males.



1538
1539
1540
1541
1542
1543
1544
1545
1546

Fig. 5.24. Photon SAFs for emissions from the oesophagus contents irradiating the oesophagus stem cell target in the reference females.

REFERENCES

1547
 1548
 1549 Adams, N., 1981. Dependence on age at intake of committed dose equivalents from radionuclides. *Phys*
 1550 *Med Biol* 26, 1019-1034.
 1551 Bahadori, A.A., Johnson, P., Jokisch, D.W., et al., 2011. Response functions for computing absorbed dose
 1552 to skeletal tissues from neutron irradiation. *Phys Med Biol* 56, 6873-6897.
 1553 Beddoe, A.H., Darley, P.J., and Spiers, F.W., 1976. Measurements of trabecular bone structure in man (for
 1554 radionuclide dosimetry). *Phys Med Biol* 21, 589-607.
 1555 Bolch, W.E., Shah, A.P., Watchman, C.J., et al., 2007. Skeletal absorbed fractions for electrons in the adult
 1556 male: considerations of a revised 50-microm definition of the bone endosteum. *Radiat Prot Dosimetry*
 1557 127, 169-173.
 1558 Bouchet, L.G., Bolch, W.E., Howell, R.W., et al., 2000. S values for radionuclides localized within the
 1559 skeleton. *J Nucl Med* 41, 189-212.
 1560 Bouchet, L.G., Jokisch, D.W., and Bolch, W.E., 1999. A three-dimensional transport model for determining
 1561 absorbed fractions of energy for electrons within trabecular bone. *J Nucl Med* 40, 1947-1966.
 1562 Bourke, V., Watchman, C., Reith, J., et al., 2009. Spatial gradients of blood vessels and hematopoietic stem
 1563 and progenitor cells within the marrow cavities of the human skeleton. *Blood* 114, 4077-4080.
 1564 Cristy, M., 1981. Active bone marrow distribution as a function of age in humans. *Phys Med Biol* 26, 389-
 1565 400.
 1566 Dant, J.T., Richardson, R.B., and Nie, L.H., 2013. Monte Carlo simulation of age-dependent radiation dose
 1567 from alpha- and beta-emitting radionuclides to critical trabecular bone and marrow targets. *Phys Med*
 1568 *Biol* 58, 3301-3319.
 1569 Degteva, M.O., Tolstykh, E.I., Shishkina, E.A., et al., 2021. Stochastic parametric skeletal dosimetry model
 1570 for humans: general approach and application to active marrow exposure from bone-seeking beta-
 1571 particle emitters. *PLoS ONE* 16, e0257605.
 1572 Eckerman, K., Bolch, W., Zankl, M., et al., 2008. Response functions for computing absorbed dose to
 1573 skeletal tissues for photon irradiation. *Radiat Prot Dosimetry* 127, 187-191.
 1574 Eckerman, K.F., Ryman, J.C., Taner, A.C., et al., 1985. "Traversal of cells by radiation and absorbed
 1575 fraction estimates for electrons and alpha particles." In *Proceedings of the Fourth International*
 1576 *Radiopharmaceutical Dosimetry Symposium*, edited by A.T. Schlafke-Stelson and E.E. Watson, 67-81.
 1577 Oak Ridge, Tennessee: Oak Ridge Associated Universities.
 1578 Eckerman, K.F., and Stabin, M.G., 2000. Electron absorbed fractions and dose conversion factors for
 1579 marrow and bone by skeletal regions. *Health Phys* 78, 199-214.
 1580 Eveleth, P.B., and Tanner, J.M., 1990. *Worldwide Variation in Human Growth*, 2nd edn. (Cambridge
 1581 University Press: Cambridge, UK).
 1582 Fritsch, F., and Carlson, R., 1980. Monotone piecewise cubic interpolation. *SIAM Journal on Numerical*
 1583 *Analysis* 17, 238-246.
 1584 Gao, S., Ren, L., Qiu, R., et al., 2017. Electron absorbed fractions in an image-based microscopic skeletal
 1585 dosimetry model of chinese adult male. *Radiation Protection Dosimetry* 175, 450-459.
 1586 Gaultier, C., Boule, M., Allaire, Y., et al., 1979. Growth of lung volumes during the first three years of life.
 1587 *Bull Eur Physiopathol Respir* 15, 1103-16.
 1588 Gossner, W., 2003. Target cells in internal dosimetry. *Radiat Prot Dosimetry* 105, 39-42.
 1589 Gossner, W., Masse, R., and Stather, J.W., 2000. Cells at risk for dosimetric modeling relevant to bone
 1590 tumour induction. *Radiat Prot Dosimetry* 92, 209-213.
 1591 Griffin, K.T., Eckerman, K.F., Manger, R.P., et al., 2022. Specific absorbed fractions for spontaneous
 1592 fission neutron emitters in the ICRP reference pediatric voxel phantom series. *Health Phys*.
 1593 Hough, M., Johnson, P., Rajon, D., et al., 2011. An image-based skeletal dosimetry model for the ICRP
 1594 reference adult male--internal electron sources. *Phys Med Biol* 56, 2309-2346.
 1595 Howerton, R.J., 1986. "Calculated neutron KERMA factors based on the LLNL ENDL data files." In
 1596 Livermore, CA: Lawrence Livermore National Laboratory.

- 1597 Hunt, J.G., Watchman, C.J., and Bolch, W.E., 2007. Calculation of absorbed fractions to human skeletal
1598 tissues due to alpha particles using the Monte Carlo and 3-d chord-based transport techniques. *Radiation*
1599 *Protection Dosimetry* 127, 223-226.
- 1600 ICRP, 1968. A review of the radiosensitivity of the tissues in bone (Pergamon Press: Oxford).
- 1601 ICRP, 1973. Alkaline earth metabolism in adult man (Pergamon Press: Oxford).
- 1602 ICRP, 1975. Report of the task group on reference man. ICRP Publication 23 (Pergamon Press: Oxford).
- 1603 ICRP, 1977. Recommendations of the ICRP. *Ann. ICRP* 1.
- 1604 ICRP, 1979. Limits for intakes of radionuclides by workers. *Ann. ICRP* 2.
- 1605 ICRP, 1994. Human respiratory tract model for radiological protection. A report of a Task Group of the
1606 International Commission on Radiological Protection. *Ann ICRP* 24, 1-482.
- 1607 ICRP, 1995a. Age-dependent doses to members of the public from intake of radionuclides - part 4 inhalation
1608 dose coefficients. ICRP Publication 71. *Ann ICRP* 25.
- 1609 ICRP, 1995b. Basic anatomical and physiological data for use in radiological protection - the skeleton. *Ann.*
1610 *ICRP* 25.
- 1611 ICRP, 2001. Doses to the embryo and fetus from intakes of radionuclides by the mother. *Ann. ICRP* 31.
- 1612 ICRP, 2002. Basic anatomical and physiological data for use in radiological protection: reference values.
1613 A report of age- and gender-related differences in the anatomical and physiological characteristics of
1614 reference individuals. ICRP Publication 89. *Ann ICRP* 32, 5-265.
- 1615 ICRP, 2006. Human alimentary tract model for radiological protection. ICRP Publication 100. A report of
1616 The International Commission on Radiological Protection. *Ann ICRP* 36, 25-327, iii.
- 1617 ICRP, 2007. The 2007 Recommendations of the International Commission on Radiological Protection.
1618 ICRP publication 103. *Ann ICRP* 37, 1-332.
- 1619 ICRP, 2008a. ICRP Publication 107. Nuclear decay data for dosimetric calculations. *Ann ICRP* 38, 7-96.
- 1620 ICRP, 2008b. Radiation dose to patients from radiopharmaceuticals - addendum 3 to ICRP Publication 53.
1621 *Ann. ICRP* 38.
- 1622 ICRP, 2009. ICRP Publication 110. Realistic reference phantoms: an ICRP/ICRU joint effort. A report of
1623 adult reference computational phantoms. *Ann ICRP* 39, 1-164.
- 1624 ICRP, 2010. ICRP Publication 116. Conversion coefficients for radiological protection quantities for
1625 external radiation exposures. *Ann ICRP* 40, 1-257.
- 1626 ICRP, 2013. Assessment of radiation exposure of astronauts in space. ICRP Publication 123. *Ann ICRP* 42.
- 1627 ICRP, 2015. ICRP Publication 130: Occupational Intakes of Radionuclides: Part 1. *Ann ICRP* 44, 5-188.
- 1628 ICRP, 2016a. ICRP Publication 133: The ICRP computational framework for internal dose assessment for
1629 reference adults: specific absorbed fractions. *Ann ICRP* 45, 5-73.
- 1630 ICRP, 2016b. ICRP Publication 134: Occupational Intakes of Radionuclides: Part 2. *Ann ICRP* 45, 7-349.
- 1631 ICRP, 2017. ICRP Publication 137: Occupational Intakes of Radionuclides: Part 3. *Ann ICRP* 46, 1-486.
- 1632 ICRP, 2019. ICRP Publication 141: Occupational Intakes of Radionuclides: Part 4. *Ann ICRP* 48, 9-501.
- 1633 ICRP, 2020a. Adult mesh-type reference computational phantoms. ICRP Publication 145. *Ann ICRP* 49.
- 1634 ICRP, 2020b. ICRP Publication 143: Paediatric Reference Computational Phantoms. *Ann ICRP* 49, 5-297.
- 1635 ICRP, 2020c. ICRP Publication 144: Dose Coefficients for External Exposures to Environmental Sources.
1636 *Annals of the ICRP* 49, 11-145.
- 1637 ICRP, 2022. Occupational intakes of radionuclides: Part 5. ICRP Publication 151. *Ann ICRP* 51.
- 1638 Johnson, P.B.B., A.A.; Eckerman, K.F.; Lee, C; Bolch, W.E.;, 2011. Response functions for computing
1639 absorbed dose to skeletal tissue from photon irradiation - an update. *Phys Med Biol* 56, 2347-2365.
- 1640 Jokisch, D.W., Bouchet, L.G., Patton, P.W., et al., 2001. Beta-particle dosimetry of the trabecular skeleton
1641 using Monte Carlo transport within 3D digital images. *Med Phys* 28, 1505-1518.
- 1642 Kramer, R., Cassola, V.F., Vieira, J.W., et al., 2012. Skeletal dosimetry based on microCT images of
1643 trabecular bone: update and comparisons. *Phys Med Biol* 57, 3995-4021.
- 1644 Lee, C., Lodwick, D., Hurtado, J., et al., 2010. The UF family of reference hybrid phantoms for
1645 computational radiation dosimetry. *Phys Med Biol* 55, 339-363.

1646 Mays, C., and Sears, K., 1962. "Determination of Localized Alpha Dose. III. From Surface and Volume
 1647 Deposits of Pu-230, Th-228, and Ra-226." In *Report COO-226*. Salt Lake City, UT: University of Utah.
 1648 O'Reilly, S.E., DeWeese, L.S., Maynard, M.R., et al., 2016. An image-based skeletal dosimetry model for
 1649 the ICRP reference adult female-internal electron sources. *Phys Med Biol* 61, 8794-8824.
 1650 Pafundi, D. 2009. 'Image-based skeletal tissue and electron dosimetry models for the ICRP reference
 1651 pediatric age series', Dissertation, University of Florida.
 1652 Pafundi, D., Lee, C., Watchman, C.J., et al., 2009. An image-based skeletal tissue model for the ICRP
 1653 reference newborn. *Phys Med Biol* 54, 4497-4531.
 1654 Pafundi, D., Rajon, D., Jokisch, D., et al., 2010. An image-based skeletal dosimetry model for the ICRP
 1655 reference newborn--internal electron sources. *Phys Med Biol* 55, 1785-1814.
 1656 Patton, P.W., Rajon, D.A., Shah, A.P., et al., 2002. Site-specific variability in trabecular bone dosimetry:
 1657 considerations of energy loss to cortical bone. *Med Phys* 29, 6-14.
 1658 Pelowitz, D.B., 2011. "MCNPX User's Manual Version 2.7.0." In, edited by Los Alamos National
 1659 Laboratory. Los Alamos, New Mexico, USA.
 1660 Pelowitz, D.B., 2013. "MCNP6 User's Manual Version 1.0." In.
 1661 Petoussi-Hens, N., Bolch, W.E., Zankl, M., et al., 2007. Patient-specific scaling of reference S-values for
 1662 cross-organ radionuclide S-values: what is appropriate? *Radiat Prot Dosimetry* 127, 192-196.
 1663 Phalen, R.F., Oldham, M.J., Beaucage, C.B., et al., 1985. Postnatal enlargement of human tracheobronchial
 1664 airways and implications for particle deposition. *Anat. Rec.* 212, 368-380.
 1665 Rowland, R.E., 1966. Exchangeable bone calcium. *Current Orthopaedic Practice* 49, 233-248.
 1666 Schwarz, B.C., Godwin, W.J., Wayson, M.B., et al., 2021a. Specific absorbed fractions for a revised series
 1667 of the UF/NCI pediatric reference phantoms: internal electron sources. *Physics in medicine and biology*
 1668 66, 035005.
 1669 Schwarz, B.C., Godwin, W.J., Wayson, M.B., et al., 2021b. Specific absorbed fractions for a revised series
 1670 of the UF/NCI pediatric reference phantoms: internal photon sources. *Physics in medicine and biology*
 1671 66, 035006.
 1672 Shah, A.P., Rajon, D.A., Patton, P.W., et al., 2005. Accounting for beta-particle energy loss to cortical bone
 1673 via paired-image radiation transport (PIRT). *Med Phys* 32, 1354-1366.
 1674 Snyder, W.S., 1970. Estimation of absorbed fraction of energy from photon sources in body organs.
 1675 Snyder, W.S., Ford, M.R., Warner, G.G., et al., 1975. MIRD Pamphlet No. 11: S, absorbed dose per unit
 1676 cumulated activity for selected radionuclides and organs. Society of Nuclear Medicine.
 1677 Spiers, F.W., 1968. *Radioisotopes in the Human Body* (Academic Press: New York and London).
 1678 Spiers, F.W. 1969. 'Beta particle dosimetry in trabecular bone.' in C.W. Mays, W.S.S. Jee, R.D. Lloyd, B.J.
 1679 Stover, J.H. Dougherty and G.N. Taylor (eds.), *Delayed Effects of Bone Seeking Radionuclides*
 1680 (University of Utah Press: Salt Lake City).
 1681 Spiers, F.W., 1970. Determination of absorbed dose to bone and red bone marrow.
 1682 Spiers, F.W., 1974. Radionuclides and bone - from Ra-226 to Sr-90. *Br J Radiol* 47, 833-44.
 1683 Stabin, M.G., Eckerman, K.F., Bolch, W.E., et al., 2002. Evolution and status of bone models. *Cancer*
 1684 *Biotherapy & Radiopharmaceuticals* 17, 427-433.
 1685 Stabin, M.G., and Siegel, J.A., 2003. Physical models and dose factors for use in internal dose assessment.
 1686 *Health Phys* 83, 294-310.
 1687 Sugiyama, H., Misumi, M., Brenner, A., et al., 2020. Radiation risk of incident colorectal cancer by
 1688 anatomical site among atomic bomb survivors: 1958-2009. *Int J Cancer* 146, 635-645.
 1689 Thorne, M.C., 1976. Aspects of the dosimetry of plutonium in bone. *Nature* 259, 539-541.
 1690 Thorne, M.C., 1977. Aspects of the dosimetry of alpha-emitting radionuclides in bone with particular
 1691 emphasis on Ra-226 and Pu-239. *Phys Med Biol* 22, 36-46.
 1692 Watchman, C.J., and Bolch, W.E., 2009. Absorbed fractions for alpha-particles in tissues of cortical bone.
 1693 *Phys Med Biol* 54, 6009-6027.



1694 Watchman, C.J., Jokisch, D.W., Patton, P.W., et al., 2005. Absorbed fractions for alpha-particles in tissues
1695 of trabecular bone: considerations of marrow cellularity within the ICRP reference male. *J Nucl Med*
1696 46, 1171-1185.

1697 Watchman, C., Bourke, V., Lyon, J., et al., 2007. Spatial distribution of blood vessels and CD34+
1698 hematopoietic stem and progenitor cells within the marrow cavities of human cancellous bone. *J Nucl*
1699 *Med* 48, 645-654.

1700 Wayson, M., Lee, C., Sgouros, G., et al., 2012. Internal photon and electron dosimetry of the newborn
1701 patient - a hybrid computational phantom study. *Phys Med Biol* 57, 1433-1457.

1702 Wayson, M.B. 2012. 'Computational internal dosimetry methods as applied to the University of Florida
1703 series of hybrid phantoms', University of Florida.

1704 Wayson, M.B., and Bolch, W.E., 2018. Individualized adjustments to reference phantom internal organ
1705 dosimetry - scaling factors given knowledge of patient internal anatomy. *Phys Med Biol* 63, 085006.

1706 Wayson, M.B., Leggett, R.W., Jokisch, D.W., et al., 2018. Suggested reference values for regional blood
1707 volumes in children and adolescents. *Phys Med Biol* 63, 155022.

1708 Whitwell, J.R. 1973. 'Theoretical investigations of energy loss by ionizing particles in bone', University of
1709 Leeds.

1710 Whitwell, J.R., and Spiers, F.W., 1976. Calculated beta-ray dose factors for trabecular bone. *Phys Med Biol*
1711 21, 16-38.

1712 Zankl, M., Becker, J., Fill, U., et al., 2005. "GSF male and female adult voxel models representing ICRP
1713 Reference Man - the present status." In *The Monte Carlo Method: Versatility Unbounded in a Dynamic*
1714 *Computing World*. American Nuclear Society.

1715 Zankl, M., and Wittmann, A., 2001. The adult male voxel model "Golem" segmented from whole-body CT
1716 patient data. *Radiat Environ Biophys* 40, 153-162.

1717

1718

1719

1720

ANNEX A. DESCRIPTION OF ELECTRONIC FILES

1721 (A 1) Electronic files containing SAFs, source and target region masses, and skeletal photon
 1722 dose response functions are available for download at www.icrp.org as a supplement to this
 1723 publication. The SAF and mass files use the abbreviations provided in Tables 3.9 and 3.16.
 1724

1725 (A 2) The SAF filenames are provided in Table A.1. Source region masses for the female are
 1726 found in Sregions_Female.ndx and for the male in Sregions_Male.ndx. Target region masses are
 1727 found in Torgans_Female.ndx and Torgans_Male.ndx.
 1728

1729
 1730 Table A.1. Filenames for specific absorbed fraction tables

Reference Individual	Photons	Electrons	Alpha particles	Neutrons
Newborn female	rcp-00F_photon.SAF	rcp-00F_electron.SAF	rcp-00F_alpha.SAF	rcp-00F_neutron.SAF
Newborn male	rcp-00M_photon.SAF	rcp-00M_electron.SAF	rcp-00M_alpha.SAF	rcp-00M_neutron.SAF
1y female	rcp-01F_photon.SAF	rcp-01F_electron.SAF	rcp-01F_alpha.SAF	rcp-01F_neutron.SAF
1y male	rcp-01M_photon.SAF	rcp-01M_electron.SAF	rcp-01M_alpha.SAF	rcp-01M_neutron.SAF
5y female	rcp-05F_photon.SAF	rcp-05F_electron.SAF	rcp-05F_alpha.SAF	rcp-05F_neutron.SAF
5y male	rcp-05M_photon.SAF	rcp-05M_electron.SAF	rcp-05M_alpha.SAF	rcp-05M_neutron.SAF
10y female	rcp-10F_photon.SAF	rcp-10F_electron.SAF	rcp-10F_alpha.SAF	rcp-10F_neutron.SAF
10y male	rcp-10M_photon.SAF	rcp-10M_electron.SAF	rcp-10M_alpha.SAF	rcp-10M_neutron.SAF
15y female	rcp-15F_photon.SAF	rcp-15F_electron.SAF	rcp-15F_alpha.SAF	rcp-15F_neutron.SAF
15y male	rcp-15M_photon.SAF	rcp-15M_electron.SAF	rcp-15M_alpha.SAF	rcp-15M_neutron.SAF
Adult female	rcp-af_photon.SAF	rcp-af_electron.SAF	rcp-af_alpha.SAF	rcp-af_neutron.SAF
Adult male	rcp-am_photon.SAF	rcp-am_electron.SAF	rcp-am_alpha.SAF	rcp-am_neutron.SAF

1731 (A 3) Each of the SAF files has five header rows with the sixth row containing SAFs for the
 1732 first described source/target geometry. Annex B of *Publication 133* details the manner of access
 1733 to the files. There are a total of 43 target regions and 79 source regions resulting in 3,402 rows of
 1734 SAFs in each file. Each row in the file contains 315 (photons and electrons) or 270 (alphas)
 1735 characters. The difference in characters results from photon and electron SAFs being tabulated for
 1736 28 energies while the alpha SAFs are tabulated for 24 energies. These energies appear in units of
 1737 MeV in the fourth row of each file.
 1738

1739 (A 4) The last two columns in each SAF file contain the Ecutoff and ID. The Ecutoff value is
 1740 the kinetic energy of the lowest energy radiation for that geometry which contains a non-zero value
 1741 for the SAF. If all SAFs for that geometry are non-zero, the Ecutoff is zero. The ID is the index
 1742 (integer location) of the Ecutoff value. If the Ecutoff for a particular geometry (row) was 0.010
 1743 MeV, which is the fourth energy on the electron energy grid, the ID would be 4.
 1744

1745 (A 5) Neutron SAFs are structured differently since they are weighted for each radionuclide's
 1746 spontaneous fission spectrum. The fourth row of each neutron SAF file contains the spectrum-
 1747 weighted neutron radiation weighting factor which should be applied if computing equivalent and
 1748 effective dose. Twenty-eight radionuclides are listed in each file and are: ²³⁸U, ²³⁶Pu, ²³⁸Pu, ²⁴⁰Pu,
 1749 ²⁴²Pu, ²⁴⁴Pu, ²⁴⁰Cm, ²⁴²Cm, ²⁴⁴Cm, ²⁴⁵Cm, ²⁴⁶Cm, ²⁴⁸Cm, ²⁵⁰Cm, ²⁴⁶Cf, ²⁴⁸Cf, ²⁴⁹Cf, ²⁵⁰Cf, ²⁵²Cf,
 1750 ²⁵⁴Cf, ²⁵³Es, ²⁵⁴Es, ^{254m}Es, ²⁵⁵Es, ²⁵²Fm, ²⁵⁴Fm, ²⁵⁵Fm, ²⁵⁶Fm, and ²⁵⁷Fm.
 1751

1752 (A 6) The date of last revision to each SAF and mass file is listed on the far right of the first
 1753 row. Note that dates may not be consistent across all files as revisions occur for some files without
 1754 affecting other files.

1753 (A 7) The skeletal photon dose response functions have been described in sections 4.1.2 and
1754 4.4.4. They are provided and have a filename photon_drf.xls. Note that the dose response functions
1755 used in this work to compute photon SAFs were an earlier version (up to date at the time the SAFs
1756 were computed). The values of the skeletal photon dose response functions provided here have
1757 been recently revised and refined by the members of ICRP Task Group 113 in their work on
1758 reference dose coefficients for radiological imaging exams using the *Publication 110* adult and
1759 *Publication 143* paediatric reference voxel phantoms.
1760

1761

ACKNOWLEDGEMENTS

1762 This publication provides specific absorbed fractions (SAFs) for the ICRP reference individuals.
1763 SAFs for the reference adults are identical to those provided in *Publication 133* (ICRP 2016a).
1764 The methodology for computing these SAFs is presented along with a description of their use in
1765 the forthcoming publication of dose coefficients for intakes of radionuclides by members of the
1766 public. Calculation of SAFs requires knowledge of tissue masses for the reference individuals
1767 (described in section 3) and simulation of radiation transport in computational models (described
1768 in section 4.) The reference masses provided in section 3 are supplemented and modified when
1769 necessary, but based largely on values in *Publications 66, 89, and 100* (ICRP 1995b).
1770 Computational models include reference voxel phantoms of *Publications 110 and 143* (ICRP 2009,
1771 2020b), mathematical stylised models for the alimentary and respiratory tracts largely defined in
1772 *Publication 66 and 100* (ICRP 1994, 2006), and skeletal voxel models (Pafundi et al. 2010; Hough
1773 et al. 2011; O'Reilly et al. 2016). While these SAFs for reference individuals are designed for
1774 radiation protection purposes and the calculation of reference dose coefficients, it is anticipated
1775 they may be used in other applications including nuclear medicine and dose reconstruction.

1776 **Task Group 96 – Computational Phantoms and Radiation Transport members (2014-**
1777 **present)**

1778	W. E. Bolch (Chair)	K. Eckerman	J. Hunt
1779	D. Jokisch	K. P. Kim	C. H. Kim
1780	C. Lee	J. Li	N. Petoussi-Hens
1781	T. Sato	H. Schlattl	Y. S. Yeom
1782	M. Zankl		

1783 **Committee 2 critical reviewers**

1784	M. Andersson	M.S. Kulkarni	T. Sato
1785	D. de Souza Santos	J. Marsh	T. Smith
1786	A. Giussani	N. Petoussi-Hens	
1787			

1788 **Main Commission critical reviewers**

1789	M. Kai	S. Romanov
1790		

1791 **Editorial members**

1792 C. H. Clement (Scientific Secretary and *Annals of the ICRP* Editor-in-Chief)
1793 T. Yasumune (Assistant Scientific Secretary and *Annals of the ICRP* Associate Editor)
1794 (2022-)
1795 H. Fujita (Assistant Scientific Secretary and *Annals of the ICRP* Associate Editor)
1796 (2018-2022)
1797

1798 **Committee 2 members during preparation of this publication**

1799 (2017-2021)

1800	J. D. Harrison (Chair)	D. Jokisch	N. Petoussi-Henss
1801	F. Paquet (Vice-Chair)	C.H. Kim	T. Sato
1802	W.E. Bolch (Secretary)	R. Leggett	T. Smith
1803	V. Berkovskyy	J. Li	A. Ulanowski
1804	E. Blanchardon	M.A. Lopez	F. Wissmann
1805	A. Giussani		

1806

1807 (2021-2025)

1808	F. Bochud (Chair)	D. Jokisch	J.W. Marsh
1809	F. Paquet (Vice-Chair)	C.H. Kim	N. Petoussi-Henss
1810	M.A. Lopez (Secretary)	M.S. Kulkarni	T. Sato
1811	V. Berkovskyy	S. Lamart	T. Smith
1812	D. de Souza Santos	C. Lee	A. Ulanowski
1813	A. Giussani	J. Li	

1814 **Emeritus member**

1815 K. Eckerman

1816

1817 **Main Commission members at the time of approval of this publication**1818 Chair: W. Rühm, *Germany*1819 Vice-Chair: D.A. Cool, *USA*1820 Scientific Secretary: C.H. Clement, *Canada*; sci.sec@icrp.org[†]

1821

1822	K. Applegate, <i>USA</i>	D. Laurier, <i>France</i>	Emeritus members
1823	F. Bochud, <i>Switzerland</i>	S. Liu, <i>China</i>	R.H. Clarke, <i>UK</i>
1824	S. Bouffler, <i>UK</i>	S. Romanov, <i>Russia</i>	F.A. Mettler, <i>USA</i>
1825	K.W. Cho, <i>Korea</i>	T. Schneider, <i>France</i>	R.J. Pentreath, <i>UK</i>
1826	G. Hirth, <i>Australia</i>	A. Wojcik, <i>Sweden</i>	R.J. Preston, <i>USA</i>
1827	M. Kai, <i>Japan</i>		C. Streffer, <i>Germany</i>
1828			E. Vañó, <i>Spain</i>

1829

1830 [†]Although formally not a member since 1988, the Scientific Secretary is an integral part of the

1831 Main Commission.

1832

1833 The authors on behalf of ICRP thank M. Bellamy, S. Dewji, D. Gregoratto, R. Leggett, J. Marsh,

1834 G. Ratia, and T. Smith for their valuable contributions to this publication.

1835

1836